Turun yliopisto
University of Turku

Development of a Radiometer Front End for Detection of Oil Spill on Sea Surface

Matti Kaisti

Department of Information Technology
Faculty of Mathematics and Natural Sciences
University of Turku

MASTER´S THESIS

Turku 2012

UNIVERSITY OF TURKU
Department of Information Technology

MATTI KAISTI: Development of a Radiometer Front End for Detection of Oil Spill on Sea Surface

Master's Thesis, 104p.
Integrated circuits and systems
April 2012

Radiometry is a well-established science where electro-magnetic radiation emitted by all objects in the universe at temperatures above absolute zero is measured and analyzed. Microwave radiometers can be utilized in remote sensing to measure various properties related to the atmosphere and surface of the Earth. An antenna is commonly used to view the scene and collect the thermal radiation emitted or reflected from it. In the microwave region the available power P is directly related to the brightness temperature T_B, which in turn is directly related to physical temperature through emissivity. Emissivity can vary greatly between materials and surfaces and hence by measuring the brightness temperature of a scene, its properties can be determined.

Microwave radiometry has a unique potential to detect oil spill on water and to determine its thickness. A thin layer of oil on sea surface creates a thin-film interference. This multilayer system has two reflective surfaces. Depending on the thickness of the oil layer and frequency, these reflections produce either constructive or destructive interference. With a point frequency, this leads to oscillatory emissivity and hence brightness temperature as a function of the layer thickness. By modeling this phenomenon accurately, it can be compared to the measured brightness temperature to obtain the oil layer thickness.

In this thesis, two radiometers are designed and tested. The thesis is limited to the initial verification phase of the radiometers that are to be used in oil spill detection. Radiometers are designed for Ka-band at $36{,}5GHz$ and for W-band at $89GHz$. The main contribution of this thesis is the front-end design and testing, development of calibration procedure including cryogenic load design. Radiometer system design with simulations is presented.

Keywords: Radiometry, Radiometer, Oil spill, Front-end, Calibration

TURUN YLIOPISTO
Informaatioteknologian laitos

MATTI KAISTI: Radiometrin kehittäminen öljyläikän havainnointiin meren pinnalta

Diplomityö 104s.
Integroidut piirit ja systeemit
Huhtikuu 2012

Kaikki kappaleet säteilevät sähkömagneettista energiaa. Radiometreillä voidaan mitata tätä säteilyä, ja mittausten avulla voidaan kaukokartoituksessa analysoida monia ilmakehään ja maan pintaan liittyviä ilmiöitä. Säteilyä kerätään useimmiten radiometriin kytketyn antennin avulla. Mikroaaltoalueella säteilystä saatava teho on verrannollinen kohteen kirkkauslämpötilaan. Kirkkauslämpötila on puolestaan verrannollinen kohteen fyysiseen lämpötilaan materiaalin emissiivisyyden kautta. Emissiivisyys voi vaihdella suuresti eri pintojen ja materiaalien välillä. Näin ollen mittaamalla kohteen kirkkauslämpötilaa saadaan tietoa sen ominaisuuksista.

Mikroaaltoradiometrin avulla voidaan havaita öljyläikkä meren pinnalta, sekä määrittää öljyläikän paksuus. Öljy muodostaa ohuen kalvon meren pinnalla. Ohuen kalvon ylä- ja alapinnasta heijastuneet aallot kulkevat eri matkan, jonka seurauksena muodostuu interferenssikuvio. Interferenssi on joko konstruktiivinen tai destruktiivinen riippuen heijastusten vaihe-erosta. Pistetaajuudella tästä seuraa kalvon paksuudesta riippuva sinimuotoinen emissiivisyys. Mallintamalla tämä ilmiö riittävän tarkasti voidaan radiometrin mittaamaa kirkkauslämpötilaa verrata mallinnettuun arvoon ja täten määrittää öljykerroksen paksuus.

Tässä työssä esitetään kahden radiometrin suunnittelu ja testaus. Työ rajoittuu radiometrien alustavaan testausvaiheeseen. Radiometrit on suunniteltu 36,5GHz sekä 89GHz taajuuksille. Työn suurin kontribuutio on radiometrien etupään suunnittelussa ja testauksessa, kalibraatiomenetelmien kehittämisessä sekä kylmäkuorman suunnittelussa. Lisäksi työssä esitetään radiometrien systeemisuunnittelu sekä siihen liittyvät simulaatiot.

Avainsanat: Radiometria, Radiometri, Öljyläikkä, Etupää, Kalibraatio

ACKNOWLEDGEMENTS

Foremost, I would like to thank my instructor Torsti Poutanen for his guidance and support during my adventure in learning the science of Radiometry. In the many interesting discussions we have had - in addition to expanding my knowledge - I have gained a scientific mindset for problem solving. I will gratefully take this on through my engineering career.

I would also like to express my gratitude to my supervisor Professor Ari Paasio for the corrections and comments. Furthermore, I thank him for his flexibility which made it possible to get all the bureaucratic maneuvers done in time.

I am grateful to my spouse Aino for encouragement, proofreading and for correcting my abstruse writing.

Matti Kaisti
Lieto, 14.6.2012

TABLE OF CONTENTS

1 INTRODUCTION

Radiometry is a well-established science where electro-magnetic radiation emitted by all objects in the universe at temperatures above absolute zero is measured and analyzed. Microwave radiometers can be utilized in remote sensing to measure various properties related to the atmosphere and surface of the Earth. An antenna is commonly used to view the scene and collect the thermal radiation emitted or reflected from it. In microwave region the available power P is directly related to temperature T. For an idealized blackbody the measured equivalent radiometric temperature, defined as brightness temperature T_B, is equal to its physical temperature. For any real object the brightness temperature is always smaller than the physical temperature. Physical and brightness temperatures are related through emissivity $\varepsilon = T_B/T$ which varies between 0 (for perfectly non-emitting material) and 1 (for a perfect emitter). We can see that different bodies at the same temperature have different brightness temperatures depending on their emissivity. This enables the possibility to distinguish between materials if their emissivities are known.

Microwave radiometry has a unique potential to detect oil spill on water and to determine its thickness. A thin layer of oil on sea surface creates a thin-film interference. The multilayer system has two reflective surfaces. Depending on the thickness of the oil layer and frequency, these reflections produce either constructive or destructive interference. With a point frequency, this leads to oscillatory brightness temperature as a function of the layer thickness. By modeling this phenomenon accurately, the measured brightness temperature can be compared to the modeled one to obtain the oil layer thickness.

A fundamental difficulty in radiometric measurements is the nature of measured signal. Radiometers are generally used to measure thermal noise power levels below the self-emitted noise of the radiometers. Therefore, radiometers are configured for high degree of sensitivity. For accurate measurement results the radiometer needs to be calibrated. Calibration relates the input brightness temperature to the output voltage of the radiometer by measuring known temperature standards. Accuracy of the calibration is mainly determined by the quality of the calibration standards. Typically radiometers use absorbing materials with known physical temperatures or noise diodes with known noise power as temperature standards

In this thesis, two radiometers are designed and tested in a laboratory setup. The thesis is limited to the initial verification phase of the radiometers that are to be used in oil spill detection. Radiometers are designed for Ka-band at $36{,}5GHz$ and for W-band at $89GHz$. The main contribution of this thesis is the front-end design, testing and development of calibration procedure including cryogenic load design. Radiometer system design and simulations are computed and presented.

Chapter 2 provides an insight into the fundamental theories of radiometry and radiometers. Chapter 3 presents the system description. A simplified block diagram of the radiometer is included and discussed. Chapter 4 explains the relevant concepts and error sources of calibration with the help of simulations. Chapter 5 describes the front-end system design and mechanical design including radiometer box and microwave parts. Cryogenic load design and analysis is covered in chapter 6. The design and the measurement results of passive microwave parts are covered in chapter 7. Measurements of the active parts and an analysis on the radiometer performance are explained in chapter 8. Conclusions are given in chapter 9.

2 THEORETICAL BACKROUND

2.1 Principles of oil detection

The brightness temperature of oil on water is increased compared to clean water due to increased emissivity. When a film with different dielectric constant covers water a multilayer system exists. Depending on the frequency and slick thickness the waves either add in-phase (constructively) or out-off-phase (destructively) creating an oscillatory brightness temperature as a function of the layer thickness. The brightness temperature is given as

$$T_B(f,\theta,p) = \varepsilon(f,\theta,p)T_{sea} = (1 - |R(f,\theta,p)|^2)T_{sea} \quad (2\text{-}1)$$

The emissivity ε is a function of incident angle θ (angle to the normal of the layer), frequency f and polarization p. The complex reflection coefficient for the electromagnetic field arises from infinite amount of reflections and refractions from the multilayer system and is given by

$$R(d,f) = \frac{R_{12}^p + R_{23}^p e^{j2\sigma}}{1 + R_{12}^p R_{23}^p e^{j2\sigma}} \quad (2\text{-}2)$$

Where $\sigma = 2\pi\sqrt{e_{oil}}\cos(\theta_{oil})\, d/\lambda$. Reflections for vertical and horizontal polarization are given by

$$R_{ij}^V = \frac{\sqrt{\varepsilon_j}\cos(\theta_i) - \sqrt{\varepsilon_i}\cos(\theta_j)}{\sqrt{\varepsilon_j}\cos(\theta_i) + \sqrt{\varepsilon_i}\cos(\theta_j)} \quad (2\text{-}3)$$

$$R_{ij}^H = \frac{\sqrt{\varepsilon_i}\cos(\theta_i) - \sqrt{\varepsilon_j}\cos(\theta_j)}{\sqrt{\varepsilon_i}\cos(\theta_i) + \sqrt{\varepsilon_j}\cos(\theta_j)} \quad (2\text{-}4)$$

Figure 2-1 shows the brightness temperature as a function of oil film thickness for the two radiometer frequencies with angle of incidence 0 degrees. The frequencies were given to this thesis by previous study made in DA-Design Ltd and they are $36{,}5GHz$ and $89GHz$. The brightness temperature has oscillatory nature with a spatial period related to the wavelength in the oil film $\lambda \approx \lambda_0/\sqrt{e_{oil}}$. For 0 degree incident angle, the

polarization makes no difference, but for other angles horizontal polarization has a stronger reflection. The magnitude of brightness temperature increases with the angle of incidence for horizontal polarization and the opposite is true for vertical polarization. The periodic function makes it possible not only to detect oil, but also to determine its thickness. However, periodicity creates ambiguity in the measurements. This can be removed by introducing a multi-frequency system and combining sets of measurements with different frequency. When longer wavelengths are used, thicker oil slicks can be measured without the problem of ambiguity. On the other hand, this means that the sensitivity is decreased i.e. the measured signal has smaller change with a given oil slick thickness variation when longer wavelengths are used. The presented brightness temperature variation is for the simplest case only. It has been analyzed more thoroughly in DA-Design Ltd. and a brightness temperature is expected to vary between $100K \ldots 250K$. [1],[2],[3].

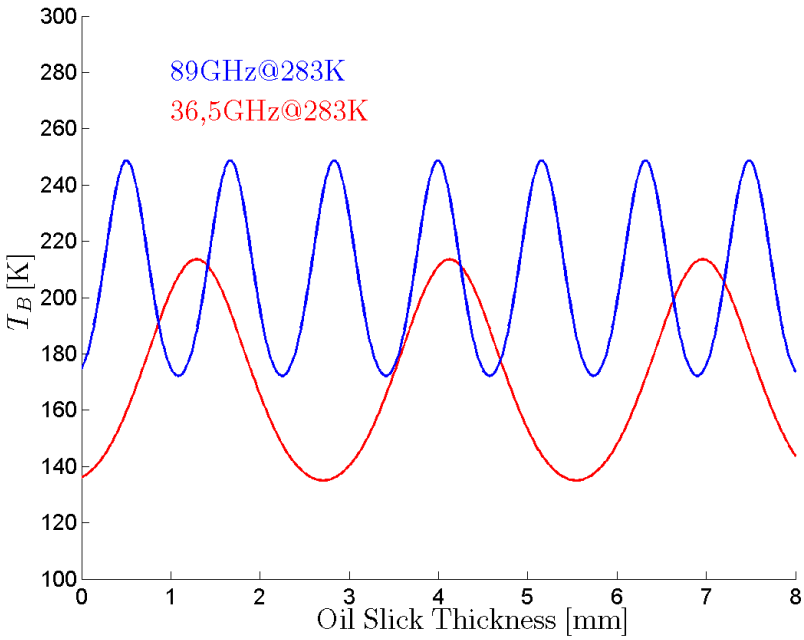

Figure 2-1 Brightness temperature as a function of oil slick thickness for 36,5GHz and 89GHz radiometer frequencies. The angle of incidence is 0 degrees.

2.2 Temperature and noise

All objects at temperature above absolute zero absorb and radiate electromagnetic energy. A blackbody by definition is an idealized perfect radiation absorber at all frequen-

cies. In order for blackbody to stay in thermal equilibrium it must also emit the same amount of energy that is incident on it, making it also a perfect emitter. Brightness of a blackbody is given by the *Planck's blackbody radiation law*

$$I_f = \frac{2hf^3}{c^2}\frac{1}{e^{hf/kT}-1} \tag{2-5}$$

where I_f is blackbody spectral brightness, $Wm^{-2}\,sr^{-1}\,Hz^{-1}$, h is the Planck constant, k is the Boltzmann constant, c is the speed of light in a vacuum and f is the frequency. At low frequencies $hf/kT \ll 1$ and the exponential term can be approximated with $e^{hf/kT} - 1 = hf/kT$ which leads to *Rayleigh Jeans* brightness approximation

$$I_f \approx \frac{2hf^3kT}{c^2hf} = \frac{2f^2kT}{c^2} = \frac{2kT}{\lambda^2} \tag{2-6}$$

Real materials emit less power than the blackbody at any temperature T. The brightness of such bodies is described with blackbody equivalent radiometric temperature, the brightness temperature. Brightness temperature is defined as the temperature of a blackbody that emits the same brightness as the scene being measured

$$I_f(\theta,\phi) = \frac{2k}{\lambda^2}T_B(\theta,\phi) \tag{2-7}$$

where T_B is the brightness temperature. The measured brightness is generally a function of θ and ϕ which are the spherical coordinates of a field point. Blackbody radiates the maximum amount of energy and all other bodies at the same temperature radiate equal or less depending on the material emissivity. Emissivity varies between $0 \ldots 1$ and the radiated brightness of a grey body is given by εI_f. If this is equated with 2-7 we have

$$\varepsilon(\theta,\phi)\frac{2hf^3}{c^2}\frac{1}{e^{hf/kT}-1} = \frac{2kT_B(\theta,\phi)}{\lambda^2} \tag{2-8}$$

And by solving this for T_B we have a relation between physical temperature and brightness temperature

$$T_B(\theta,\phi) = \varepsilon(\theta,\phi)\frac{hf/k}{e^{hf/kT}-1} \approx \varepsilon(\theta,\phi)T \tag{2-9}$$

For a blackbody with $\varepsilon = 1$, the above relation can be used to convert the thermodynamic temperature of a blackbody to the brightness temperature of a blackbody.[4][5] If the Planck's quantum effects are not accounted and the blackbody thermodynamic and brightness temperatures are assumed equal an error close to 3% is found for the cryogenic load at $77K$ and $89GHz$. This is discussed in chapter 6.

Emissivity is related to material reflectivity by

$$\varepsilon(\theta, \phi) = 1 - |R(\theta, \phi)|^2 \tag{2-10}$$

where R^2 is the power reflectivity.[6],[1]

Scene brightness may vary with direction and it is a function of spherical angles θ and ϕ. This dependence was expressed as $I_f(\theta, \phi)$ for brightness. Power received by an antenna is given by

$$P_A = \frac{1}{2} A_e \int_f^{f+B} \iint_{4\pi} I_f(\theta, \phi) F_n(\theta, \phi) d\Omega df \tag{2-11}$$

where A_e is the effective antenna aperture, $F_n(\theta, \phi)$ is the normalized antenna power pattern with a directional distribution. The brightness is weighted with antenna power pattern and integrated over a solid angle of 4π presenting the whole sphere surface. This yields spectral power per unit bandwidth which is further integrated over a bandwidth B. The measured brightness is unpolarized and the antenna is polarized and therefore the antenna detects only half of the power. Therefore the factor ½ is introduced. Consider an idealized situation where a lossless antenna is enclosed in an ideal blackbody chamber that has constant temperature T over a bandwidth $B \ll f^2$. Then the brightness will be constant at all directions having a value $I_f(\theta, \phi) = I_c = 2kT/\lambda^2$. From antenna theory the beam area is known to be $\Omega_A = \lambda^2/A_e$. Introducing these results to eq. (2-11) leads to

$$P_{bb} = \frac{1}{2} A_e I_c \Omega_A B = \frac{1}{2} A_e \frac{2kT}{\lambda^2} \frac{\lambda^2}{A_e} B = kTB \tag{2-12}$$

This is the fundamental result used in microwave radiometry. It relates the temperature directly to the power. The above analysis was given to a blackbody, but this result can

be generalized to $P = kT_B B$, where T_B is the brightness temperature. A closely related concept to the brightness temperature is the antenna temperature. When brightness temperature of the scene is observed with an ideal antenna without atmospheric distortions, the antenna temperature equals the brightness temperature, $T_A = T_B$. In this thesis this is generally assumed if not explicitly stated otherwise. [6],[1]

According to thermodynamics, mean kinetic energy of an electron in a conductor is proportional to the temperature T. For a conductor of resistance R this random motion produces small Gaussian distributed random voltage fluctuations at the terminals of the resistor proportional to its temperature, called the Johnson noise. This voltage has the average value of zero, but the average power is given by Rayleigh-Jeans approximation. The rms voltage of the resistor is given by [7]

$$V_n = \sqrt{4kTBR} \tag{2-13}$$

where k is Boltzmann's constant and B is the bandwidth of the system. When a matched load resistor is connected to the described noisy resistor the maximum power delivered to the load in a bandwidth B, is

$$P_n = \left(\frac{V_n}{2R}\right)^2 R = \frac{V_n^2}{4R} = kTB \tag{2-14}$$

This is the same result previously found as the power collected by an antenna enclosed in the blackbody chamber. Imagine that the antenna terminals are connected to a matched resistor at the same temperature as the blackbody through a matched transmission line. The antenna delivers power equal kTB to the resistor through the transmission line. The Johnson noise in the resistor causes noise power to be transmitted through the transmission line to the antenna. The antenna radiates this power towards the walls of the blackbody chamber where the power is absorbed. If the delivered and received powers at the resistor were unequal, the resistor would either gain or lose energy leading to a violation of second law of thermodynamics. Therefore, the power delivered by the resistor equals the power picked by an antenna surrounded by a blackbody.[8]

If an arbitrary noise source is white i.e. its noise spectral density is frequency independent it can be modeled as an equivalent thermal noise source and characterized by equivalent noise temperature. If the noise source delivers a noise power P_{ns} to a load resistor R it can be replaced by a noisy resistor with value R at temperature T_e. This equivalent temperature T_e is chosen in a way that it delivers the same power to the load as the noise

source that it models i.e. $P_{ns} = P_n = kT_eB$. Components and systems such as receivers can then be characterized by equivalent noise temperature with some fixed bandwidth B. Another way to characterize noisy microwave components is the noise figure. Noise figure is a measure of signal-to-noise ratio degradation from the input to the output of a component. When a signal is applied to a noiseless system the signal-to-noise ratio remains the same. In practice all components are noisy and hence increase the noise power at the output leading to a reduction of signal-to-noise ratio. The noise figure F is defined as

$$F = \frac{S_{in}/N_{in}}{S_{out}/N_{out}} \tag{2-15}$$

here S_{in} and N_{in} are the input signal and noise powers, and S_{out} and N_{out} are the output signal and noise powers. Equivalent noise temperature T_e and noise figure F are related by

$$T_e = (F - 1)T_0. \tag{2-16}$$

Noise figure is defined for a matched input source that consists of a resistor at temperature $T_0 = 290K$. Noise figure and equivalent noise temperature are interchangeable when noise characteristics of a component or a system are described.[7]

2.3 Theory of waveguides

Rectangular waveguide can support transverse electric (TE) and transverse magnetic (TM) waves. TE waves have magnetic, but no electric field in the direction of propagation. For TM waves there exists electric field, but no magnetic field in the direction of propagation. Propagation constant for TE and TM modes is given by

$$\beta = k\sqrt{1 - (f_c/f)^2} \tag{2-17}$$

where the wavenumber $k = \omega\sqrt{\mu\varepsilon}$. Propagation constant is real for all propagating modes where $k > k_c$. The cutoff wavenumber $k_c = k^2 - \beta^2$. All modes have a cutoff frequency given by

$$f_{c,mn} = \frac{1}{2\pi\sqrt{\mu\varepsilon}}\sqrt{\left(\frac{m\pi}{a}\right)^2 + \left(\frac{n\pi}{b}\right)^2} \quad (2\text{-}18)$$

where a and b are the width and the height of the waveguide respectively. The mode with the lowest cutoff frequency is the dominant mode. For a standard rectangular waveguides $a > b$ and hence the dominant mode is TE_{10}. All modes that have lower cutoff frequency than the given operating frequency can propagate, modes with $f_c > f$ have imaginary propagation constant, indicating that such field components will decay exponentially from the source of excitation. Wave impedance is also imaginary and no net transfer of power can occur. Such modes are evanescent modes i.e. cutoff modes. Waveguide is said to be overmoded if more than one mode is propagating. Waveguide frequency bands are defined in a way that only the dominant mode is supported and no other modes can propagate. The propagation constant and wave impedances are non-linear functions of frequency for non-TEM modes and therefore the waveguide is dispersive. Guide wavelength is always greater than the free space wavelength and it is given by

$$\lambda_g = \frac{\lambda}{\sqrt{1-(f_c/f)^2}} \quad (2\text{-}19)$$

and wave impedance for TEmode is

$$Z_{mn}^{TE} = \frac{\eta_0}{\sqrt{1-(f_c/f)^2}} \quad (2\text{-}20)$$

where η_0 is the free space impedance.[7]

Waveguide transmission losses can be evaluated by replacing propagation constant with its complex-valued version $\beta_C = \beta - i\alpha$, where α is the attenuation constant. The field components in z-direction is given by

$$E_z = e^{-\alpha z}e^{-i\beta z} \quad (2\text{-}21)$$

The attenuation constant is a sum of dielectric losses and conductor losses, $\alpha = \alpha_d + \alpha_c$. For small loss dielectrics the attenuation can be approximated with

$$\alpha_d = \frac{k^2 tan\delta}{2\beta} [Np/m] \tag{2-22}$$

where $tan\delta$ is the loss tangent of the dielectric. This result applies to any TE or TM wave as long as the waveguide is completely filled with the dielectric.

Conductor losses for TE_{10} mode can be calculated with

$$\alpha_c = \frac{R_s}{\eta b} \frac{\left(1 + \frac{2b}{a}\frac{f_c^2}{f^2}\right)}{\sqrt{1 - \frac{f_c^2}{f^2}}} [Np/m] \tag{2-23}$$

where R_s is the surface resistance of the conductor and given by

$$R_s = \sqrt{\frac{\omega\mu}{2\sigma}} \tag{2-24}$$

and wave impedance $\eta = \sqrt{\mu/\varepsilon}$. Waveguide wall thickness is assumed to be several skin depths of conductivity σ. For air-filled waveguide the conductor losses dominate and dielectric losses can be neglegted.

2.4 Theory of radiometers

Radiometer is, in terms of detection, a passive device i.e. it does not send out a signal, but merely detects the inherent noise that is generated by all bodies whose temperatures are above absolute zero temperature. The previously discussed Planck's radiation law is the foundation on which radiometry lies. The equivalent radiometric temperature that characterizes emitted power from the scene is given by brightness temperature $T_B = P/kB$. A real material always reflects some of the power and thus does not radiate as much power as a blackbody. A measure of how much power is radiated by a body relative to that radiated by blackbody at the same temperature is the emissivity ε. Emissivity is always $0 \leq \varepsilon \leq 1$, and for a perfect blackbody $\varepsilon = 1$. Brightness temperature is related to physical temperature by emissivity

$$T_B = \varepsilon T = (1 - |R|^2)T \tag{2-25}$$

where R is the complex voltage reflection coefficient. From this we can see that the brightness temperature is always smaller than the physical temperature and that different bodies at the same temperature may have different brightness temperatures depending on their emissivities. This makes it possible to distinguish between materials if their emissivities are known.[7]

Total power radiometer relates input temperature to the output voltage by $U = Gk(T_A + T_N)B$. Here k is the Boltzmann constant, T_N is the radiometer noise temperature and B is the equivalent predetection noise bandwidth of the radiometer and. G is the radiometer gain (in units V/W). If the gain of the radiometer is not stable it will change the output voltage in a way that is indistinguishable from the changes of the scene brightness temperature. These effects can be compensated with frequent enough calibration using at-least two known brightness temperature references. Calibration interval should be shorter than the timescale of the gain instability. Otherwise the error of the radiometer measurements is increased. The gain instability is the most prominent disadvantage of the total power radiometer and other topologies have been developed to overcome this limitation.[1],[9]

Dicke radiometer uses modulation techniques in order to reduce the gain fluctuations. It resembles the Total Power Radiometer with some additional features. A switch is added to the radiometer input that periodically switches between the antenna and a known temperature reference. Switching rate needs to exceed the highest frequency component of the fluctuations. The difference of these two loads is the output of the Dicke radiometer. If antenna and reference load temperatures are equal, the gain variations are fully cancelled. This is called the balanced Dicke radiometer. Unbalanced Dicke radiometer has different values for reference and antenna temperatures and does not fully eliminate the gain fluctuation. For a balanced Dicke radiometer, the resolution arising from the white Gaussian distributed noise, is increased by a factor of two compared to the total power radiometer. To maintain the balanced state, a control circuit is required to adjust the reference load brightness temperature as the antenna temperature changes.[1],[9]

Interferometer with correlation receiver has at least two antennas that are separated by several wavelengths. Both channels usually have individual predetection section. Channels and antenna are identical and antennas are pointed to the same direction. A source will therefore induce a signal with equal magnitude, but with a certain phase

difference to the channels depending on the source direction. The signals after the predetection section are multiplied and send to the square-law detector. When uncorrelated noise voltages from different measurement channels are multiplied together the product has average value of zero. A discrete source produces correlated noise for both channels which produces dc-voltage at the output of the square-law detector. This voltage is proportional to the phase difference of the incident signal at the antennas. It has better resolution than the Dicke receiver and it does not require switching schemes at the input of the radiometer. Since the gain instabilities at both channels are uncorrelated they will not affect the receiver resolution. However the random phase variation at amplifiers of the individual channels can reduce the resolution.[6]

Pseudo-correlation radiometer observes scene and reference load continuously. The two input signals are added by a hybrid coupler and amplified in two parallel amplification chains. After amplification a second hybrid follows that separates the signals, after which they are detected. One of the amplification chains is switched in phase, thus producing alternating scene-load signal at the output branches of the second hybrid. Using this technique both signals (reference and scene) have the same gain fluctuations that can be eliminated by differencing the two detected output signals. In varying scene brightness temperatures the gain should be dynamically adjusted so that the two voltages would stay balanced. The gain modulation would then be the measure of the observed brightness temperature. This configuration resembles the Dicke radiometer requiring complex balancing schemes.[10]

A more through discussion on the radiometer types is presented in [1],[6] and [9]. The total power radiometer has the simplest architecture and the most compact implementation. Also it does not require complex switching schemes or balanced amplifiers. It also has the potential for best resolution since it spends more time looking at scene compared to other radiometer types. For these reasons the total power radiometer was chosen in this work.

2.4.1 Total power radiometer

The simplest form of total power radiometer consists of an amplifier, a band pass filter, a detector and an integrator. An amplifier simply amplifies the signal from an antenna in order to provide strong enough signals for the detection. Filter provides the selectivity and integrator smoothes the signal to reduce noise and fluctuations at the detector out-

put. It is desirable to use square-law detector since it relates the output voltage directly to the input power and hence to the input brightness temperature. The average output voltage can be expressed by

$$\bar{U}_{out} = \gamma GkB(T_A + T_N) \tag{2-26}$$

where T_A is the antenna temperature, T_N is the noise temperature of the receiver, G is the predetection RF-gain, B is the equivalent predetection bandwidth, k is the Boltzman's constant and γ is the voltage sensitivity of the square law detector. The theoretical resolution of a total power radiometer is given by *ideal radiometer equation*

$$\sigma_T = \frac{T_A + T_N}{\sqrt{B\tau}} \tag{2-27}$$

where σ_T is the standard deviation of the output voltage and τ is the postdetection integration time. From this equation some basic properties of radiometer measurements can be observed. Increasing the noise temperature will increase the deviation at the output. This will also increase the mean value at the output and from this it is easy to see that keeping receiver noise as low as possible is important. Otherwise the measurement would be dominated by the receiver's own noise. It can also be seen that increasing integration time or the bandwidth the output fluctuations are reduced. There are of course some practical upper limits in bandwidth and integration time that are discussed later on.[9]

The presented equation holds for ideal radiometer and neglects other types of error. One serious error comes from gain fluctuations, the $1/f$ noise that occurs at active devices. When system is calibrated with a certain gain that changes by the time the scene is measured, an error is produced. *Practical radiometer equation* is given by

$$\sigma_T = (T_A + T_N)\sqrt{\frac{1}{B\tau} + \left(\frac{\sigma_g}{g}\right)^2} \tag{2-28}$$

where σ_g/g is the standard deviation of fractional gain fluctuation within the integration interval. From the above relation it is clear that the gain fluctuation degrades the radiometer resolution if sufficient amplifier stability is not reached. This is the main drawback of total power radiometer and for this reason one often uses other topologies (e.g.

Dicke switching) that can suppress these fluctuations. However, modern advances in MMIC (Monolithic microwave integrated circuit) designs have made it attractive to use total power radiometer for its simplicity and best theoretical resolution. However, careful design practice and frequent calibration must be used to overcome this limitation. [9]

The total power radiometer can be implemented as a heterodyne configuration or with a direct detection. With heterodyne configuration the measured signal is downconverted with local oscillator and mixer prior to detection. In the direct detection the detection happens at the RF frequency. This makes it possible to exclude the high frequency mixer and LO (local oscillator). The direct detection has potential benefits over heterodyne configuration e.g. simpler structure, smaller size and weight, lower power consumption, no LO leakage and better frequency stability in the absence of LO. However, direct detection has its drawbacks mainly from the component availability. The IF (intermediate frequency) stage amplification has better quality in terms of stability and there is need for smaller RF gain with delicate amplifiers.[11][12] However, the availability of modern MMICs favors the direct detection especially when the size and weight constraints are considered. For these reasons the direct detection was chosen for both total power radiometers in this work.

3 SYSTEM DESCRIPTION

Two radiometers at frequencies $36{,}5GHz$ and $89GHz$ are designed to be used for unambiguous detection of oil film thickness on water. Both radiometers are made by cascading waveguide components. The radiometers require bias electronics, temperature stabilization circuitry and analog-digital-converter (ADC). The ADC measures the radiometer output voltages, bias currents and internal calibration load temperature as well the radiometer temperature itself. This data is sent through serial peripheral bus to the FPGA where some averaging is made in order to avoid too vast data blocks. Software that generates the thickness data from digitized measurements is run on PC.

Parabolic antenna with waveguide feed horns is used as an antenna to measure the sea surface. The radiometer system is designed to be mounted on a ship mast. Both radiometers are designed with waveguide interfaces to the feed horns. The system requires two onsite calibration loads. A matched load is used as cold load and a matched load with added noise power from a noise diode as the hot load. To determine the noise diode power accurately a factory calibration is required. For factory calibration a cryogenic load is used with the matched load.

Figure 3-1 shows the general description of the radiometer measurement system. It consists of three modules: radiometer box, temperature stabilization circuitry and control and interface module. The temperature stabilization circuitry is a commercial unit that is controlled by the control and interface unit. The Peltier element is driven with a pulse-width-modulated (PWM) signal. The temperature of the radiometer is monitored and the information is sent back to the control unit. The temperature sensor is mounted near the Peltier element which in turn is located near the first two LNAs which are considered to be the most prominent source of instability due to temperature variations. The control and interface module receives the samples from the ADC, generates the general-purpose-input-output (GPIO) controls and handles the link to the user interface PC where the computing algorithms of slick thickness analysis are run. The signals that are measured with ADC from both receiver channels are:

- LNA bias currents
- Noise diode bias current
- Internal calibration load temperature
- Radiometer temperature
- Ambient temperature

- Diode detector output voltage

It has been found in [13] that HEMT amplifiers exhibit strong correlation between gain fluctuations and drain current fluctuations. It has also been suggested that there is possibility of using the measured drain currents to reduce some of the low frequency gain fluctuations from the amplifiers. Preliminary results have shown ≈30% reduction in low frequency gain fluctuations with 30GHz cryogenic amplifiers. The possibility of using this technique relies on careful measurement of LNA bias currents which is achieved using precision low noise instrumentation amplifiers.

One of the suggested reasons for instability of the noise diode (ND) is the fluctuations at the bias currents that drive the ND [14]. Measuring ND bias currents excludes one instability mechanism and presents more freedom on analyzing the radiometer measurements.

High precision waveguide loads are used for calibration. This is a simple way to produce an accurate load since the physical and brightness temperatures can be accurately related. This leads to the need of accurately measuring the physical temperature of the load which is done with high precision PT1000 sensor.

Major cause of overall instability is caused by temperature variations [1]. Therefore, the radiometer itself is enclosed in a temperature stabilized box. The possible temperature drifts are monitored and compared to the measured video signal for correlations. Similarly the ambient temperature is recorded to see if measured video signal correlate with ambient variations. The radiometer box is thermally insulated enclosure with metal shielding. All signal feedthroughs are filtered while the metal enclosure assures that the box is a Faraday's cage for all unwanted noise signals.

The measured video signals from the diode detector are in order of millivolts and are amplified with low noise operational amplifier before AD-conversion.

In addition to measuring, the ADC has GPIO control signals for both receivers:

- Noise diode on/off
- Waveguide switch position

Noise diode bias current is simply turned on and off when calibration is needed. GPIO lines are used as an enable for the bias circuitry. The waveguide switch is located at the input of the radiometer and it has a DC-motor that is driven by H-bridge driver which in turn is driven by logic values from the GPIO lines.

The connecting network in Figure 3-1 illustrates the possibility of connecting both the antenna and cryogenic load to the radiometer inputs. In practice there are two connecting networks for the two calibration procedures that are described in chapter 4. Both of these connecting networks consist of waveguide tubes and a waveguide switch. In factory calibration mode a cryogenic load is connected to the radiometer input. In on-site calibration mode it is connected to the feed horn as discussed and there is no possibility of connecting the cryogenic load to the input of the radiometers. The cryogenic load and the microwave parts of the radiometer are discussed thoroughly later on.

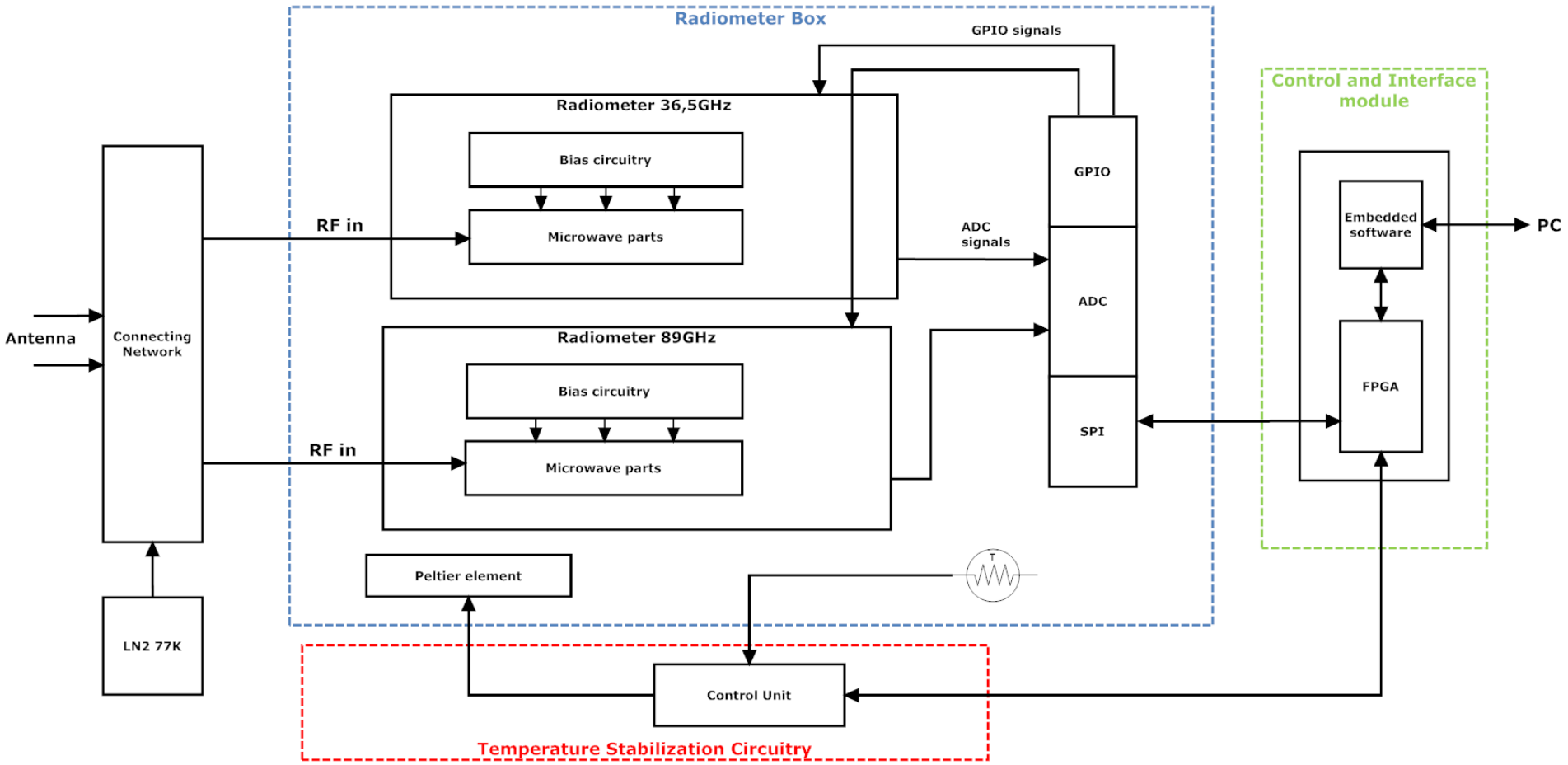

Figure 3-1 Simplified description of the radiometer system. The system consists of temperature stabilization circuitry, radiometer box, connecting network and control electronics with user interface PC.

4 CALIBRATION

Calibration is used to accurately relate radiometer output voltage to the input brightness temperature. If full knowledge of all component characteristics was available, the behavior of the radiometer would be perfectly known. This, however, is not the case and the behavior of a practical radiometer has to be corrected by frequent calibration. Square law detector relates output voltage linearly to the input power. With the assumption of linear radiometer transfer function, two input noise sources are needed to calibrate total power radiometer. This creates a calibration line that relates input brightness temperature to output voltage. The accuracy of calibration is mainly determined by the accuracy of used calibration references. A matched load (with $\varepsilon = 1$) brightness temperature can be determined by measuring and controlling its physical temperature. A common way to create known calibration loads is to use precision termination and vary its physical temperature. For the hot load, an ambient temperature termination can be used. To achieve low temperatures, a microwave termination can be submerged into a liquid with a low boiling point, referred as cryogenic load. Most commonly liquid nitrogen (LN2) is used. Another possibility for the cold load is to use an antenna connected to the radiometer and view an absorbing material saturated with LN2. A high quality absorber has emissivity close to unity and hence its brightness temperature can be known accurately if the LN2 boiling point is known.

In this thesis two calibration procedures are presented: *factory calibration* and *on-site calibration*. For on-site calibration it would be impractical to have cryogenic load available at all times and therefore much more compact noise diode is used. The on-site calibration is frequently performed when radiometers are used in the field. For this two known temperature references are developed. The cold load is a matched load at ambient temperature. The hot load is a switched noise diode that couples extra noise power on top of the matched load. Calibration interval should be shorter than the timescale of the gain instability. The exact coupled noise diode temperature is obtained in factory calibration. The factory calibration is done much more infrequently where the interval of factory calibration is determined by the stability of the noise diode. An ambient temperature matched load is used as hot load. A cryogenic load is used as cold load which is discussed in chapter 6. [15][1]

Simulation model in the next section simulates the used on-site calibration procedure. The simulation model assumes that the noise diode is perfectly known and stable. Equa-

tions that can be used for factory calibration are also presented. Rest of this chapter discusses error arising from gain fluctuations and mismatches and shows that the overall radiometer resolution is limited by the low frequency gain fluctuations. Even though the actual radiometer is not yet discussed, following simulations are general in a way that all total power radiometers can be described in the same manner.

Simulation results presented in this chapter are based on estimated performance of the designed radiometers. The parameters used throughout the simulations are given in Table 1. Thorough discussion of radiometer parameters is given in chapter 5. Note that for the $89GHz$ radiometer a conservative noise temperature estimate was used. The noise temperature obtained from the actual system design is somewhat smaller due revaluation of losses at the radiometer input.

Table 1 Radiometer parameters used in the calibration simulations.

	Radiometer Ka-band	RadiometerW-band
Frequency	36,5GHz	89GHz
Bandwidth	450MHz	4GHz
Noise Temperature	450K	1150K

4.1 Measurement uncertainty from the calibration loads

Finite resolution of calibration load measurements degrades the overall radiometer resolution even if full knowledge of calibration loads is present. This problem is described next and followed by a MATLAB simulation model that estimates the nature of the error. After this, results from the model are presented.

4.1.1 Problem statement

One error source degrading ideal radiometer resolution arises from the measurement of the calibration loads. Even if we assume perfect knowledge of the calibration loads, the corresponding calibration measurements always include some uncertainty in the same way as the scene measurements made by the radiometer i.e. the same uncertainty is present for the calibration load measurements as there is for the actual target described by

the ideal radiometer equation. It would be preferable to use calibration source temperatures that are just above and below the target temperature. A common practice is to use a cryocenic load, but for onsite calibration this is not possible. Therefore a matched load at ambient temperature is used for cold load. Hot calibration load is created by injecting extra noise power on top of this temperature. This means that both calibration points are at higher temperatures than the target. This leads to an error referred here as an extrapolation error. This means that radiometer response (that is assumed linear) has an error in its slope and the error is different with consecutive calibrations. Figure 4-1 depicts the principle of obtaining the radiometer response.

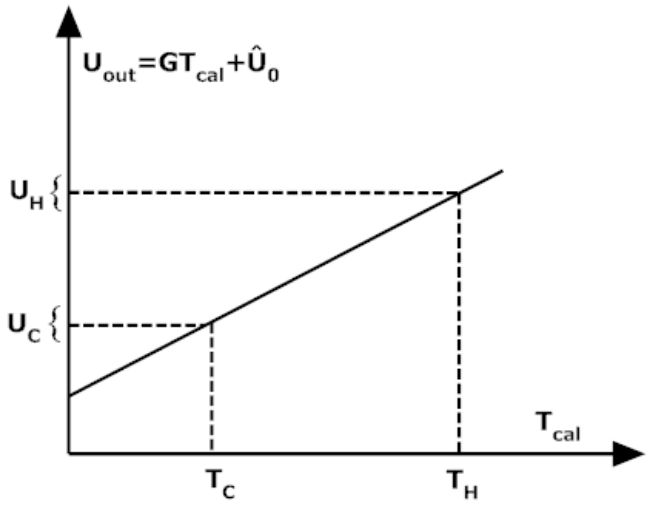

Figure 4-1. Radiometer calibration with two loads. A set of brightness temperature measurements that correspond to a set of radiometer output voltages [16].

4.1.2 Simulation model

Measured voltage from the detector output and the radiometer input power are related by

$$U_{out} = G(T_A + T_N)^{\alpha} + U_0 \qquad (4\text{-}1)$$

where U_0 is the offset of the video amplifier. If we assume the radiometer response to be perfectly linear i.e. $\alpha = 1$, the equation (4-1) reduces to

$$U_{out} = GT_A + \hat{U}_0 \tag{4-2}$$

where $\hat{U}_0 = GT_N + U_0$. Now we have two unknowns, gain and a combined offset value. Thus the needed amount of calibration points (sources with known brightness temperature) for total power radiometer is two. Here it has to be noted that gain has a wider meaning than it had in equation (2-26). The detector voltage sensitivity, Boltzmann constant and bandwidth are also included to gain and it has units $[V/K]$. Equations (4-3) to (4-6) show the possible measurements that the system can make in the *on-site calibration*.

$$U_1 = GT_C + \hat{U}_0 \tag{4-3}$$

$$U_2 = GT_H + \hat{U}_0 \tag{4-4}$$

$$U_3 = GT_A + \hat{U}_0 \tag{4-5}$$

$$U_4 = G(T_A + T_{ND}) + \hat{U}_0 \tag{4-6}$$

Where T_C, T_H, T_A and T_{ND} are the cold load temperature, hot load temperature, antenna temperature and noise diode temperature respectively. We have three unknowns, $G, \hat{U}_o$ and T_A and four equations. This overdetermined system of linear equations is solved by least squares method. However, a new variable has to be presented to the equation (4-6), $U_{AG} = GT_A$, in order to keep the system linear. The unknowns are solved first and then T_A is obtained by dividing U_{AG} with the solved gain estimate. The calibration equations can be presented in the following form:

$$\begin{pmatrix} U_1 \\ U_2 \\ U_3 \\ U_4 \end{pmatrix} = \begin{pmatrix} T_C & 1 & 0 \\ T_H & 1 & 0 \\ 0 & 1 & 1 \\ T_{ND} & 1 & 1 \end{pmatrix} \begin{pmatrix} G \\ \hat{U}_0 \\ U_{AG} \end{pmatrix} \tag{4-7}$$

The cold, hot and noise diode temperatures are assumed to be known. Voltages are also known from measurements. The values of G=1 and $\hat{U}_o = 0$ are used, but these are not told to the model. The actual numerical values in this simulation are irrelevant. For each measurement, white Gaussian noise is added with standard deviation given by the ideal radiometer equation. Each measurement is cyclically viewed, and this cycle is repeated

at least 1000 times. From these calculated estimates, the overall standard deviation of the scene is calculated as a function of various variables shown in the next section.

4.1.3 Simulation model results

In Figure 4-2 radiometer uncertainty is plotted for various calibration loads pairs as a function of the unknown antenna temperature. This deviation in measured voltages has the greatest effect when the calibration load temperatures are close to each other. Also the error always increases when the antenna temperature T_A is moved further from the calibration loads. Similar results are obtained in [16] where an equation for radiometer resolution is derived that includes the described error from calibration sources. However the presented model offers more flexibility regarding additional sources of error e.g. drifts and offsets in temperature sources can be added. From the simulation results it can be noted that uncertainty of the ideal radiometer cannot be achieved. One of the plotted curves evaluates the possibility of using a novel semi-conductor based active cold load technology with estimated brightness temperature of 100K. Active cold loads are described for e.g. in [15]. If such a load was present in the onsite calibration the calibration loads would be closer to the scene temperature. It would make possible to have calibration loads at above and below the target temperature range. This would greatly reduce the described error.

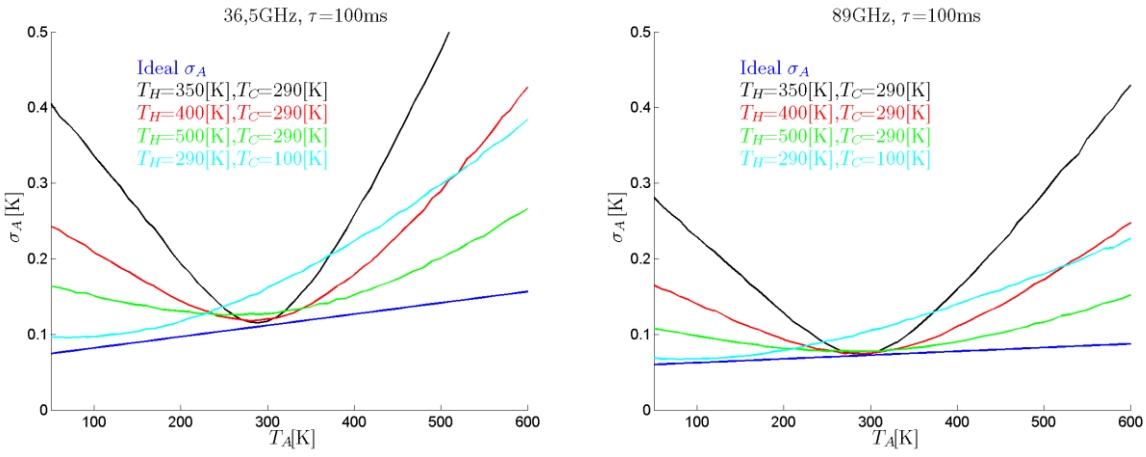

Figure 4-2 Radiometer uncertainty as function of target temperature for various calibration load pairs for both receivers with integration time of 100ms at each load.

With the presented simulation model the target noise diode temperature can be estimated. With the presented simulation model the radiometer uncertainty is plotted as a function of noise diode temperatures with scene temperature of 150K and 100ms integration times for each load. From this it can be seen that the noise to be added on top of the ambient temperature load is 200K or more. There is no absolute limit how much noise can be injected, but increasing the noise power adds the requirement of the receiver dynamic range where the radiometer needs to be linear. The range of 200K to 400K is chosen for the noise diode temperature to be injected to the radiometer channels. Figure 4-2 and Figure 4-3both show that the W-band radiometer has better resolution. These simulations have however neglected a prominent source of error in total power radiometer, the $1/f$ noise. This is discussed in the next section.

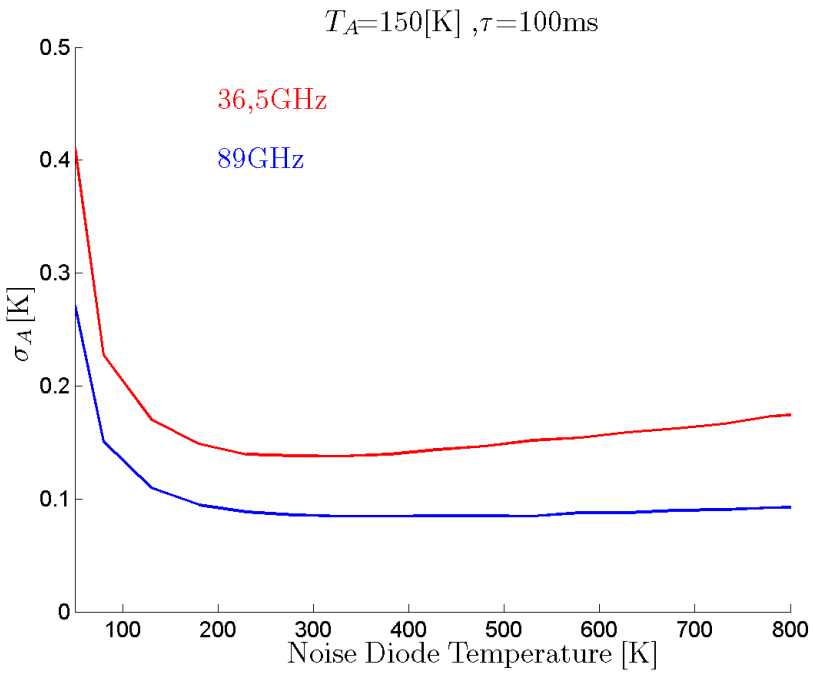

Figure 4-3 Radiometer uncertainty for various noise diode temperatures for antenna temperature of 150K for both channels with integration time of 100ms at each load. T0=290K and perfect knowledge of calibration loads are assumed.

The factory calibration procedure is similar to the on-site calibration that was presented. In the on-site calibration the noise diode temperature was assumed to be known. This knowledge is obtained in factory calibration. The possible measurements that the sys-

tem can make in the *factory calibration* are presented below. T_C are T_H are the cold and hot load temperatures. Cold load is achieved by cooling an absorber material with liquid nitrogen. The hot load is the same matched load at ambient temperature that was used as a cold load in on-site calibration. Both of these reference load temperatures are known by design. The three unknowns, $G, \hat{\mathrm{U}}_o$ and T_{ND} are solved in the same manner as the unknowns in the on-site calibration. The variable that is presented to keep the system linear is $U_{NDG} = GT_{ND}$. The unknowns are solved first and then T_{ND} is obtained by dividing U_{NDG} with the solved gain estimate. The calibration equations can be presented in the following form:

$$\begin{pmatrix} U_1 \\ U_2 \\ U_3 \\ U_4 \end{pmatrix} = \begin{pmatrix} T_C & 1 & 0 \\ T_H & 1 & 0 \\ T_C & 1 & 1 \\ T_H & 1 & 1 \end{pmatrix} \begin{pmatrix} G \\ \hat{\mathrm{U}}_0 \\ U_{NDG} \end{pmatrix} \tag{4-8}$$

The same results that were obtained for the on-site calibration apply to the factory calibration also. When the noise diode temperature is obtained in factory calibration it has some error in it. This is a bias error in the on-site calibration since the obtained single value is used throughout until the next factory calibration. By measuring the noise diode temperature with the given procedure multiple times and averaging these measurements the error can be reduced to obtain more repeatable factory calibration values.

4.2 Uncertainty from 1/f noise

If the radiometer noise was white, the resolution could be improved indefinitely with integration time. In practice, there is a limit in the radiometer resolution that can be reached. Radiometer noise is usually modeled with two types of noise sources, white Gaussian distributed (non-correlated) and $1/f$ (correlated) noise[4]. These are caused by unrelated mechanisms and may be considered statistically independent. Therefore the radiometer noise is given by $\sigma = \sqrt{{\sigma_T}^2 + (\sigma_g/g)^2}$ which is a squared sum of the variances of both noise components[1]. The amplitude spectral density of the front-end noise contribution referenced to radiometer input is given by

$$\sigma_T(f) = (T_A + T_N)\sqrt{\frac{1}{B} + \left(\frac{\sigma_g(f)}{g}\right)^2} \tag{4-9}$$

An empirical model describing the gain fluctuations is given in [17]

$$\frac{\sigma_g(f)}{g} = \frac{2A\sqrt{N_s}}{\sqrt{f}} \tag{4-10}$$

Here N_s is the number of amplifier stages and A is a normalization constant. Number of stages used are 9 and 12 for the Ka-band and for the W-band, respectively. The normalization constant can vary considerably. Estimates of $1{,}8 * 10^{-5}$ and $2{,}5 * 10^{-5}$ are obtained from [17]. In Figure 4-4 the amplitude spectral density is plotted for both radiometer channels. It can be observed that white noise component is smaller in the W-band radiometer as observed earlier. This is due to the much wider predetection bandwidth. However, the $1/f$ component of the noise is more prominent with the W-band radiometer. This is due to the number of amplifying stages in the LNA chips and for the larger normalization constant. The model shows that the knee frequency i.e. the frequency where power spectral densities of the noise components are equal, is higher for the W-band radiometer. It is also evident, that the $1/f$ component of the spectrum is higher for the W-band radiometer. This means that the optimum integration time will be shorter for the W-band than for the Ka-band radiometer and that the overall resolution will be better for the Ka-band radiometer due to the better $1/f$ noise performance.

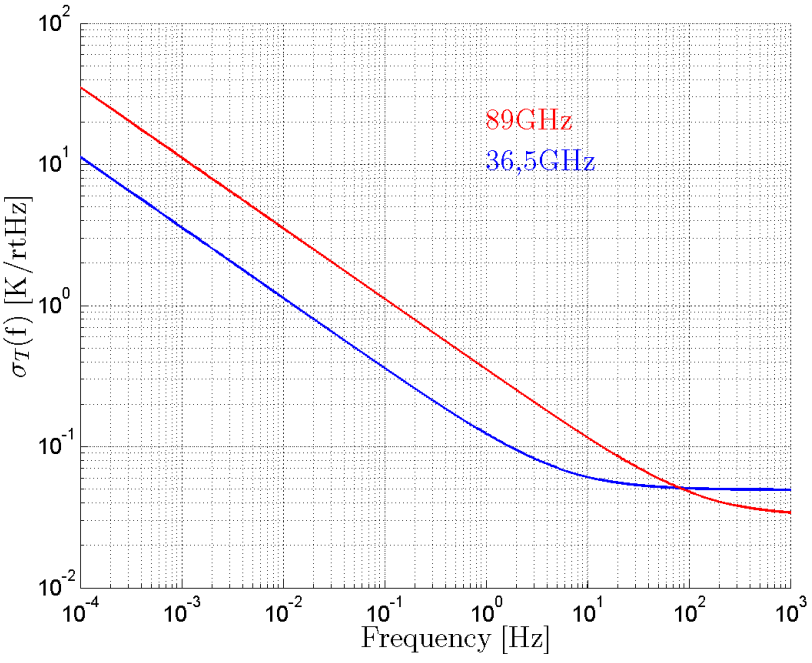

Figure 4-4 Amplitude spectral densities of the front end noise contributions referenced to radiometer input (calibration plane). Antenna temperature of 290K was used.

Allan deviation is an often used measure for the radiometer stability. Unlike the usual standard deviation Allan deviation is based on the standard deviation of measurement differences. Allan variance is defined to have the same value as the standard variance when white Gaussian distributed noise is measured. Allan variance is a two-sample variance, where time average of successive bins is taken. Time average differences are squared and then averaged and divided by two. This is repeated for several integration times. This method provides a way to differentiate between different types of noises in signal. Continuous Allan deviation is given by

$$\sigma_y(\tau) = \sqrt{\frac{1}{2}\langle (y(t+\tau) - y(t))^2 \rangle} \tag{4-11}$$

where

$$y(t) = \frac{1}{\tau}\int_t^{t+\tau} V(t)dt \tag{4-12}$$

$V(t)$ is the measured video signal and τ is the integration time. Allan deviation can also be calculated in frequency domain. By taking a Fourier transformation from (4-12) the following is obtained

$$\sigma_y{}^2(\tau) = 2\int_0^{f_s} S_V(f)\frac{\sin^4(\pi\tau f)}{(\pi\tau f)^2}df \tag{4-13}$$

where S_V is a single sided power spectral density of the amplitude spectral density.[18] Figure 4-5 shows the allan deviation for both radiometer channels calculated with eq. (4-13). From the plots it can be seen that the integration time for the Ka-band radiometer is limited to about $1s$ where as to the W-band the limit is around $100ms$. The model assumes $1/f^{\alpha}$ noise spectra with $\alpha = 1$, but alpha can vary considerably between different amplifiers. From literature review in [19] it has been found for High-Electron-Mobility-Transistors (HEMT) to lie between $0{,}7 \ldots 1{,}3$. Gallium nitride (GaN) HEMT literature describes slopes of $1 \ldots 1{,}3$ and Gallium Arsenide (GaAs) HEMT literature $0{,}7 \ldots 1$. The actual slope is interesting in radiometry since in the used model an optimum integration time is found after which the radiometer resolution can not be improved. However, if the actual slope had $\alpha < 1$ for the amplifiers, the fluctuations could be suppressed by increasing integration time. If the slope is steeper, $\alpha > 1$ the Allan deviation would have a minimum at some integration time and further increase in the integration time would in fact lead degraded performance. For the Ka-band radiometer it is assumed to be somewhat below 1, but for the W-band no such

assumption can be made since the manufacturing process of the chips is unknown. It has also been found that low frequency fluctuations increase significantly when increasing drain voltage of HEMT. With changes in gate voltage and hence in the drain current, no significant changes are found. This implies that optimum bias conditions for radiometer can be found by low drain voltage.

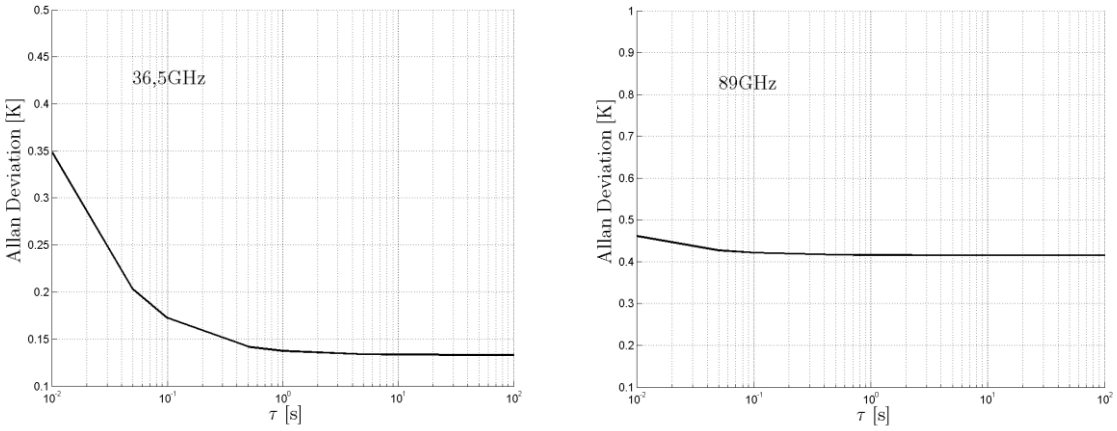

Figure 4-5 Allan deviation of the front-end for both radiometers reduced to the radiometer input calculated from the front-end amplitude spectral density noise models). Antenna temperature of 290K was used in the simulation. Note the different scale on y-axis

More thorough treatment on different variances and their uses are found in [18] that explain the shortcomings of the standard Allan deviation and proposes better choices to be used for the actual scene measurements.

4.3 Uncertainty from mismatches

Variations in reflections, losses and in gain beyond the receiver calibration plane can be factored out by the calibration process, if calibration is done frequently enough. The most detrimental factor affecting these is the temperature fluctuations leading to the importance of keeping the radiometer temperature at a constant value during the calibration where different loads are viewed cyclically. In practice, this means that temperature stabilization of the radiometer is required or radiometer calibration is inaccurate. There is, however, another source of error which has not yet been addressed, namely the mis-

matches between different temperature loads that are connected to radiometer input during the calibration cycle. Mismatches here are defined as differences in reflections and insertion losses between radiometer input and different loads. The problem is how to relate input brightness temperature to the output voltage of the radiometer without the error induced by the mismatches.

All different loads are connected to the radiometer input via a lossy two-port network which is characterized by scattering matrix shown in Figure 4-6. The connecting network, in this design, consists of waveguide switch and waveguide tubing (any passive, linear and time-invariant network is valid). The connecting network is inevitably different for all loads leading to mismatches that introduce an error to the measured scene brightness temperatures if not corrected. The properties of the connecting network can be measured with VNA (Vector Network Analyser). A relationship between a noise temperature of a noise generator (calibration reference or antenna) and T_{IN} has to be developed for this correction.

Equation (4-14) shows all the components that contribute to the measured input temperature T_{IN}. T_G is the generator noise temperature that is being measured, T_0 is the physical temperature of the connecting network and T_R is the effective receiver temperature. This usually is not the noise temperature of the receiver reduced to the input, since an isolator is typically used somewhere at the receiver front-end before amplification. Isolators serve as a low loss signal path for one direction and a high loss for the other and therefore emitting brightness temperature equal to a resistor (with emissivity at unity) towards the generator. Terms α_m are γ known as the micmatch loss factor and transmission factor respectively.[1]

Consider a case where radiometer is calibrated with two known calibration references. When calibration references are measured that have noise generator temperatures T_G known by design at $plane\ 1$, the temperatures need to be converted to T_{IN} at $plane\ 2$ (calibration plane) with eq. (4-14). On the other hand, when the scene is measured, the temperature is obtained at $plane\ 2$ which then needs to be converted to T_G at $plane\ 1$ i.e. T_{IN} is known by measurement and T_G is the unknown.

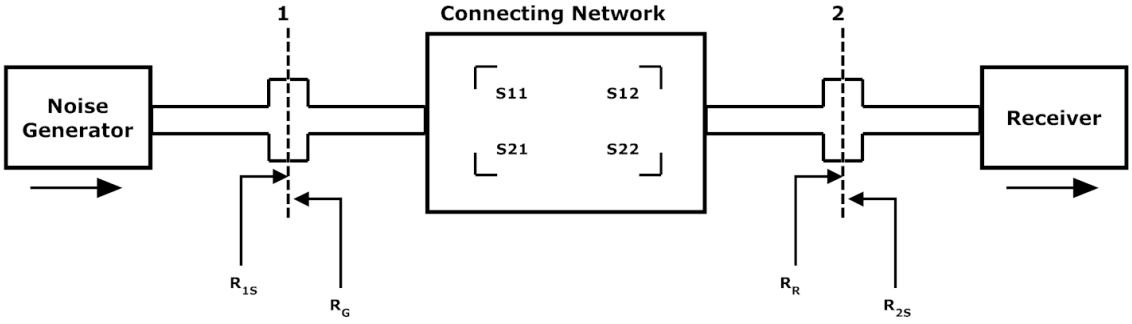

Figure 4-6 Network representation of radiometer front end. Noise generator refers to calibration load or antenna. [1]

$$T_{IN} = \alpha_m \gamma T_G + \alpha_m (1-\gamma) T_0 + (1-\alpha_m) T_R \tag{4-14}$$

where

$$\begin{aligned} \alpha_m \gamma T_G &= net\ delivered\ noise\ temperature\ from\ generator \\ \alpha_m (1-\gamma) T_0 &= net\ delivered\ noise\ temperature\ generated\ by \\ &\quad lossy\ network\ due\ to\ self-emission \\ (1-\alpha_m) T_R &= net\ delivered\ noise\ temperature\ generated\ by \\ &\quad the\ receiver\ and\ then\ reflected\ back\ towards\ the\ receiver \end{aligned} \tag{4-15}$$

$$\alpha_m = \frac{(1-|R_{2S}|^2)(1-|R_R|^2)}{|1-R_{2S}R_R|^2} \tag{4-16}$$

$$\gamma = \frac{1}{L_S}\left[\frac{(1-|R_G|^2)(1-|S_{11}|^2)}{|1-S_{11}R_G|^2(1-|R_{2S}|^2)}\right] \tag{4-17}$$

where

$$R_{2S} = S_{22} + \frac{S_{21}S_{12}R_G}{1-S_{11}R_G} \tag{4-18}$$

$$L_S = \frac{Z_{02}}{Z_{01}}\frac{(1-|S_{11}|^2)}{|S_{21}|^2} \tag{4-19}$$

The connecting network used to connect the antenna to the radiometer input consists of waveguide tubing and a waveguide switch. The switch is used to cycle between the in-

ternal calibration load and a waveguide interface at the radiometer box. Figure 3-1 shows the connecting network to be outside the thermally insulated radiometer box. The waveguide switch and a small part of the waveguide tubing are inside the thermally stabilized radiometer box, but most of the tube connecting an antenna to the radiometer box is not thermally stabilized. The two calibration modes described have different connecting waveguide tubes. Cryogenic load that is used with factory calibration is done at a room temperature with modest temperature fluctuations. In addition the tube between the cryogenic load and the radiometers can be kept short. For these reasons the uncertainty of connecting network mismatch is much larger with the on-site calibration. Therefore the discussion is limited to uncertainty from mismatches with on-site calibration.

The on-site calibration has a parabolic antenna with a feed horn as an antenna. The receiver has an isolator before the first LNA which decouples the radiometer noise temperature from the connecting network and T_R is characterized with the physical temperature of the radiometer $T_{radiometer}$. With thermal control $T_{radiometer}$ is adjusted slightly above the ambient temperature. The radiometer temperature is assumed to be completely constant, and by measuring its complex reflection coefficient and temperature, its contribution in eq. (4-14) can be accurately known. The connecting tube between radiometer input and the antenna assembly has dissipative losses. The tube is also susceptible to ambient temperature variations which is the most prominent error source between T_G and T_{IN} conversions.

The effect of connecting network temperature variations are examined as a function of tube losses. It is fair to assume return loss of $-25dB$ for waveguide tubes if only gradual bends are used. The return loss of the antenna assembly is typically $-25dB$. It can be measured and used in (4-14), but the stability of this term is unknown. Since the antenna does not have any resonating structures and is inherently wideband, small gradual changes in mechanical dimensions are believed to result in insignificant change in the return loss and are here assumed to be constant. The input return losses of the radiometers are evaluated in chapter 8 and a slightly conservative $-22dB$ is used. So far, only the magnitudes of the reflections have been discussed. The phase plays a role in the denominator of (4-16). To get a conservative estimate, a simulation where all phases are changed $0 \dots 2\pi$ is made. The values that give the highest T_{IN} are used to evaluate the effect of the tube loss with temperature variations. This is a conservative estimate on the effect of reflections when the phases are unknown. $T0$ in (4-14) is varied between $270 \dots 310K$ which presents the long term ambient temperature variation in the field

measurements. Generator temperature $T_G = 100K$ presenting the smallest estimated antenna temperature is used throughout the simulation. The mechanical dimensions change with temperature resulting in further variation in the losses and the phase of the tube. These, however, have a clearly smaller effect than the direct change of the self-emitting noise temperature of the tube and are therefore neglected. $T0$ is given to the simulation as a random variable with uniform distribution. A difference from a maximum and a minimum value from a sample of 10000 are taken. This is repeated with a waveguide loss range of $0 \ldots 1{,}5dB$. Also the T_{IN} is plotted as a function of the tube loss. The minimum and maximum curves result from the variable phase with the given magnitudes. The real value for T_{IN} with fixed phases would be found somewhere between the max and min curves. The results are shown in Figure 4-7.

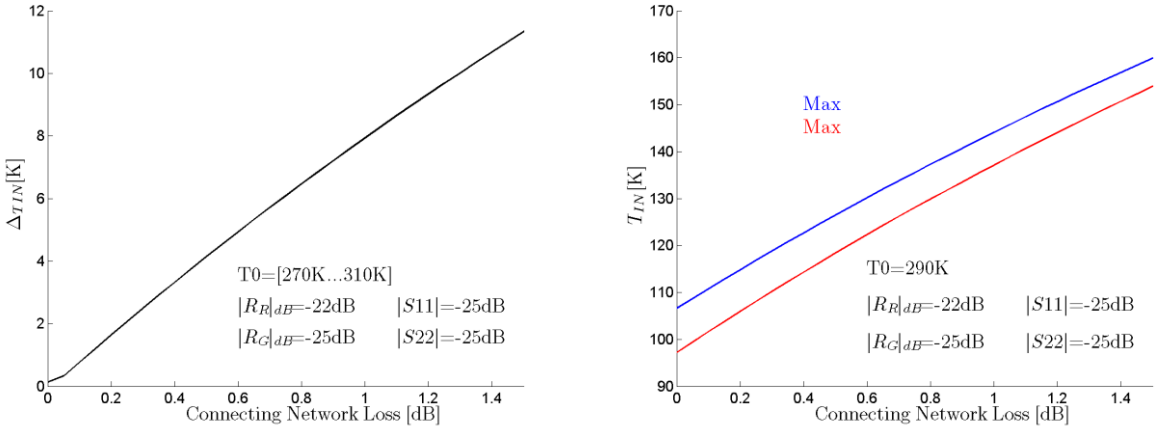

Figure 4-7 Effects of connecting network losses with ambient temperature variation. Left: Uncertainty in T_{IN} when the tube temperature is varied from 270K…310K. Right: Input temperature at the calibration plane as a function of connecting network loss.

It is clear that with the assumption of about 40C temperature variation, very little loss can be allowed between the antenna and radiometer box. For the $89GHz$ radiometer the losses for ideal copper tube are around $2{,}7dB/m$ and about $0{,}5dB/m$ for the $36{,}5GHz$ radiometer. The tube should be much shorter than $10cm$ without serious degradation of radiometric resolution at $89GHz$. This is not achievable. Therefore the temperature variation must be reduced with thermal control or the temperature of the tube must be recorded and used in computations when conversions between T_G and T_{IN} are made.

5 SYSTEM DESIGN

5.1 Specifications

The system is composed of two radiometers. Radiometers are total power radiometers with noise injection and direct detection. Table 2 below summarizes key spesifications for radiometers that are used in the system design. The center frequencies and bandwidth requirements are based on previous study made in DA-Design Ltd. and are given to this work. Maximum signal level comes from the hot calibration source. Minimum signal level to be detected is the bare sea water brightness temperature and is roughly around $100K$. The noise figure has no absolute target value, but since the resolution of the radiometer is adversely affected by receiver noise a small noise figure is desired.

Table 2 Technical specification for both receivers

	Radiometer Ka-band	Radiometer W-band
Frequency	36,5GHz	89GHz
Bandwidth	450MHz	4GHz
Resolution	TBD	TBD
Maximum signal temperature	400	400
Minimum signal temperature	100	100
Integration time	TBD	TBD

5.2 Power level analysis

Gain of the radiometer can be analyzed by the known input power levels and by the desired power at the detector. The input power level at the detector can be calculated by $P_{in} = k(T_A + T_N)BG$. The desired power level at the detector is chosen to be in the linear region of the detector response. There is a trade off when choosing the signal levels. A low level ensures good square law behavior, but results in weak signals which can cause problems on the following amplifier stages.[9] According to the manufacturer data, the square law behavior starts slowly deteriorating at $> -20dBm$ at 30GHz. A level of $-25dBm \ldots -30dBm$ at the detector is chosen to be a good compromise. The needed gain can be evaluated from the bandwidth and receiver noise temperature estimates with $G \geq P_{in}/k(T_A + T_n)BF$. For the chosen LNA type, three LNAs are re-

quired to achieve the desired gain for both channels. More detailed calculations are given later on.

The added noise of the noise diode can be calculated by [20]

$$\mathrm{ENR} = 10\log\left(\frac{\mathrm{T_N}}{290} - 1\right) \tag{5-1}$$

$$T_N = 290\left(10^{ENR/10} + 1\right) \tag{5-2}$$

Based on manufacturer data, the diode Excess Noise Ratio (ENR) can vary between $15dB \ldots 25dB$. It was estimated to be higher at lower frequencies. With target noise injection temperature between $200K \ldots 400K$ for both radiometers, the coupling values of $19dB$ and $17dB$ for Ka-band and W-band couplers were chosen. These, however, need to be checked with the measured noise diode ENR.

5.3 Cascade analysis

Radiometers measure self-emitted noise of objects that usually have smaller brightness temperature as the radiometer noise temperature. Any signal-to-noise ratio degradation prior to amplification directly affects radiometer resolution. Reflection- and loss-free radiometer would not impose any problems concerning the components before the amplification. Nevertheless some components are required before the signal can be amplified. Careful design is needed to keep losses and hence the noise figure at a reasonably low level. A waveguide switch at the input is needed to switch between calibration load and the antenna. Directional coupler is placed after the switch. It is needed to couple noise from the noise diode. The noise diode is simply switched on and off and additional noise is injected through directional coupler to the receiver channel. Now the LNA could be placed, but since the reflection coefficients are usually poor and at this point it is critical to have good matching, an isolator is used. Isolator propagates signal in one direction only i.e. it decouples the output from the input. Therefore, the noise temperature seen by the antenna looking towards the receiver is the temperature of the internal matched load of the isolator. This was analyzed in 4.3. As direct detection is used, the

goal is simply to amplify the signal for detection and filter out the wideband noise picked up by the antenna to the defined bandwidth with a waveguide filter. After the isolator, two LNA chips are cascaded in one mechanical block and a microstrip attenuator is placed between them. Attenuator is used to suppress reflections between LNAs to provide better stability. Integrating components in a single block leads to more difficult implementation, but is required for a more compact mechanical implementation. Amplifiers have a wide gain bandwidth and since the filter will reflect all power outside the filter pass band, an isolator is placed before the band-pass filter to provide good wideband matching. All three amplifiers that are needed to achieve enough gain, could be cascaded in a similar manner as the first two, but the amplifier wideband noise might lead to a compression of the last stage so the filter is placed between the second and the third amplifier. The third amplifier is integrated with the diode detector to one mechanical block. An attenuator is placed between last amplifier and detector to assure good stability for the amplifier. After detection, the signal is amplified in a video amplifier to have sufficient level for AD-converter. Both radiometers have the described configuration and this is shown in Figure 5-1.

Data used in the cascade analysis for each component is based on typical commercial components and values found in the literature. These calculations are repeated with measured values in chapter 8.

The following equations are used in the cascade analysis. Cascaded gain is simply a sum of gains of the individual stages where sums are made over $1\ to\ n$, which represent the first and the last component in the receiver respectively.

$$G_{dB,cascade} = \sum G_{dB,n} \tag{5-3}$$

Noise figure is calculated with Friis equation which is given as

$$NF_{dB} = 10\,log\left(F_1 + \frac{F_2 - 1}{g_1} + \frac{F_3 - 1}{g_1 g_2} + \cdots\right) \tag{5-4}$$

where F_n refers to noise factor of a single component (absolute value of the noise figure). The overall performances of the receivers are presented in Table 3 and Table 4.

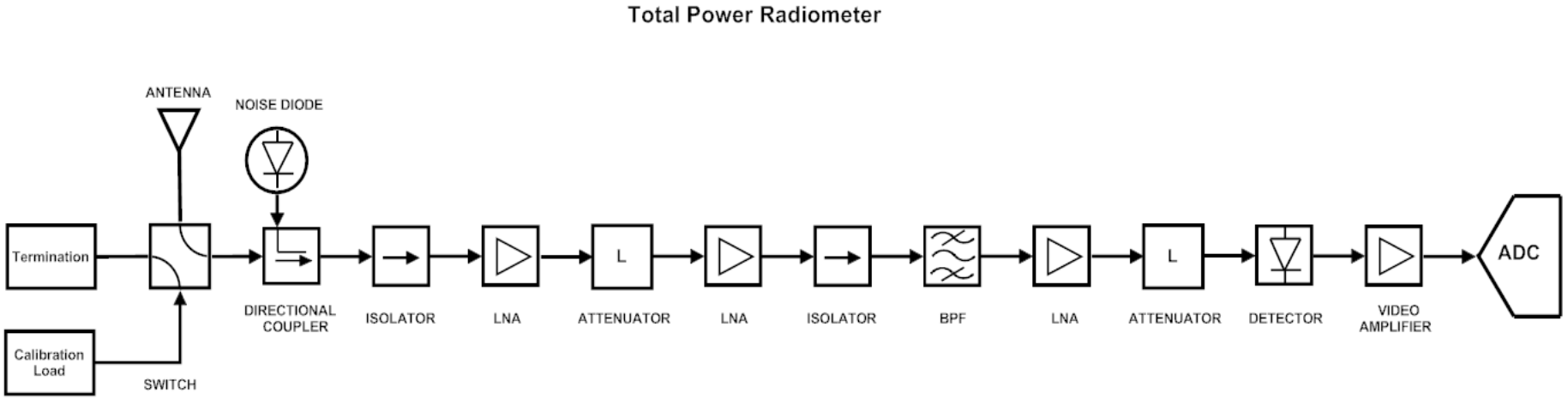

Figure 5-1 Total power radiometer block diagram. Both radiometers use the same configuration. Calibration plane is referred to the directional coupler input.

Table 3 System calculations for Ka-band (36,5GHz) radiometer

Radiometer Ka-band										
[dB]	Switch	Coupler	Isolator	LNA1	ATT	LNA2	Isolator	BPF	LNA3	ATT
NF	0,4	0,4	0,4	2,8	3,0	2,8	0,4	2,0	2,8	3,0
Gain	-0,4	-0,4	-0,4	21,0	-3,0	21,0	-0,4	-2,0	21,0	-3,0
NF Cascade	0,4	0,8	1,2	4,0	4,0	4,1	4,1	4,1	4,1	**4,1**
Gain Cascade	-0,4	-0,8	-1,2	19,8	16,8	37,8	37,4	35,4	56,4	**53,4**
[dBm]										
Output Power	-71,9	-71,9	-71,9	-48,1	-51,1	-30,1	-30,5	-48,0	-27,0	**-30,0**

Table 4 System calculations for W-band (89GHz) radiometer

Radiometer W-band										
[dB]	Switch	Coupler	Isolator	LNA1	ATT	LNA2	Isolator	BPF	LNA3	ATT
NF	0,8	0,8	0,8	4,0	3,0	4,0	0,8	2,0	4,0	3,0
Gain	-0,8	-0,8	-0,8	15,0	-3,0	15,0	-0,8	-2,0	15,0	-3,0
NF Cascade	0,8	1,6	2,4	6,4	6,5	6,6	6,6	6,6	6,6	**6,6**
Gain Cascade	-0,8	-1,6	-2,4	12,6	9,6	24,6	23,8	21,8	36,8	**33,8**
[dBm]										
Output Power	-68,0	-68,0	-68,0	-49,0	-51,9	-36,7	-37,5	-49,5	-34,5	**-37,5**

Commonly the radiometer noise figure is presented in terms of equivalent noise temperature. The conversion is made by

$$T_e = (10^{NF_{dB}/10} - 1)T_0 \tag{5-5}$$

where T_0 = 290K. Table below summarizes the calculated performances for both receivers.

Table 5 Performance summary for both receivers

Frequency [GHz]	NF [dB]	T_e [K]	Gain [dB]
36,5	4,05	447,1	53,40
89	6,63	1043,7	33,80

5.4 Linearity

LNAs exhibit much larger gain bandwidths than the nominal radiometer bandwidth and the effect of the LNA compression with larger bandwidth has to be analyzed. Table 6 and Table 7 show the calculated output power levels of the LNAs. In the calculations the whole receiver chain is used and $290K$ load at the input is assumed. Crest factor is the peak to rms voltage ratio of a signal. For Gaussian distributed noise, 4 is usually used. Crest factor can be converted to decibels with $CF_{dB} = 20\log\ CF_{linear}$. This results to 12dB for the used factor of 4. Using this margin ensures that peak values have negligible effect on measurement. Case 1 shown in Table 6 and Table 7 does not include the BPF and it would be placed after the last LNA. 16GHz and 40GHz are used as effective LNA gain bandwidths for 36,5GHz and 89GHz radiometers respectively. It can be seen that the rms power levels at the LNAs are well below the saturation points. However, when the crest factor is added we only get about 5dB and 9dB margins at the third LNAs in Ka- and W-band respectively. This is considered to be too low especially if other spurious signals are within the range of wideband gain of LNAs. Also this does not give freedom to adjust more gain from LNAs if needed. This is the reason why the band pass filter is located before the last LNA as shown in case 2 which is the case for this design. The margin is now increased to 23dB and 21dB and no LNA saturation is expected.

Table 6 Amplifier saturation analysis for Ka-band radiometer

Radiometer Ka-band							
Case 1	Ant	LNA1	ATT	LNA2	ISO	LNA3	
rms [dBm]	-71,93	-48,13	-51,12	-30,08	-30,48	-9,48	
peak [dBm]	-53,93	-30,13	-33,12	-12,08	-12,48	8,52	
Case 2	Ant	LNA1	ATT	LNA2	ISO	BPF	LNA3
rms [dBm]	-71,93	-48,13	-51,12	-30,08	-30,48	-47,99	-26,99
peak [dBm]	-53,93	-30,13	-33,12	-12,08	-12,48	-29,99	-8,99

Table 7 Amplifier saturation analysis for W-band radiometer

Radiometer W-band							
Case 1	Ant	LNA1	ATT	LNA2	ISO	LNA3	
rms [dBm]	-67,95	-48,95	-51,90	-36,74	-37,54	-22,54	
peak [dBm]	-49,95	-30,95	-33,90	-18,74	-19,54	-4,54	
Case 2	Ant	LNA1	ATT	LNA2	ISO	BPF	LNA3
rms [dBm]	-67,95	-48,95	-51,90	-36,74	-37,54	-49,54	-34,53
peak [dBm]	-49,95	-30,95	-33,90	-18,74	-19,54	-31,54	-16,53

In this configuration we have some wideband noise at the detector amplified in the last LNA. It is important that the detected signal is dominated by the filtered noise and the measured signals are not contaminated by the last LNA wideband noise. This can be analyzed by calculating the wideband power of the LNAs. These values are compared with the nominal band limited noise power used in the system calculations. We can see from the Table 8 that the wideband excess noise is well below the in-band signal levels and therefore its effect to the measurement is negligible. Calculations use the estimated minimum $100K$ signal level at the input. This situation presents the worst case where weakest signals are measured. Wideband noise power (WNP) is significantly lower than the filtered noise power (FNP) and adds the total power level at the detector 0,09dB and 0,35dB for the Ka-band and W-band radiometers respectively and hence, the WNP contributions in the measured power levels are insignificant.

Table 8 Last LNA wideband noise analysis for both receivers

	LNA BW [GHz]	BPF [GHz]	WNP [dBm]	FNP [dBm]	WNP+FNP [dBm]	Added WNP [dB]
Ka-band	16	0,45	-48,13	-31,29	-31,20	0,09
W-band	40	4,00	-48,95	-38,20	-37,85	0,35

5.5 Mechanical design

Radiometer box consists of two radiometers (Ka-band and W-band), bias circuitry for the active parts of the radiometer and temperature stabilization electronics. In the mechanical design, size and weight requirements were in high priority since the radiometers will be mounted on the antenna feed. Small size requires integration of parts to one mechanical block. Effective thermal design with small size and weight is briefly discussed. Finally the cryogenic load design for calibration is presented.

5.5.1 Component mechanics

To use MMICs (Monolithic Microwave Integrated Circuit) within a waveguide housing a waveguide to microstrip transitions are required. MMICs are connected to the transitions by wire bonding. When these active chips are enclosed in a metal housing, cavity resonances may emerge. These microwave cavities have certain resonant frequencies where oscillations can occur. Standing waves inside the cavity makes the impedance fluctuate wildly introducing instability in the active devices. To reduce the reflections inside the cavities an absorber material was used. Microwave absorbers are effective in damping the resonances. Absorbers have high values of permittivity and permeability in addition to high loss factor. These properties give the absorber the ability to store the electric and magnetic energy and convert it to heat. To effectively dampen the dominant resonating mode the absorber is placed in the middle of the cavity (in propagating direction) where the field maximum is. The absorber slab is made long enough to cover the whole distance from one transition to the other.[21]

A split block technique was used throughout the radiometer block designs. All blocks were yellow chromated to avoid oxidation of aluminum which was the material used in all blocks. Only few blocks are used to mount the radiometers to the base plate. Blocks left in between are only connected by the flanges and are above the base plate to help relief mechanical stresses. To reduce the size and weight a certain level of integration is necessary. The first two LNAs are integrated to the same mechanical block with a microstrip attenuator placed in between the amplifiers. Also the diode detector is placed to the same block with the third LNA with an attenuator between the components. Mechanical designs are shown in Figure 5-2 and Figure 5-3. In the front is the waveguide switch which enables the possibility of onsite calibration which is essential for accurate measurements. The two-channel waveguide switch is equipped with a DC-motor that is

used to switch between positions. After the switch there is a waveguide twist that changes the polarization. This is added to connect the switch and the following directional coupler with orthogonal polarizations. Directional coupler is used to inject noise to the receiver path. Noise block is mounted in one of the ports of the directional coupler from which the power is coupled to the signal path. The unused port is terminated with a matched load. Waveguide isolators are used at both sides of the 2xLNA block. For the isolator a commercial product was chosen. The next component is the band pass filter that determines the system pre detection bandwidth.

All components, especially active, exhibit some temperature dependence. As the radiometer temperature fluctuates the response of the radiometer fluctuate with it. This leads to strict temperature control requirements. Drifts in thermal gradients are unavoidable, but they can be suppressed to such small levels that during the calibration interval the changes are negligible. The calibration procedure assumes full knowledge of calibration load temperatures, from which the radiometer response can be deducted. The internal matched load is known by accurate measurements of its physical temperature. However the noise diode brightness temperature is obtained by factory calibration and the changes in its brightness temperature cannot be measured during operation. The used commercial PID-controller used for thermal stabilization has thermal fluctuations within $0{,}1C$. Noise diode temperature fluctuation due to this small thermal instability is believed to be insignificant [14]. However, the noise diode thermal sensitivity should be measured before final conclusion can be given. This can be done in factory calibration mode where noise diode temperature is determined.

5.5.2 Radiometer box

The radiometer box is thermally insulated. Peltier element is mounted directly to a heat sink with high thermal conductivity. Peltier is mounted close to the 2xLNA blocks of the radiometers which are the most likely source of low frequency fluctuations induced by thermal fluctuations. One controlled thermal path is allowed through a peltier element. All other sides of the mechanics are thermally insulated with high performance insulating material. Small exception results from the inevitable fact that some interfaces are needed for making the actual measurements, namely the waveguide interfaces and data and power supply wires to the box. Waveguide interfaces are made from low thermal conductivity material with small cross sectional area to increase the thermal resistance. Stainless steel with $0{,}25mm$ wall thickness was chosen. All components in-

cluding bias electronics and AD-converter are inside the temperature stabilized box. The temperature stabilizing electronics is placed outside the box. A commercial controller is used where a PID (Proportional-Integrate-Derivate) controller drives the Peltier element. Enough power is needed to overcome external heat changes. Also the control loop time constants need to be considered in the mechanical design. Even if the radiometer is fully insulated with low thermal conductivity insulation material it has finite thermal resistivity i.e. external temperature changes affect the inside temperature of the radiometer. These changes should be kept low to ease the stability issues of the control loop which leads to the demand for very high thermal resistance and thermal capacity of the box. The control has to be fast enough that it can accurately follow the external heat and limit the temperature drift to $0{,}1C$ or less. The sensing temperature sensor needs to be mounted in the vicinity of the Peltier element to keep the thermal time constant small between the heating element and the sensor.

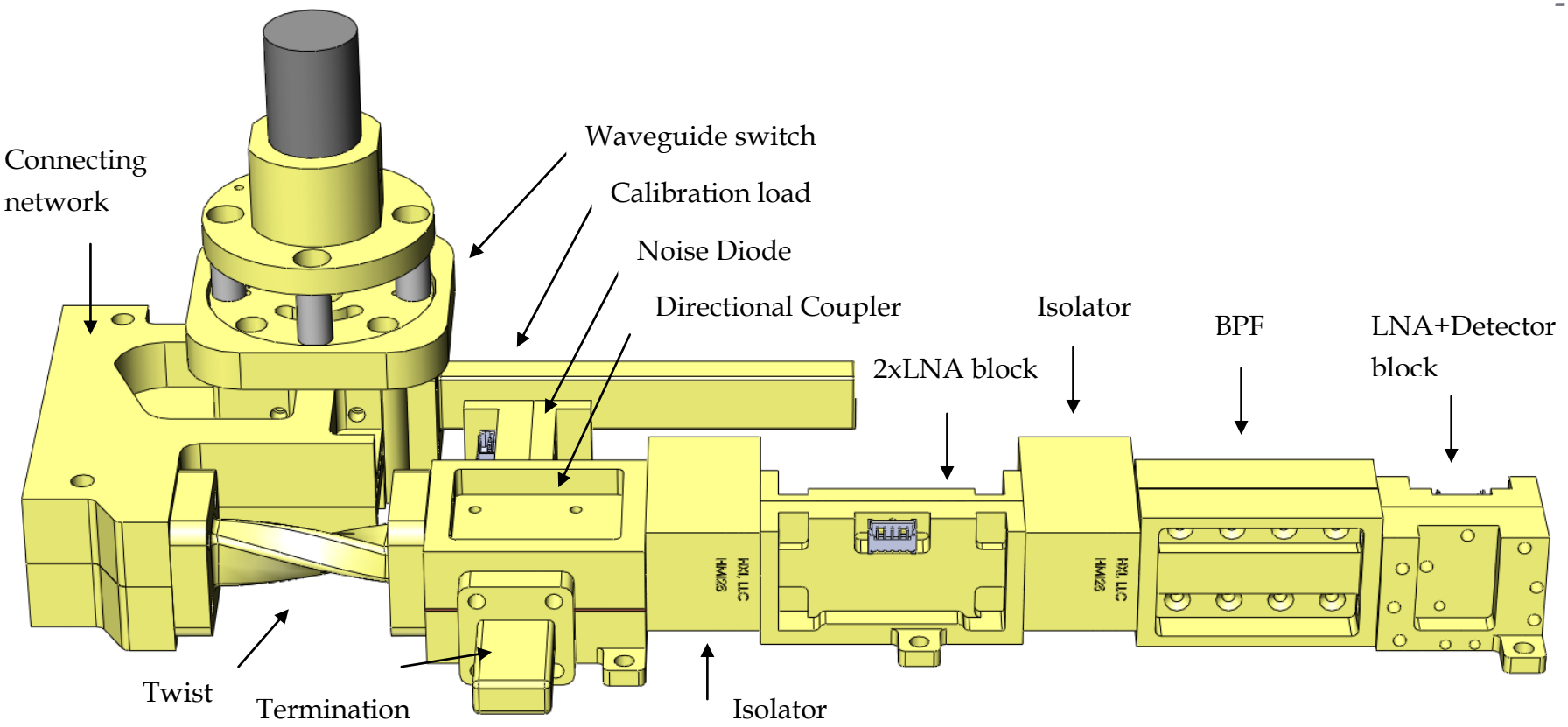

Figure 5-2 Mechanical drawing of the Ka-band radiometer. One port of the waveguide switch (not seen in the picture) is terminated with a matched load. The overall size is 253x117 [mm] and it weighs 510g including the connecting network. The connecting network has standard WR28 flange as a connecting interface. Biases and video signal are connected with shielded ribbon cables.

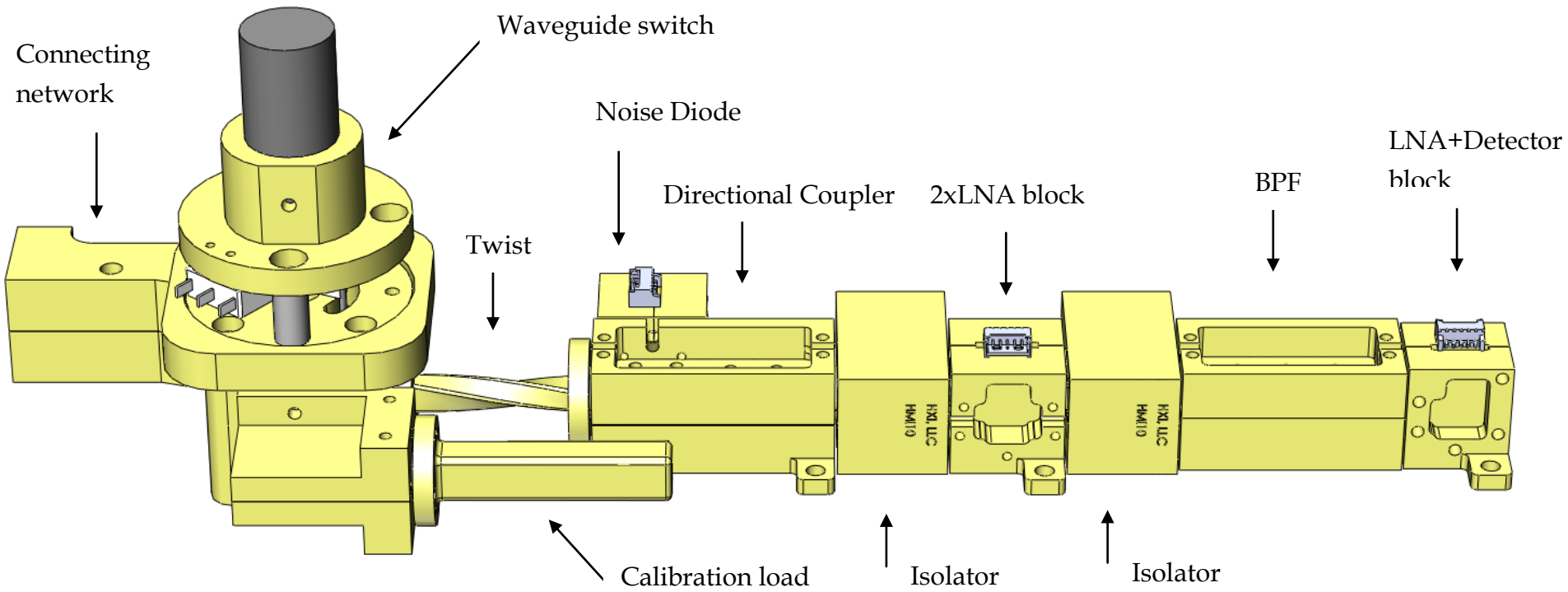

Figure 5-3 Mechanical drawing of the W-band radiometer. One port of the waveguide switch (not seen in the picture) is terminated with a matched load. The overall size is 263x77 [mm] and it weighs 370g including the connecting network. The connecting network has standard WR10 flange as a connecting interface. Biases and video signal are connected with shielded ribbon cables.

6 CRYOGENIC LOAD

6.1 Construction

Two reference temperatures are needed for the radiometer calibration. The noise diode temperature, used in the field measurements, has to be measured. This is done in factory calibration. The two known reference temperatures used in the factory calibration are a matched load with a measured physical temperature and a cryogenic load.

Cryogenic load can be made by submerging a waveguide load into liquid nitrogen (LN2) as described in [22]. Although this structure can be simplified there are many design considerations that make it impractical. At millimeter wave frequencies the waveguide tube connecting the antenna to the radiometer is the dominating error source. The waveguide losses and the temperature profile along the waveguide have to be known with great accuracy. Heat flow from warm ambient to the cooled load creates uncertainty to the physical temperature of the load. Dry nitrogen would have to be blown in the matched load to prevent air from icing inside the tube. The physical temperature of the absorbing material is also difficult to measure since it is inside a waveguide tube.

More practical approach can be achieved by cooling an absorber material with LN2 and use an antenna connected to the radiometer input to view the cooled absorber. Mechanical drawing of the cryogenic load is shown in Figure 6-1. The reflections of boiling LN2 are difficult to estimate and they change as the nitrogen boils away from the absorbing material. Therefore the antenna is placed beneath the polystyrene box. This is more repeatable and it also provides longer operation time of the load with one filling of nitrogen when the boiling does not affect the brightness temperature of the load. The reflection resulting from air-polystyrene interface is negligible since the polystyrene has a dielectric constant close to unity. The condensation of water on polystyrene surface is eliminated by high volume air flow along the surface. The absorber needs to be placed firmly to the polystyrene box to avoid reflection from polystyrene-LN2 interface and to only have polystyrene-absorber interface. For this reason a metal plate is mounted on top of the absorber to press the absorber tightly against the polystyrene. Metal plate is drilled full of holes to let the LN2 boil away freely. Absorber needs to be porous and soaked in LN2. An impedance tapered flat absorber was chosen with measured return

loss around $30dB$. The same reference load can be used for both receivers by only changing the antenna and the connecting waveguide tube. [23][24]

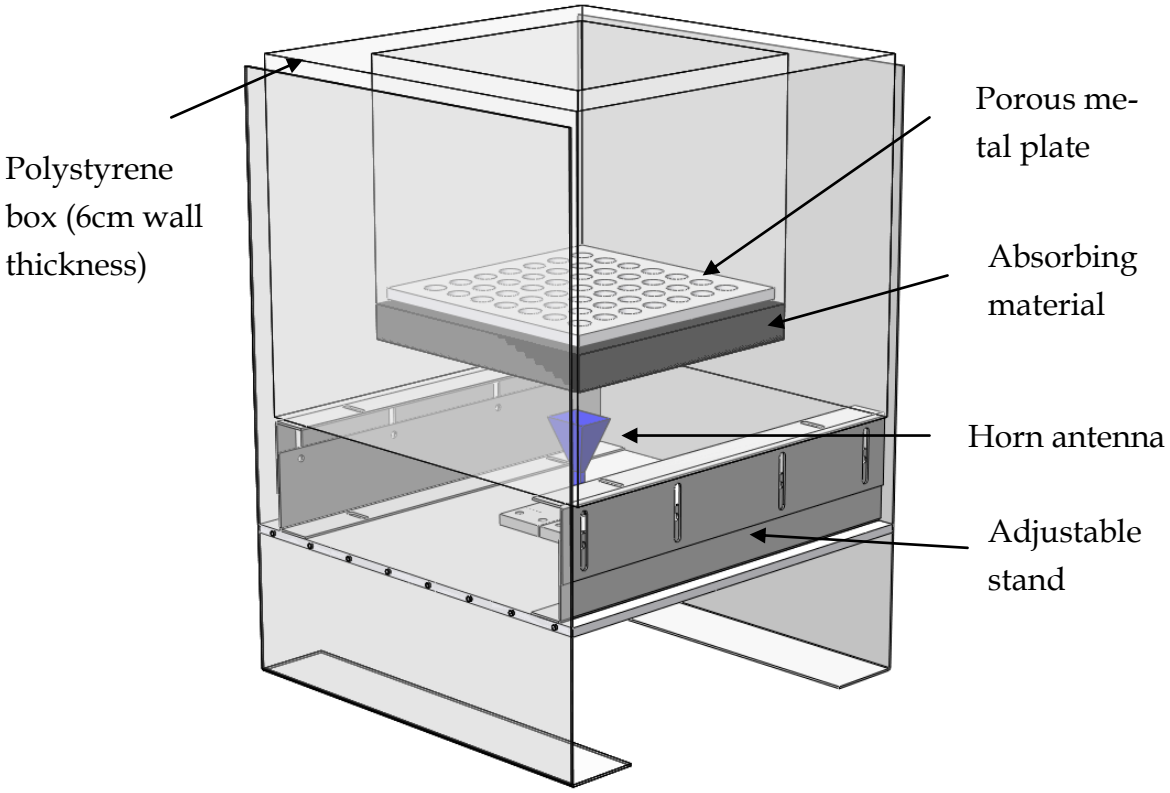

Figure 6-1 Mechanical drawing of the cryogenic load. Waveguide interface is beneath the horn antenna. LN2 is poured into the box and the load is viewed beneath the box. The absorber dimensions are 26x26x5cm^3.

The resulting antenna temperature is close to the LN2 boiling point. The temperature is slightly increased due to antenna side and back lobe contribution, dissipative antenna losses and polystyrene box dielectric losses. These are discussed in the following chapters.

6.2 Polystyrene base contribution

As the antenna views the absorber through a polystyrene box, its losses need to be evaluated. Polystyrene foam dielectric constant and loss tangent evaluation is given in [25].

The dielectric constant of a polystyrene foam is

$$\varepsilon_r = \frac{2}{5}\varepsilon_{r0}^{d/d_0} + \frac{3}{5}\left[1 + \frac{d}{d_0}(\varepsilon_{r0} - 1)\right] \quad (6\text{-}1)$$

where ε_{r0} is the dielectric constant of polystyrene resin and d and d_0 are the densities of polystyrene foam and resin respectively. Polystyrene resin loss tangent is given by an empirical formula

$$tan\delta_0 = 0{,}89 * 10^{-3} + 6.01 * 10^{-6} f \quad (6\text{-}2)$$

where f is given in GHz The imaginary part of the dielectric constant was assumed to scale linearly with density. The real and imaginary part of the permittivity are related by $tan\delta = -\varepsilon''/\varepsilon'$. The dielectric loss was evaluated for the waveguides with eq. (2-22). For TEM mode, the cut off frequency is zero and the equation reduces to

$$\alpha_d = \frac{ktan\delta}{2} = \frac{\pi\sqrt{\varepsilon_r} f tan\delta}{c}\ [Np/m] \quad (6\text{-}3)$$

The values needed to evaluate the polystyrene base loss are given in the table below. With these values, the loss tangent of polystyrene foam can be calculated. This is plugged into eq. (6-3) accompanied with the dielectric constant of the foam obtained from eq. (6-1).

Table 9 Parameters used to evaluate the polystyrene base losses.

Polystyrene resin ε_r	2,54
Polystyrene resin density	1050kg/m^3
Polystyrene foam ε_r	1,035
Polystyrene foam density	27,8kg/m^3

A linear physical temperature gradient at the polystyrene base is assumed from LN2 boiling point to ambient. The brightness temperature seen at the polystyrene base surface is calculated recursively with eq. (6-4) by dividing the base to $N-1$ thin slices of constant physical temperature.

$$T_B^{n+1} = lT_B^n + (1-l)\,T_{base}^{n+1} \tag{6-4}$$

where $T_B^1 = TLN2$, $T_{base}^1 = TLN2\ and\ T_{base}^N = 290K$ and l is the loss factor

In Figure 6-2 the dielectric loss of a polystyrene box base is shown as a function of frequency per unit length on the left. In the right hand side of the figure the brightness temperature increase due to polystyrene dielectric losses are shown.

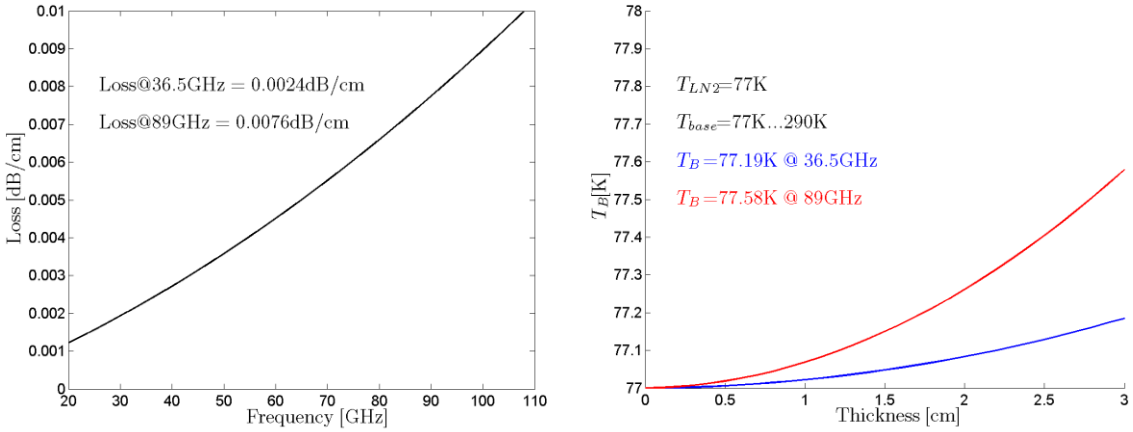

Figure 6-2 Left: Dielectric loss of the polystyrene base as a function of frequency. Right: Brightness temperature of the cryogenic load absorber soaked in LN2 viewed through a polystyrene box as a function of box thickness.

The temperature contributions from the polystyrene base are calculated with three different assumptions to obtain the nominal value with error limits. The minimum contribution is obtained by assuming that the base is completely cooled down to LN2 boiling point. The nominal value is calculated with the assumption of linear physical temperature gradient between the LN2 boiling point and the ambient temperature as shown in Figure 6-2 . This is assumed to be the base temperature after few minutes when the system has stabilized. The maximum temperature contribution is obtained by assuming that the base is fully at the ambient temperature of $290K$. This is believed to be valid only

very short period of time when LN2 poured into the polystyrene box. Base thickness of 3cm is chosen as a compromise for mechanical strength and performance. Results from these calculations are shown in table below.

Table 10 Brightness temperature increase resulting from polystyrene dielectric loss.

	36,5GHz	89GHz
ΔT min	0K	0K
ΔT nominal	0,19K	0,58K
ΔT max	0,36K	1,12K

6.3 Apparent antenna temperature

The side and back lobe contribution to the cryogenic load brightness temperature is evaluated by weighing the load temperature profile with the antenna power pattern. The weighing is done over 4π steradians presenting the sphere surface. The antenna power pattern $G(\theta,\phi)$ and the cryoload temperature profile $T(\theta,\phi)$ are both functions of spherical angles.

$$T_A = \frac{\int_{4\pi} G(\theta,\phi) * T(\theta,\phi) d\Omega}{\int_{4\pi} G(\theta,\phi) d\Omega} \tag{6-5}$$

The antenna gain power patterns are obtained from HFSS simulations. The temperature pattern depends on the boiling point of LN2, polystyrene losses and the temperature and emissivity of the cavity walls. The cavity walls are coated with copper tape for low emissivity. It is assumed that the absorber emits noise to the cavity walls from where they are reflected before absorbed by the antenna. If no multiple reflections are present, the cavity wall brightness temperature can be calculated with

$$T(\theta,\phi) = e(\theta,\phi)T_0 + (1 - e(\theta,\phi))T_{LN2} \tag{6-6}$$

This is a fair assumption with the designed cavity structure which is wide but low. The emissivity of polished copper is $0{,}02 \ldots 0{,}05$. Figure 6-3 illustrates the calculation procedure described by eq. (6-5). The figure shows the E-plane power gain pattern for Ka-band horn antenna with the respective load temperature profile.

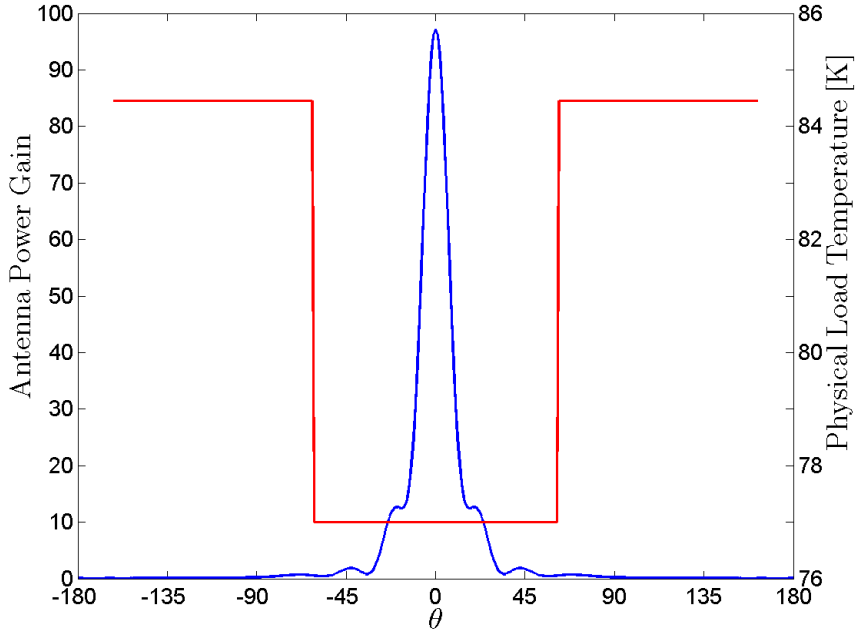

Figure 6-3 Illustration of cryogenic load brightness temperature profile is weighted by Ka-band pyramidal horn antenna E-plane power pattern.

The antennas are assembled close to the absorber to ensure that the absorber fully covers the antenna aperture. This leads to the antennas being in the near-field. Antenna patterns have been simulated in near-field with sphere from flare origin at 90mm, and 70mm radius for the WR28 and WR10 antennas respectively. These resemble the distance of the absorber in the final cryogenic load assembly. Far-field simulations are also carried out for both antennas. The near-field simulations generally give lower antenna temperature than the far-field simulations.

Three different simulations are made for both frequencies. From these, a nominal brightness temperature increase from LN2 boiling point with conservative error margins is obtained. The minimum value is calculated with near-field pattern and with emissivity 0,02 for all cavity surfaces. All cavity surfaces are assumed to have one reflection from the cryogenic absorber resulting cavity wall temperature of $81{,}26K$. The maximum value is obtained with far-field simulation with cavity emissivity of 0,05. This is the emissivity for tarnished copper tape. The copper surfaces are polished and kept clean and hence this value presents a conservative estimate. Two reflections are assumed between cavity wall and cryogenic absorber resulting in cavity wall temperature

of $97{,}77K$ which is a conservative estimate. This is obtained using eq.(6-6) recursively two times. The nominal value is calculated with emissivity of $0{,}03$ and assuming one reflection resulting in $83{,}39K$ for cavity wall temperature. Simulated near-field antenna pattern is used. In all cases cavity wall brightness temperatures are assumed to be constant. The temperatures used to calculate the temperature profile are $T0 = 290K$ and $T_{LN2} = 77K$. The distance from antenna aperture and absorber was $5cm$ and absorber area was $25{,}8cm\ x\ 25{,}8cm$.

In the table below, the results of the cryogenic load temperatures profiles weighted by simulated antenna patterns are summarized.

Table 11 Brightness temperature increase resulting from load brightness temperature profile weighted with antenna power pattern. The increase is a result of antenna side and back lobes that view a brightness temperature above LN2 boiling point.

	36,5GHz	89GHz
ΔT min	0,04K	0,07K
ΔT nominal	0,06K	0,10K
ΔT max	0,45K	0,65K

6.4 Antenna efficiency

Antennas used in cryogenic load are standard gain horn antennas. The power attenuation of a rectangular horn antenna is calculated with

$$\alpha = e^{2K \int \alpha_c dz} \tag{6-7}$$

where K is a factor for surface roughness and α_c is a conductor loss described in chapter 2.3. The waveguide tube after the antenna, used to connect the antenna to the radiometer, ensures that no other modes can propagate and no power is transferred from other modes through the antenna. This simplifies the analysis, since only $TE10$ mode must be analyzed and other modes can be safely ignored. The cutoff frequency given by eq. (2-18) simplifies to $f_c = c/2a$. The attenuation for a waveguide with changing aperture dimensions can be calculated with (2-23) and (2-24). The total attenuation is obtained by integrating the antenna losses over its length z. The K in the exponent of eq. (6-7) is

a surface roughness factor, that is obtained by measurement. A similar waveguide tube from which the antennas are manufactured are measured and compared to the ideal value with the same conductivity. Then K is adjusted accordingly and used throughout the profile.[5] Especially for higher frequencies, the surface roughness is believed to be the dominant factor deviating the tube losses from ideal. Even if other factors contribute, they are included since the K factors are obtained by measurements. The used antenna dimensions are given in Table 12. The antenna loss profiles are shown in Figure 6-4.

Table 12 Dimensions for antennas used in the cryogenic load.

	Ka-band@36,5GHz [mm]	W-band@89GHz [mm]
antenna length	71,2	24,9
flare length	50,9	24,9
waveguide width a	7,112	2,54
waveguide height b	3,556	1,27
aperture width	43,2	8,30
aperture height	34,6	5,80

According to [5] the antenna loss equals antenna efficiency, $\alpha = \eta_l$. The final noise temperature at the antenna terminal can be calculated with

$$T_G = \eta_l T_A + (1 - \eta_l)\, T_0 \qquad (6\text{-}8)$$

The error sources used in the analysis are: the accuracy of the measurement equipment, uncertainty in mechanical dimensions and uncertainty in the conductivity and surface roughness factor. Uncertainty in horn antenna mechanical dimensions is less than $0{,}1mm$. The error in conductivity is assumed to be $\pm 20\%$ which is used throughout the antenna profile. Measurement accuracy of the used VNAs is at worst $0{,}2dB$ [26]. This is a conservative $|S21|$ for $70GHz$. This is used for both frequencies. Minimum value is obtained with highest conductivity value and largest mechanical dimensions and by assuming no loss flare section. Maximum value is obtained with lowest conductivity, smallest mechanical dimensions and by assuming the maximum VNA error in the surface roughness factor. Nominal value is calculated with nominal parameter values.

Assuming $T0 = 290K$ and $T_A = 77K$, the antenna loss contribution is calculated and presented in Table 13.

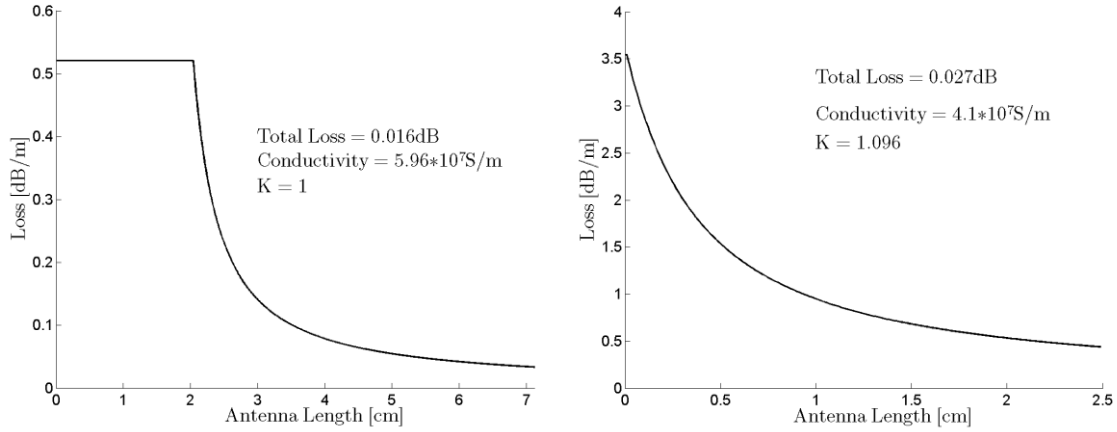

Figure 6-4 Standard gain horn antenna attenuation profiles. Total loss is obtained by integrating over the loss profile. Left: WR28 antenna attenuation at 36,5GHz. Antenna material is copper Right: WR10 antenna attenuation at 89GHz. Antenna surface is flashed with gold.

Table 13 Brightness temperature increase of the cryogenic load due to dissipative antenna losses.

	36,5GHz	89GHz
ΔT min	0,46K	1,08K
ΔT nominal	0,77K	1,31K
ΔT max	0,93K	1,64K

6.5 Error analysis

The presented analysis accounting for dielectric losses of the polystyrene base, antenna side and back lobe contribution and antenna efficiency was analyzed. In all simulations the used temperatures were $77K$ for LN2 and $290K$ for the ambient. The LN2 boiling point is dependent on atmospheric pressure and it should be corrected accordingly. Also the ambient temperature should be measured. When the side and back lobe contributions are calculated the used brightness temperature should be corrected with the increase from polystyrene loss. The brightness temperature resulting from this should finally be plugged into the antenna efficiency simulation to get the final brightness tem-

perature. In addition all thermodynamic temperatures should be changed to their brightness temperatures using eq.(2-9). The final calculated brightness temperatures of the load and the error analysis without these corrections are presented in Table 14 and Table 15.

Table 14 Calculated cryogenic load brightness temperatures.

	36,5GHz	89GHZ
brightness temperature	78,02K	78,99K

Table 15 Summary of error sources and total error of the cryogenic load brightness temperature (root square sum of individual error sources).

	36,5GHz		89GHz	
uncertainty in polystyrene base	+0,17	-0,19K	+0,54K	-0,58K
uncertainty in antenna temperature	+0,39K	-0,02K	+0,55K	-0,03K
uncertainty in antenna efficiency	+0,16K	-0,31K	+0,33K	-0,23K
total uncertainty	+0,45K	-0,36K	+0,84K	-0,62K

7 MICROWAVE COMPONENTS

The passive microwave components designed for the radiometers are presented below. The microwave to microstrip transition for the W-band radiometer had been designed for previous projects at DA-Design Ltd. The waveguide switches were redesigned from existing designs. The isolators were commercial products. These are not included in this section.

7.1 Directional couplers

Directional couplers are four port devices. If power is incident in port 1, then port 2 is the through port as most of the power is present at this port. Port 3 is characterized by coupling as designed amount of power is coupled to it. Port 4 is characterized by the isolation which in an ideal case would be infinite i.e. no power would be present at this port. Another figure of merit is the directivity which is the ratio of the power delivered to the isolated port and to the coupled port. Even though isolation and directivity would be infinite with ideal coupler, it is not the case in practical realizations. The previous quantities can be defined as:

$$Coupling = C = 10log\frac{P_1}{P_3} \tag{7-1}$$

$$Directivity = D = 10log\frac{P_3}{P_4} \tag{7-2}$$

$$Isolation = I = 10log\frac{P_1}{P_4} \tag{7-3}$$

where powers $P_1 \ldots P_4$ are the powers at the ports. Waveguide directional couplers are formed by stacking two waveguides so that they will have one common broad wall. In this wall openings are made, normally these are holes, crosses or slots from which the power can couple. It is common practice to place these openings $\lambda_g/4$ from each other. This way the coupled power from each opening will be in phase for forward propagating waves and out-of phase for backward propagating waves.

For the Ka-band radiometer Moreno cross coupler is chosen for its compact size and for W-band multihole coupler is chosen for better performance where the size is not an issue.

7.1.1 Moreno coupler

The Moreno coupler consists of two guides at right angles that share a common broad wall shown in Figure 7-1. Two apertures are shared by the guides. Typically round-ended crosses are placed symmetrically around the center of the square the two guides form. Crosses may be aligned with same direction as the guides or rotated 45° as in Figure 7-1. This has no effect on performance[27]. Analytic results for magnetic and electric polarizabilities, α_m and α_e, for small apertures has only been solved for circular and elliptic structures. However many different types of apertures have been measured and results for crossed round ended slots are shown in Table 16. Moreno coupler relies on magnetic coupling for its power transfer, but some unwanted electric field coupling cannot be avoided. This is normally much weaker than the magnetic coupling and the effect to the coupled port is negligible. However electric field also couples to the opposite isolated port which limits the directivity. The use of crosses instead of holes reduces the electric coupling and hence improves the directivity. The amplitude of the magnetically coupled wave is given by

$$c_m = -\frac{\pi\alpha_m}{a^2 b}\sin\left(\frac{2\pi d}{a}\right) \tag{7-4}$$

It is independent of frequency. Dimensions a and b are the waveguide width and height respectively. Spacing of the aperture d is shown in Figure 7-1. Coupling is most efficient at a frequency where quarter of a wavelength is $(a - 2d)$. Maximum coupling efficiency happens when $d = a/4$. Good matching is ensured with symmetrical placing of the crosses. With symmetrical configuration the operating frequency is $\sqrt{2}$ times the cutoff frequency. Using the maximum coupling efficiency eq. (7-4) reduces to

$$|c_m| = \frac{\pi\alpha_m}{a^2 b} \tag{7-5}$$

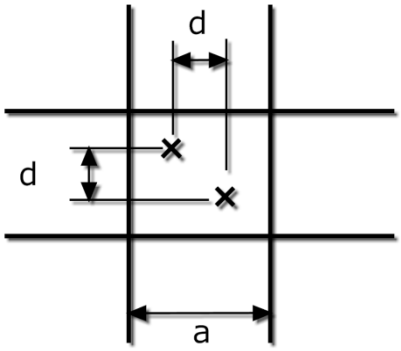

Figure 7-1 Geometry of two aperture cross coupler

The magnetic coupling does not contribute any power to the isolated port and this type of coupling is intrinsically directional. When electric coupling is considered the coupled power at an aperture will propagate forward and backward. For a narrow slot the magnetic coupling dominates, and has negligible effect on coupling, but the effects lead to a finite directivity. The magnetic coupling at the second aperture has the opposite sign. This implies that coupled power from both apertures add when the difference in path length is half wavelength. The coupled wave amplitude after the second aperture is given as

$$|c_m| = \frac{2\pi\alpha_m}{a^2 b}\sin\left(\frac{2\pi d}{a}\right)\sin[\beta(a-2d)] \tag{7-6}$$

No wave is send to the isolated port since phases add out-off-phase. For the electric coupling, where the signs of the coupled waves are the same, the cancellation happens at the coupled arm due to the half wavelength path difference. For the isolated port the wavelengths are the same and they add in phase given by

$$|i_e| = \frac{2\pi|\alpha_e|}{a^2 b} \tag{7-7}$$

Therefore the theoretical directivity at the mid band is

$$D = 20log\left|\frac{\alpha_m}{\alpha_e}\right|\text{dB} \tag{7-8}$$

where α_m and α_e are magnetic and electric polarizabilities respectively. These are given for round ended crosses in table below.

Table 16 Magnetic and electric polarizabilities for round ended crosses. Width of the cross is w and the length is l. [27]

Slot Aspect Ratio w/l	Normalized polarizabilities for crossed round ended slots	
	$\frac{\alpha_m}{l^3}$	$\frac{\alpha_e}{l^3}$
0,10	0,0611	0,0039
0,15	0,0728	0,0085
0,20	0,0832	0,0144
0,25	0,093	0,0217
0,30	0,1030	0,0292
0,35	0,1093	0,0373

For a finite wall thickness the attenuation effect for electric field is much greater than for magnetic field. When the wall thickness is not negligibly thin the coupling is weakened. When the thickness is increased the attenuation approaches that of cut off waveguide having cross section of the aperture. When the thickness is increased higher order modes are attenuated the most. The magnetic field primarily couples through $TE10$ mode and electric field through $TM11$ mode. When the thickness is increased the attenuation impacts more to the electric coupling because $TM11$ is further below its cutoff that TE10. This implies that increasing thickness weakens the coupling, but also gives better directivity. The attenuation effect of finite thickness for magnetic coupling can be estimated to be

$$A_m = 17{,}37\pi t\sqrt{\frac{1}{(2l)^2} - \frac{1}{\lambda^2}}\ dB \tag{7-9}$$

Manufacturing imposes some limits that determine the thickness of the aperture $t = 0{,}5mm$ and width of the aperture $w = 0{,}5mm$. From the presented theory we can calculate the coupling coefficient when slot width and length are decided. This normalized data can be curve fitted and given as

$$C = -4{,}098\ln\left(\frac{w}{l}\right) + 11{,}41\ dB \tag{7-10}$$

This has to be adjusted by attenuation given by eq. (7-9). Directivity can be calculated with eq. (7-8) from the measured coefficients by interpolation. The calculated values with length $l = 3{,}5mm$ can be found in Table 17. HFSS simulations were done to veri-

fy obtained results. When the attenuation is included the theoretical value and the simulated value are in good agreement. From simulations it can be seen that the directivity is better than the theoretical value. This is due to the discussed effect of electric coupling attenuating more substantially than the magnetic with finite aperture thickness. In order to further improve the directivity, slot width should be decreased and aperture thickness should be increased. When tight coupling is needed there is of course a limit when increasing the cross length is no more possible.

Table 17 Moreno coupler performance compared between calculated, simulated and measured values. Given values are at design frequency, $\sqrt{2}f_c$=29,8GHz.

	Coupling	Isolation	Directivity
Calculated	22,2	41,6	19,4
Simulated	22,4	51,8	29,4
Measured	20,5	45,2	24,7

The measurement shows that the coupled power is more than expected. This can be seen throughout the band. Isolation has some measurement uncertainty at higher isolation values due to the imperfect termination used at the isolated port during the measurement. This being considered, the isolation corresponds well with the simulated values. The calculated values for isolation and directivity were a theoretical minimum and finite aperture thickness improves these values as discussed. The operating and design frequencies, in this case, were different. At $36{,}5GHz$ the simulated coupling and isolation were $18{,}7dB$ and $37{,}2dB$ respectively. Corresponding measured values were $16{,}8dB$ and $39{,}1dB$. As the coupled power is higher than expected, it leads to increased amount of injected noise diode power from the noise diode. This, however, most likely does not impair the radiometer calibration as was discussed in chapter 4.1.3.

From Figure 7-2 we can see that designed coupler has steadily increasing coupling i.e. it is frequency sensitive. At higher frequencies the properties of the coupler deteriorate which can be seen in isolation, return loss and insertion loss. These effects can somewhat be tuned by cross separation, but Moreno cross coupler has only two openings which makes it inherently narrow banded. For better performance multihole coupler could be used in expense of larger size and weight. The return losses are better than $25dB$ throughout the waveguide band excluding a small portion at the highest frequencies of the band. The mechanical construction of the coupler is shown in Figure 7-3.

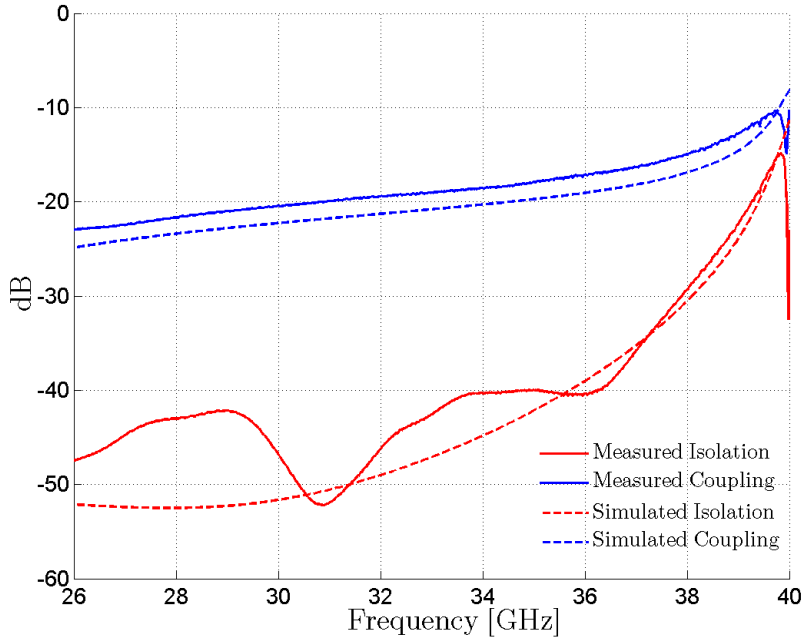

Figure 7-2 Simulated and measured results of the WR28 moreno cross coupler.

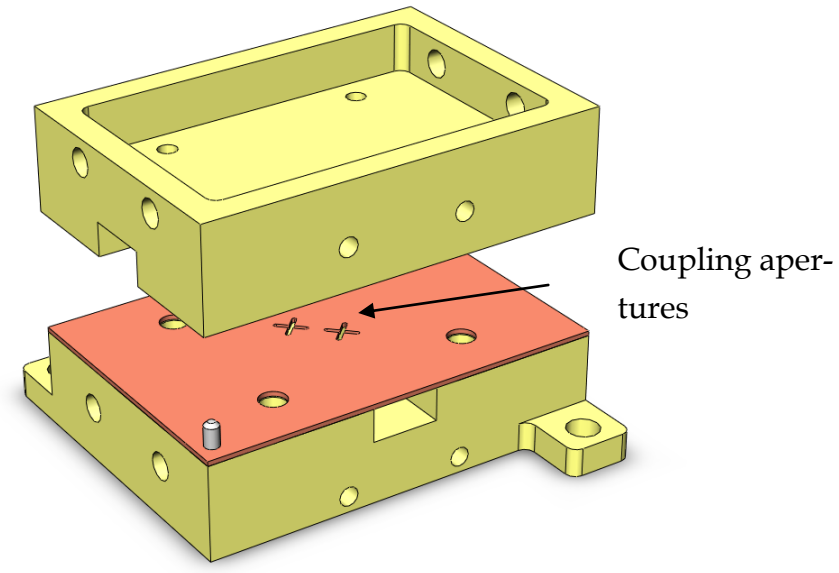

Figure 7-3. Mechanical model of the WR28 moreno coupler. A split block technique with yellow chromated aluminium is used. The brass sheet in the middle is gold plated.

7.1.2 Multihole coupler

This section is based on [7] if not stated otherwise. When only small number of openings is used the coupler will have a narrow bandwidth, at least in directivity. When series of holes are used the bandwidth can be increased. Figure 7-4 shows the basic principle of a multihole coupler. Two parallel waveguides sharing a common broadwall are shown. A longitudinal line of $N+1$ holes, where N is the order of the coupler, are drilled to the common wall of the guides. Spacing of these holes is $\lambda_g/4$ and are offset from the sidewall of the waveguide by distance s. Power enters the port 1 and is transmitted through to port 2 and some of the power is coupled to port 3. At each aperture some power is coupled and will radiate as forward and backward propagating wave component to the upper guide. Wave components going to port 3 will add in phase since they have travelled the same distance. The backward propagating waves add out-off-phase since they have travelled $\lambda_g/2$ further than the wave at the previous aperture and therefore no power is present at port 4. The cancellation is frequency dependent. Coupling is independent of frequency since path lengths for the wave components remain the same.

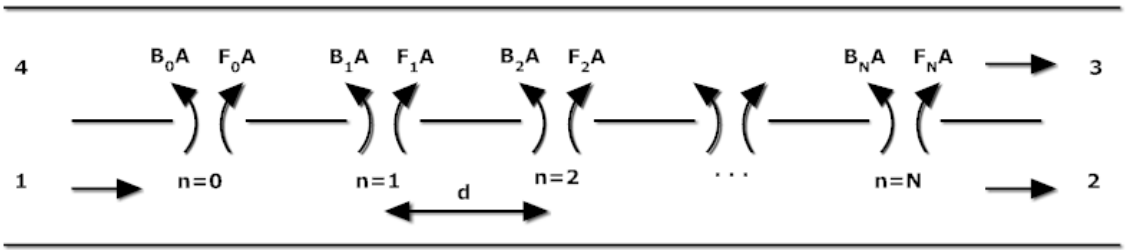

Figure 7-4 Geometry of multihole coupler with N+1 holes and order N.

If another set of holes is drilled symmetrically around the common wall center line the coupling can be increased by $6dB$ i.e. the voltage coupling is doubled [28]. This leaves the directivity unchanged. When tight coupling is desired this is practical since the diameter of the holes can become so large that the holes overlap. Another way to increase coupling is simply to add more holes. The following will show how to calculate the radii of the holes when single set of holes are used with a given coupling and directivity. Presented theory assumes zero hole thickness.

Below the design equations are presented in a simplified and compact form. More detailed discussion is found in [7] and [28]. K_f is a constant for forward propagating cou-

pling coefficient. It is the same for all holes but is a function of frequency given for $s = a/4$ as

$$|K_f| = \frac{2k_0}{3\eta_0 P_{10}}\left[\sin^2\frac{\pi s}{a} - \frac{2\beta^2}{k_0^2}\left(\sin^2\frac{\pi s}{a} + \frac{\pi^2}{\beta^2 a^2}\cos^2\frac{\pi s}{a}\right)\right] \tag{7-11}$$

where P_{10} is given as

$$P_{10} = ab\frac{\beta}{k_0\eta_0} \tag{7-12}$$

where β is the phase constant and η_0 is the free space impedance. There are infinite amount of possible choices for hole radii shown in equation (7-13). Hole radius can be split into $M = N + 1$ parts where W_M^i are Dolph-Tchebycheff weighting coefficients with $i = 1,2,\dots,M$.

$$r_0^3 + r_1^3 + \dots r_N^3 = W_M^1 r_{ref} + W_M^2 r_{ref} + \dots + W_M^M r_{ref}, \tag{7-13}$$

where

$$W_M^i = \frac{M-1}{M-i}\sum_{s=0}^{M}\binom{i-2}{s}\binom{M-i}{s+1}\alpha^{s+1} \tag{7-14}$$

$$\begin{gathered} for\ i \neq 1\ and\ i \neq M, \\ W_M^i = 1, \\ for\ i = 1\ and\ i = M \end{gathered} \tag{7-15}$$

and

$$\alpha = \tanh^2\left[\frac{ln\left(D_{min} + (D_{min}^2 - 1)^{1/2}\right)}{M-1}\right] \tag{7-16}$$

r_{ref} is given as

$$r_{ref} = \frac{K10^{D_{min}/20}}{W_M^1 + W_M^2 + \dots + W_M^M} \tag{7-17}$$

where value for K is given by

$$K = 10^{(-20log|K_f| - D_{min} - C)/20} \tag{7-18}$$

Finally radii of the holes can be calculated

$$r_n = \left(W_M^{n+1} r_{ref}\right)^{1/3} \tag{7-19}$$

Above equations with coupling of $17dB$ and directivity of $40dB$ were used to design eight hole coupler. In order to keep the holes from overlapping with each other and a good return loss at the input, two rows of holes was used and the hole distance from the wall $s = a/4$ was used. Presented theory assumes zero thickness of the holes. Non-zero thickness attenuates the coupled signal and has to be compensated with tighter coupling. The used $0{,}2mm$ hole thickness attenuates the coupling about $6dB$. The extra coupling from the other row increases the coupling by the same amount. Therefore, in this design, no compensation to the initial design values were needed. Table 18 presents the calculated values which required no further optimization.

Table 18 Multihole coupler dimensions [mm]

s	d	r1	r2	r3	r4	r5	r6	r7	r8
0,635	1,104	0,292	0,377	0,443	0,477	0,477	0,443	0,377	0,292

Figure 7-5 shows the measured and simulated results for the multihole coupler. The coupling corresponds well with simulations. The isolation is not as good as given by the simulations. Simulation assumes perfect matching for all ports. The given design has a compact load inside the mechanical block. As the incident wave is first coupled through the apertures and then reflected from the load, directivity and isolation are degraded when high performance load is not used. The average inband coupling is $16{,}9dB$ in the simulation and the measured value is $17{,}2dB$. Return losses at the output ports are around $30dB$. The mechanical construction of the coupler is shown in Figure 7-6.

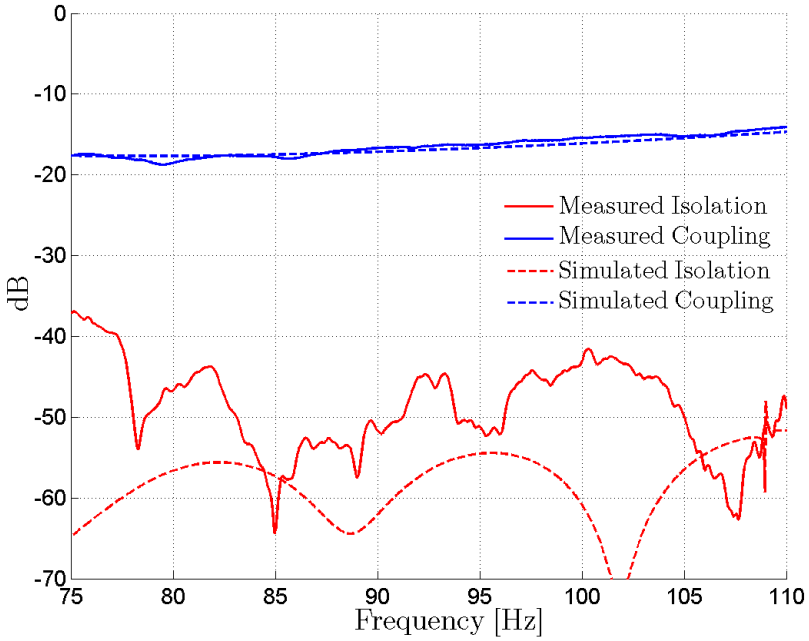

Figure 7-5 Measured and simulated results of the WR10 multihole coupler.

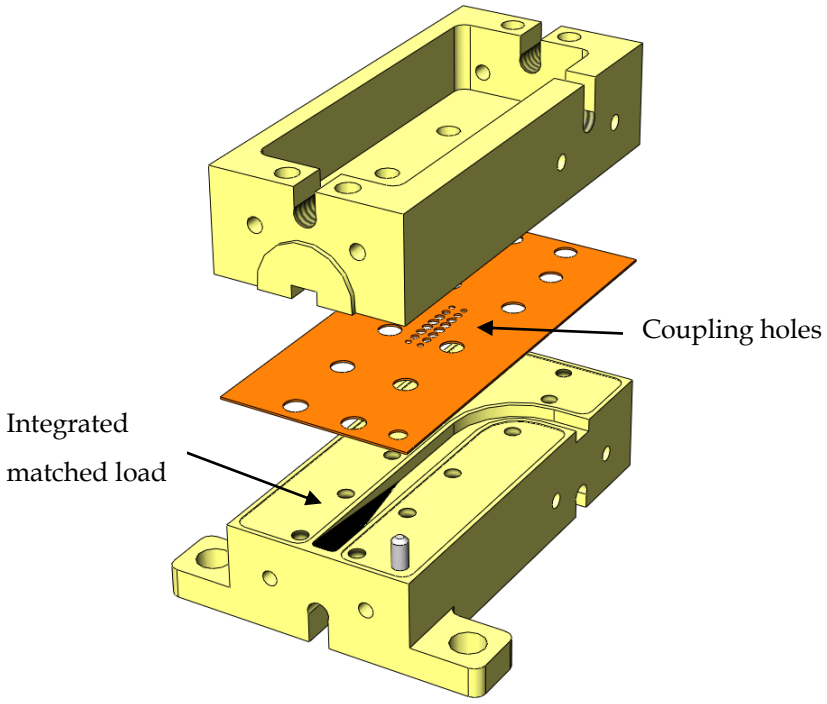

Figure 7-6 Mechanical model of the WR10 multihole coupler. A split block technique with yellow chromated aluminium is used. The brass sheet in the middle is gold plated.

7.2 Waveguide to microstrip transition

If a probe is dimensioned and placed properly, virtually all the energy can be transferred to and from the waveguide to the probe [29]. The selected probe type is particularly suitable for millimeter wave applications since the design tolerances are somewhat loose and it is low loss and broadband. The probe enters the waveguide through an opening on the broad wall of the waveguide. The used mounting configuration is referred as the E-plane probe since the surface of the probe is aligned with the E-plane. The probe section that enters to the waveguide is matched to the microstrip section. A high impedance inductive line is used in series with a quarter-wave impedance transformer to resonate out the capacitive reactance of the probe section. The probe section is tapered to a high impedance inductive line to get a more gradual impedance change and a more frequency insensitive reflection [30].The opening in the broad wall of the waveguide should be small enough to suppress all spurious modes. Dimensions of the design follows [31] where a CAD (computer aided design) based design was adopted and examples were worked out. A scaling factor is provided which enables to tune the designs to other frequencies. Multiplying a given design with $b/2540$ tunes the circuit to a different waveguide band. Dimension b is the width of the waveguide in μm. The reference design has $\varepsilon_r = 2{,}2$ and it does not require the quarter-wave impedance transformer. However, in this design, as $\varepsilon_r = 3{,}38$, the impedance transformer is required. For a starting point the quarter wavelength is used at the design frequency. Rests of the dimensions were scaled from the reference design. These were optimized with HFSS. With optimal values the impedance of the probe varies only little with frequency and results to broadband and tolerance robust design.

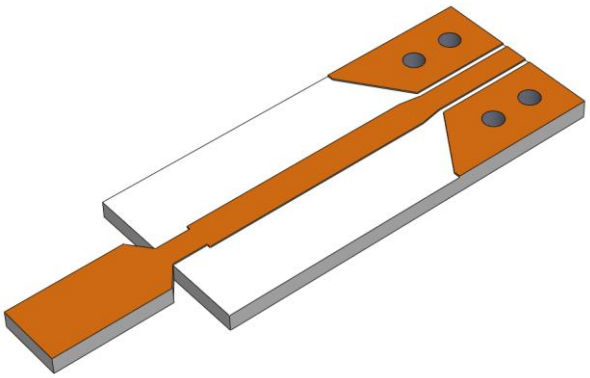

Figure 7-7 Mechanical illustration of theWR28 waveguide to microstrip transition. Base material is Rogers 4003C with $\varepsilon_r = 3{,}38$. Metallization is gold plated copper.

The dielectric constant of the selected material is 3,38. Thickness of the used substrate is $0{,}2mm$. The critical dimensions of the probe are listed below. It also shows the actual dimensions for a typical case which are measured using microscope. When all the metallization is added the final thickness according to measurement is $0{,}33mm$, where $0{,}3mm$ was the expected value.

Table 19 Dimensions of the waveguide to microstrip transition

	Designed	Measured
Probe width	850µm	820µm
Probe length (including taper)	1730µm	1696µm
Probe taper length	210µm	231µm
Inductive line width	300µm	284µm
Inductive line length	450µm	470µm
Quarter-wave transformer length (taper not included)	2970µm	2982µm
Quarter-wave transformer taper	280µm	232µm
Quarter-wave transformer width	400µm	379µm
Width of coplanar line	300µm	282µm
Length of coplanar line	1300µm	1322µm
Spacing of coplanar line	70µm	85µm
Backshort	2200µm	-
Total length	6730µm	6702µm
Total width	2200µm	2196µm
Air gapbetween microstrip line and waveguide metal housing	1mm	-

The probe tip is designed to be at half point from the opposite broad wall and the probe surface at the middle of the broad wall of the waveguide. In HFSS simulation the probe exhibits return loss better than $20dB$. All material losses were less than $0{,}2dB$ over the band. Figure 7-8 presents the simulated values of the probe with the measured physical dimensions. The effects of probe placement were investigated by changing the backshort distance and distance to the opposite broad wall. The design is robust, but still large variation in return losses can be expected with careless placement. The probe length was shorter than expected due to manufacturing tolerances. This poses difficulty in mounting the probe and if not successful this can noticeably decrease the return loss which in turn can increase the insertion loss.

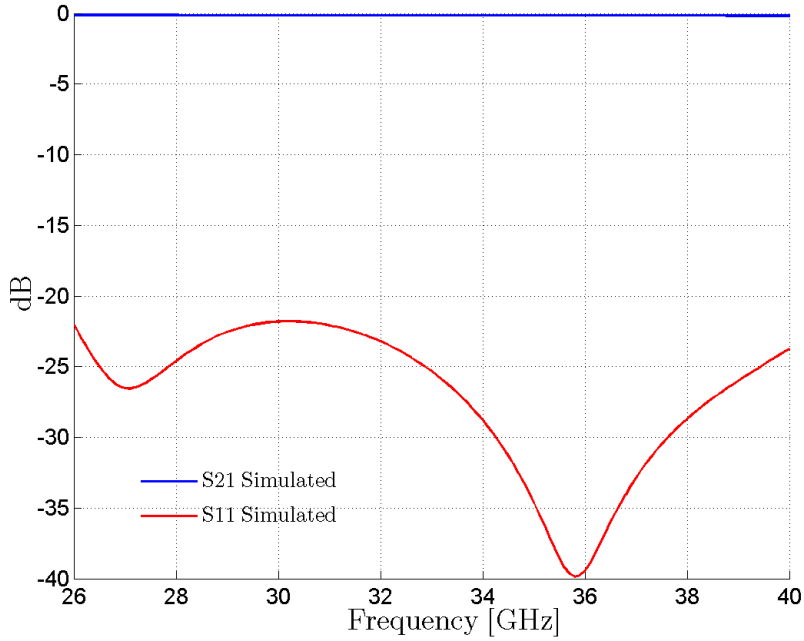

Figure 7-8 Simulated results of the WR28 waveguide to microstrip transition from HFSS.

The transition was measured with back-to-back configuration. Measurement results are shown in Figure 7-9. The tight radius bends in the mechanical block were not included in the simulations but they have been simulated separately. Also the bond wires connecting the probes were not modelled since they can be kept relatively short and the transition thickness is modest and hence the increased inductance is at an acceptable level. Both, however, deteriorate the performance of the transition. The insertion loss within the waveguide band is from $1{,}2dB \ldots 1{,}5dB$ excluding both ends of the waveguide band where the losses are somewhat higher. If bond wire losses and bend mismatch losses are subtracted, it can be evaluated that one transition has losses around $0{,}5dB$. The probe is well suited for broadband operation and the losses are at expected levels.

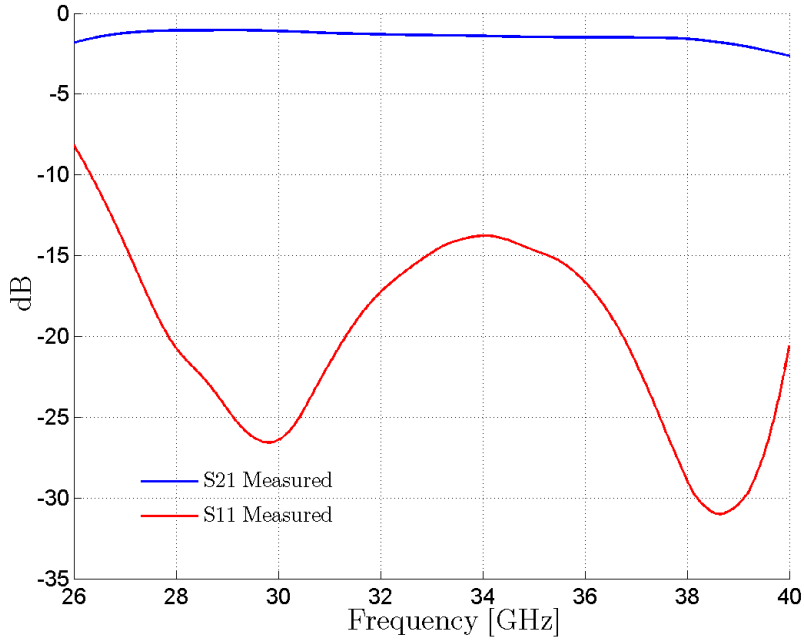

Figure 7-9 Measured results of the back-to-back configuration of the WR28 waveguide to microstrip transition.

7.3 Filters

Filters were designed using insertion loss method and the general procedure begins from filter specifications from which a low pass prototype filter is designed. Then filter is scaled and converted to proper impedance level and to the desired topology. In microwave filters the challenge lies in the implementation, when discrete capacitors and inductors cannot be used. In this section two filter designs are presented. For the Ka-band radiometer a narrow 1,2% bandwidth is required. This is realized by metal insert E-plane filter. For the W-band radiometer 4,5% bandwidth is needed. Due to larger bandwidth requirement H-plane iris filter was chosen. The important specifications are size, roll-off and losses. Phase response does not play an important role since all received signals are noise and only amplitude information is recorded. Increasing the filter order increases the weight and size which is the main reason of keeping the order as small as possible. This also increases the insertion loss and makes it more sensitive to temperature and aging in addition to requiring more complicated manufacturing process.

For W-band H-plane iris filter 5th order filter was chosen. This was the smallest order that met the stop-band attenuation requirements. Tchebyscheff -type filter with $0{,}01dB$ ripple level was chosen as a starting point. For the Ka-band E-plane filter 4th order filter is the smallest order that gives the required stop band attenuation. Butterworth response was chosen since even order filters are not well suited for Tchebyscheff response since it would require an additional matching element.

Table 20 Ka-band filter spesifications

Ka-band	
Center Frequency	36,5GHz
Bandwidth	450MHz
Stop band rejection@36GHz	>15dB
Stop band rejection@37GHz	>15dB
Order	4
Response	Butterworth
Type	E-plane Metal Insert

Table 21 W-band filter spesifications

W-band	
Center Frequency	89GHz
Bandwidth	4GHz
Stop band rejection@86GHz	>15dB
Stop band rejection@92GHz	>15dB
Order	5
Response	Tchebyscheff
Type	H-plane iris

For maximally flat Butterworth response the prototype element values can be calculated with the following equations [32]

$$g_0 = 1 \tag{7-20}$$

$$g_j = 2\sin\left[\frac{(2n-1)\pi}{2n}\right] \quad for\ j = 1,2,\dots,n \tag{7-21}$$

$$g_{n+1} = 1 \quad for\ all\ n \tag{7-22}$$

For Tchebyscheff (equal ripple) insertion loss response the prototype element values can be calculated with following equations [32]

$$\beta = ln\left(\coth\frac{L_{Ar}}{17{,}37}\right) \tag{7-23}$$

$$\gamma = \sinh\left[\frac{\beta}{2n}\right] \tag{7-24}$$

$$a_j = \sin\left[\frac{(2k-1)\pi}{2n}\right] \quad for\ j = 1,2,\dots,n \tag{7-25}$$

$$b_j = \gamma^2 + \sin^2\left(\frac{k\pi}{n}\right) \quad for\ j = 1,2,\dots,n \tag{7-26}$$

$$g_0 = 1 \tag{7-27}$$

$$g_1 = \frac{2a_1}{\gamma} \tag{7-28}$$

$$g_j = \frac{4a_{j-1}a_j}{b_{j-1}g_{j-1}} \tag{7-29}$$

$$for\ j = 2,3,\dots,n$$

$$g_{n+1} = \begin{cases} 1 & for\ n\ odd \\ \coth^2\left(\frac{\beta}{4}\right) & for\ n\ even \end{cases} \tag{7-30}$$

where L_{Ar} is pass-band ripple in decibels.

An equivalent circuit of designed waveguide filters with n dimensions is discussed in [33] and it can be presented as shown in Figure 7-10. The rectangles presents the impedance inverters which can be implemented with shunt and series reactances connected to a transmission line as shown in Figure 7-11. For the presented filters the series reactances can be set to zero and the shunt reactances to be inductive.

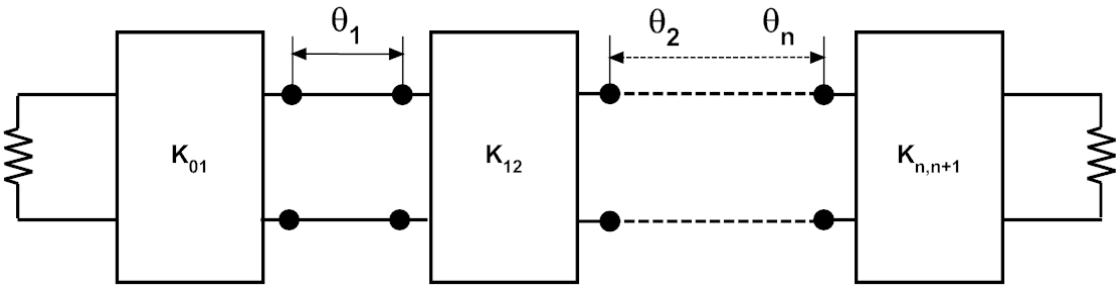

Figure 7-10 Equivalent presentation of bandpass filter with impedance inverters (K inverters) and series resonators.

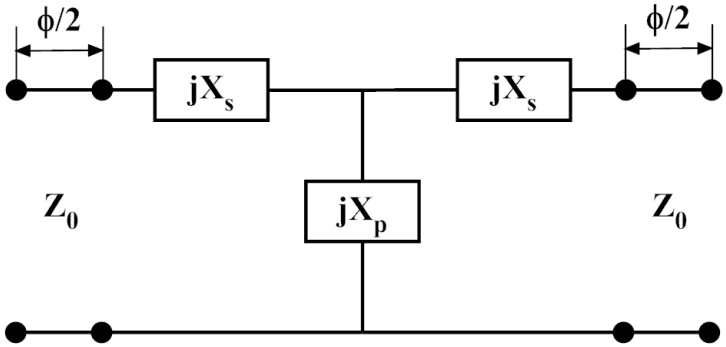

Figure 7-11 Impedance inverter with transmission lines and reactive elements.

From low-pass filter values K-inverter parameters can be calculated

$$\frac{K_{01}}{Z_0} = \sqrt{\frac{\pi\omega_a}{2g_0g_1}} \tag{7-31}$$

$$\frac{K_{j,j+1}}{Z_0} = \frac{\pi\omega_a}{2\sqrt{g_jg_{j+1}}} \quad for\ j = 1,2,\dots,n-1 \tag{7-32}$$

$$\frac{K_{n,n+1}}{Z_0} = \sqrt{\frac{\pi\omega_a}{2g_ng_{n+1}}} \tag{7-33}$$

where

$$\omega_a = \left(\frac{\lambda_{g0}}{\lambda_0}\right)^2 \frac{B}{f_0} \tag{7-34}$$

where λ_{g0} and λ_0 are the guide wavelength and free space wavelength respectively. The element values g_0 and g_n correspond to the generator and to the load respectively and they are 1 for a filter that is matched to the waveguide impedance. If series reactance to zero, then the normalized shunt reactance is

$$\frac{X_{pj}}{Z_0} = \frac{K_{j-1,j}/Z_0}{\left[1 - \left(\frac{K_{j-1,j}}{Z_0}\right)^2\right]} \tag{7-35}$$

Up to this point both filter designs are the same. The final steps of the filters are treated separately.

7.3.1 E-plane filter

Table 22 shows the calculated Butterworth prototype values calculated with equation (7-20)…(7-22). Figure 7-12 shows the metal insert structure where s is the septum length, l is the length of the resonator and b is the waveguide height.

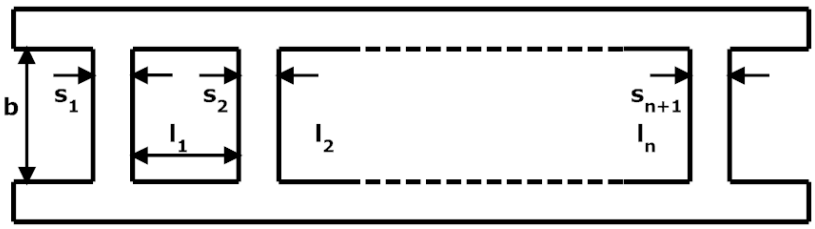

Figure 7-12 Geometry of metal insert filter with N+1 septums with order N.

Septum thickness of $0{,}2mm$ was chosen. K inverter values are calculated with equations (7-31)…(7-34). From these values the corresponding septum lengths are found from design curves of normalized shunt reactance presented in [33]. When the septum lengths that correspond to the normalized shunt reactance are found, the normalized series reactance are obtained in a similar fashion from the curves. Series inductance affects the resonator lengths and has to be included when resonator lengths are evaluat-

ed. After the shunt and series reactance are found, resonator lengths can be calculated with

$$\theta_j = \pi + \frac{1}{2}\left(\Phi_j + \Phi_{j+1}\right) \tag{7-36}$$

$$\Phi_j = -\tan^{-1}\left(\frac{2X_{pj}}{Z_0} + \frac{X_{sj}}{Z_0}\right) - \tan^{-1}\left(\frac{X_{sj}}{Z_0}\right) \tag{7-37}$$

$$l_j = \frac{\theta_j \lambda_{g0}}{2\pi} \tag{7-38}$$

The septum lengths and resonator lengths are presented in Table 23 with the optimized values. Non-primed values are the optimized ones obtained with uWizard.

Table 22 Low pass filter prototype element values for 4th order Butterworth filter

Butterworth low-pass prototype values					
g0	g1	g2	g3	g4	g5
1	0,7654	1,8478	1,8478	0,7654	1

Table 23 Calculated and optimized values of the Ka-band filter. Primed values mark the initial values and non-primed the optimized values.

Calculated and optimized septum window and resonator lengths [mm]					
k	1	2	3	4	5
s'k	1,81	5,67	6,16	5,67	1,81
l'k	2,93	2,93	2,93	2,93	-
s_k	1,806	5,626	6,237	5,626	1,806
l_k	3,397	3,388	3,388	3,397	-

Septum lengths proved to give quite accurate results. Resonator lengths were all too short which pushed the design to higher frequencies. This could be compensated by redesigning with lower center frequency, but since all resonator lengths are almost the

same they can easily be scaled to correct frequency with the aid of computer simulator. Final design was checked with HFSS. Figure 7-13 shows the simulation results from uWizard of the filter with the measured results. The insertion loss at maximum point is better than $1{,}2dB$. The 3dB points are approximately at $36{,}06GHz$ and $36{,}56GHz$ and the center frequency is $36{,}31GHz$. The equivalent noise bandwidth is $500MHz$. Figure 7-14 shows the measured wideband response of the metal insert filter. The power spectral density at diode detector needs to be analyzed to see if there is a significant power at the spurious band which could affect the radiometer measurements. This is analyzed in chapter 8. Figure 7-14 shows the spurious band of the filter. At the spurious band other wave modes are exited which are seen as increased ripple at the spurious band.

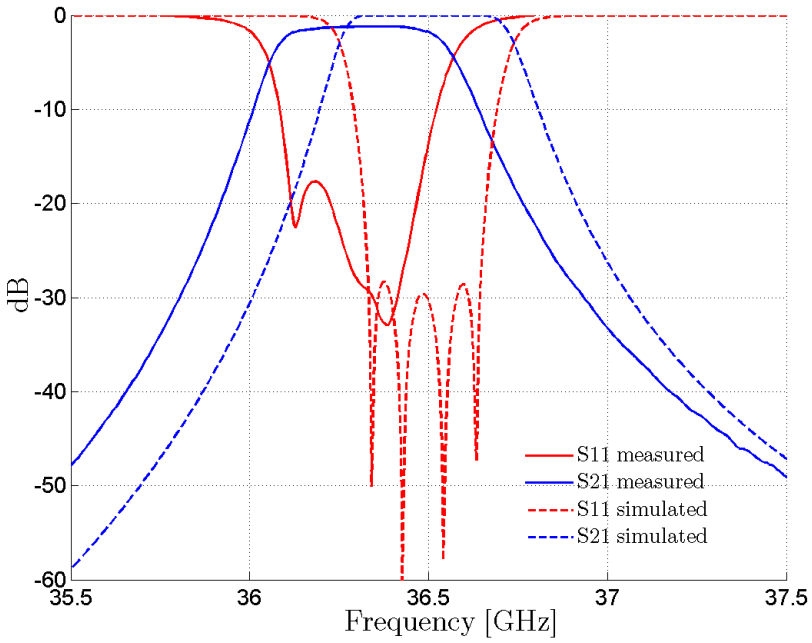

Figure 7-13 Simulated and measured results of WR28 4th order E-plane metal insert filter.

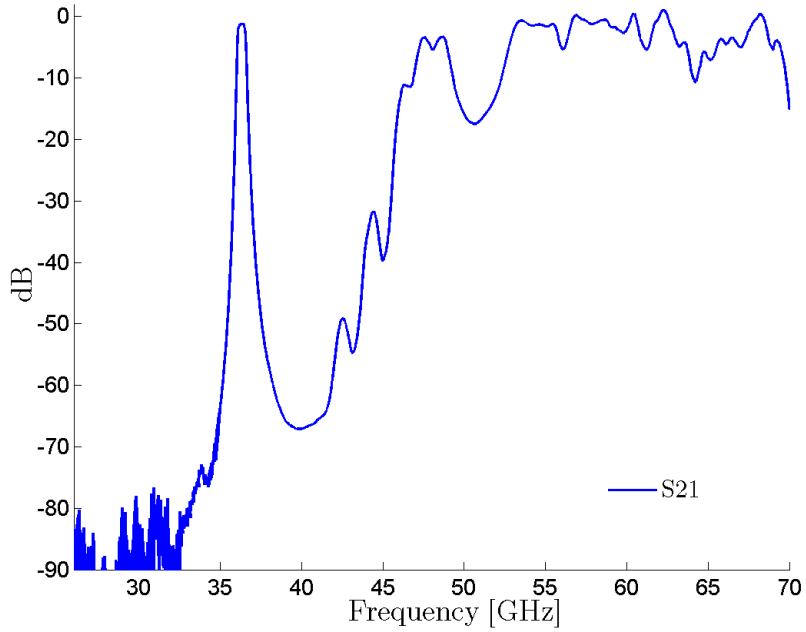

Figure 7-14 The measured wideband response of the WR28 4th order E-plane metal insert filter.

The mechanical realization of the filter is shown in Figure 7-15. A split block technique is used. The blocks are yellow chromated aluminium and metal insert brass sheet is gold plated.

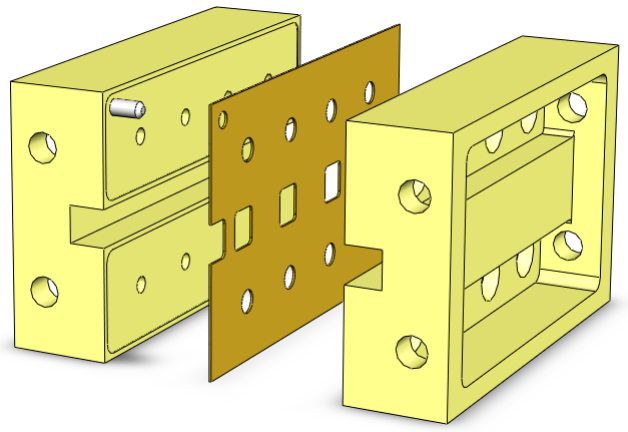

Figure 7-15 Mechanical model of the WR28 metal insert filter. A split block technique with yellow chromated aluminium is used. The brass sheet in the middle is gold plated.

7.3.2 H-plane filter

The presented theory assumes negligible iris thickness. Increasing iris thickness moves the pass-band to higher frequencies and decreases the bandwidth. This is compensated by calculating with initial values that lead to lower center frequency and wider bandwidth. This adjustment also includes the rounding of irises which results from manufacturing process. Rounding shifts the pass band about $1GHz$ to higher frequencies when $0{,}5mm$ radius is used.

Table 24 Low pass filter prototype element values for 5th order Tchebyscheff with 0,01dB ripple.

Tchebyscheff low pass values:						
g0	g1	g2	g3	g4	g5	g6
1	0,7563	1,3049	1,5773	1,3049	0,7563	1

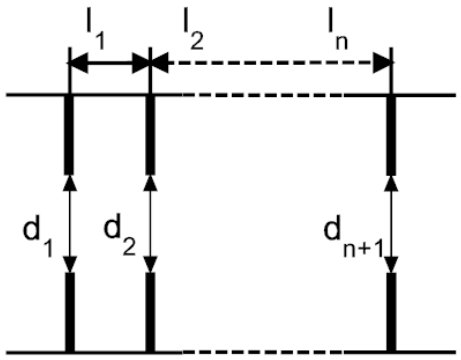

Figure 7-16 Geometry of iris filter with N+1 irises with order N.

The electrical length between the cavities is given in [33]

$$\theta_j = \pi - \frac{1}{2}\left(\tan^{-1}\left[\frac{2X_{j-1,j}}{Z_0}\right] + \tan^{-1}\left[\frac{2X_{j,j+1}}{Z_0}\right]\right) \qquad (7\text{-}39)$$

For large bandwidths $d << a$, and l is approximately half the guide wavelength. The first spurious band is near the frequency where $\theta_j \approx 2\pi\, rad$. Because of the dispersion in the waveguide this occurs roughly at one and half times f_c [34]. This can be problematic with large bandwidth filters where spurious band comes close to the upper cut-off frequency of the pass band. The iris window width is given in [35]

$$\frac{X_{j,j+1}}{Z_0} = \frac{a}{\lambda_{g0}} \cot^2\left(\frac{\pi d_{j.j+1}}{2a}\right)\left[1 + \left(\frac{1}{2}\sqrt{2 - \left(\frac{a}{\lambda_{g0}}\right)^2 - \frac{3}{4}}\right)\sin^2\left(\frac{\pi d_{j,j+1}}{2a}\right)\right] \quad (7\text{-}40)$$

Equation is solved numerically. After calculations the filter is optimized with uWizard and finally checked with HFSS. The calculated and optimized results are presented in Table 25.

Table 25 Calculated and optimized values of the W-band iris filter. Primed values mark the initial values and non-primed the optimized values. Iris thickness is 0,26mm.

Calculated and optimized iris window and resonator lengths [mm]						
k	1	2	3	4	5	6
l'_j	1,832	2,081	2,125	2,081	1,832	-
$d'_{j,j+1}$	1,423	0,924	0,781	0,781	0,924	1,423
lj	1,783	2,030	2,062	2,030	1,783	-
$d_{j,j+1}$	1,393	0,936	0,838	0,838	0,936	1,393

Figure 7-17 shows the simulation results from uWizard of the filter with measured results. The measured insertion loss at maximum point is $1{,}9dB$ and the $3dB$ points are found at $87{,}4GHz$ and $91GHz$. Filter has asymmetrical response. The return loss at the lower part of the pass-band is poor, which leads to increased insertion loss. The center frequency accurately follows the simulated response. The filter has equivalent noise bandwidth of $3{,}73GHz$. Figure 7-18 shows the wideband simulation of the iris filter. We can see the spurious band around $140GHz$. Simulation only models TE10 mode. The power spectral density at diode detector needs to be analyzed to see if there is a significant power at the spurious band which could affect the radiometer measurements. This is analyzed in chapter 8. The mechanical model of the filter is shown in Figure 7-19.

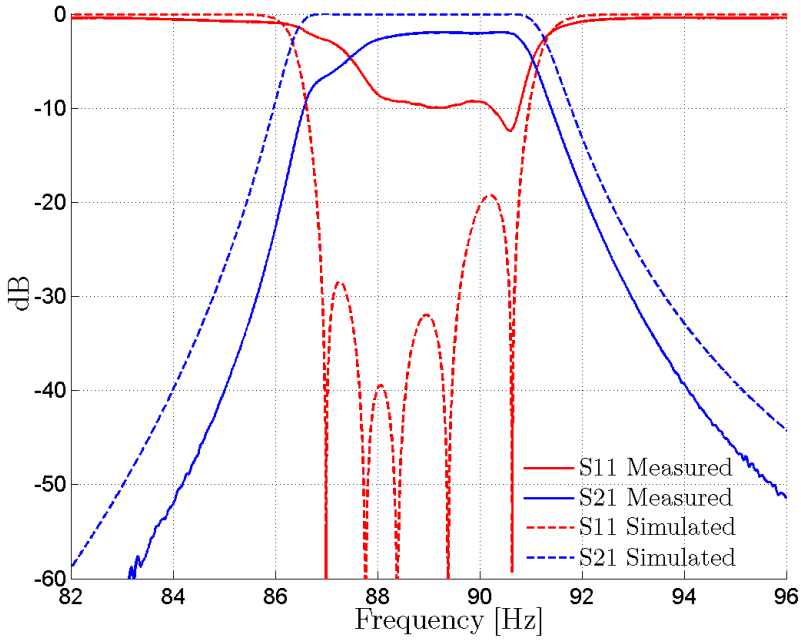

Figure 7-17 Simulated and measured results of WR10 5th order H-plane iris filter.

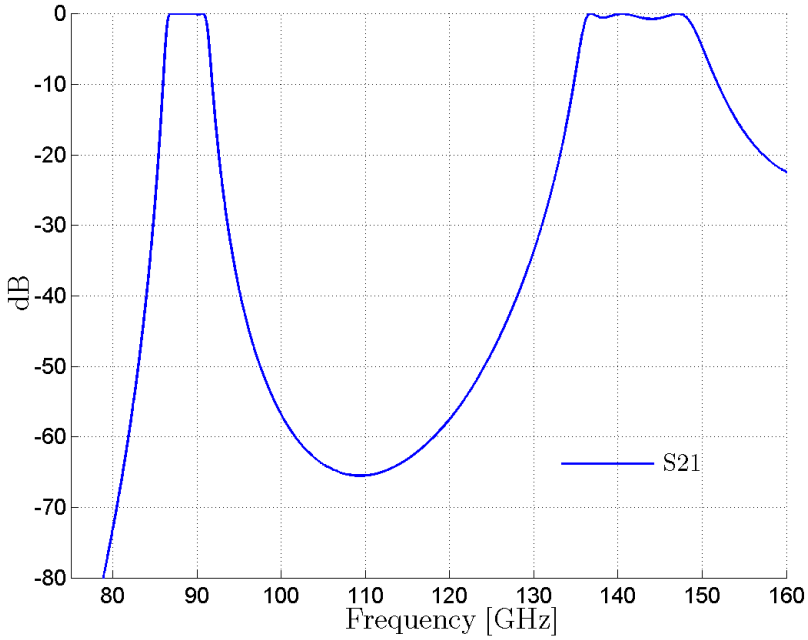

Figure 7-18 Simulated wideband response of the WR10 5th order H-plane iris filter.

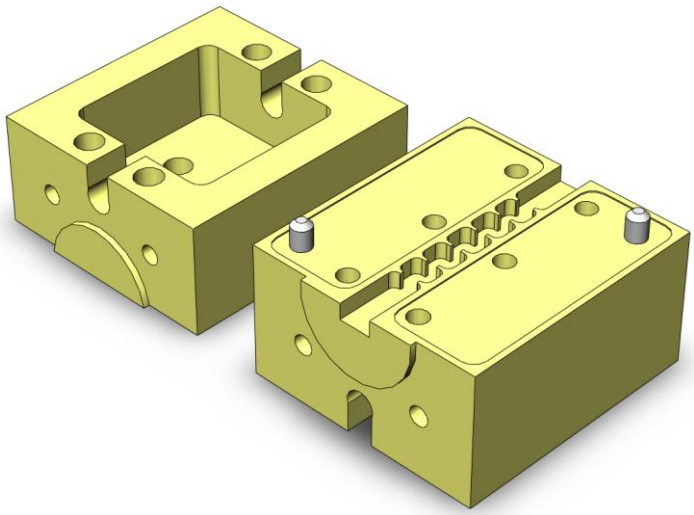

Figure 7-19 Mechanical model of the WR10 iris filter. A split block technique with yellow chromated aluminium is used.

8 VERIFICATION

The system calculations shown in Table 3 and Table 4 were updated with measured values. The results are shown in Figure 8-1 and Figure 8-2. For the Ka-band radiometer all estimations fit closely with the measured values. The noise figure is about 0,2dB higher and the gain is $1{,}2dB$ higher than expected. This is, however achieved with somewhat higher bias currents than the nominal ones used in the previous system calculations. The equivalent noise bandwidth of the BPF is $500MHz$ which increases the output power. The output power is about $1{,}9dB$ higher than estimated. This can be easily adjusted with the LNA bias conditions if required. The wideband gain bandwidth is normalized to measured gain at $36{,}5GHz$ and is $13{,}7GHz$. Ka-band radiometer has an extra isolator between the BPF and the third LNA. Another option if some decoupling is needed for LNA stability is to integrate small microstrip attenuator inside the 1xLNA+Detector block.

Due to some stability issues W-band radiometer was modified. The LNAs are no longer in the same mechanical block but were separated to individual blocks and the microstrip attenuators were changed to waveguide isolators. This leads to significantly larger mechanical size. Some level of integration is required to achieve more compact overall size. This is to be decided after preliminary system verification. The W-band radiometer has more gain than expected. The LNA gains estimates used in system calculations in chapter 5.3 were conservative. These modifications and higher LNA gain led to overall gain increase. The output power is estimated to be $-28{,}2dBm$. The power level can be further be adjusted with LNA bias currents to get either more or less power. The noise figure is about $0{,}6dB$ lower than expected. The given LNA noise figure is, however, only an estimate which is based on previous measurements made in DA-Design Ltd to similar LNA blocks. Most of the improvement arises from the designed and manufactured waveguide switch that has significantly smaller insertion loss than expected. The equivalent noise bandwidth of the filter is $3700MHz$ which was less than the specified bandwidth of $4000MHz$. This was due to the insertion loss at the lower end of the passband. This is due to manufacturing tolerances that changed the filter performance. The equivalent bandwidth is normalized with the maximum value of the response which reduces the noise bandwidth.

These configurations are used in the preliminary verification phase and the actual requirement for the presented changes is to be evaluated.

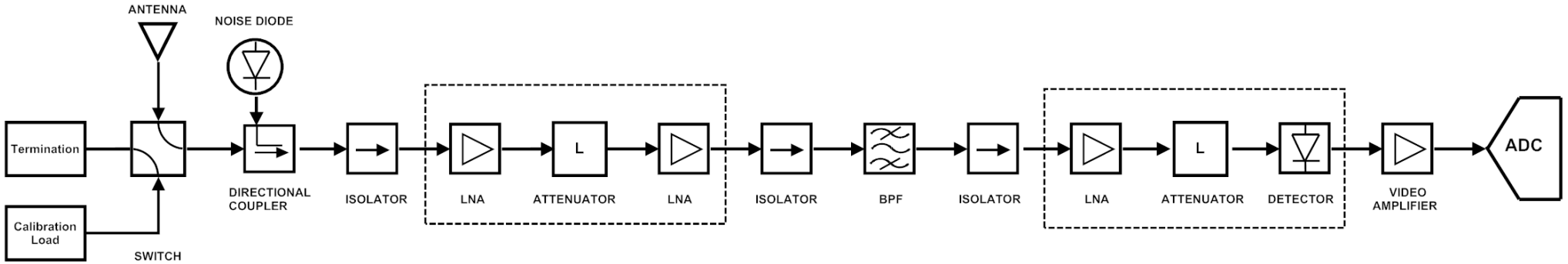

Radiometer Ka-band											
[dB]	Switch	Coupler	Isolator	LNA1	ATT	LNA2	Isolator	BPF	Isolator	LNA3	ATT
NF	0,1	0,5	0,2	3,4	3,0	3,4	0,2	1,2	0,2	3,9	3,0
Gain	-0,1	-0,5	-0,2	21,0	-3,0	21,0	-0,2	-1,2	-0,2	21,0	-3,0
NF Cascade	0,1	0,6	0,8	4,2	4,2	4,3	4,3	4,3	4,3	4,3	**4,3**
Gain Cascade	-0,1	-0,6	-0,8	20,2	17,2	38,2	38,0	36,8	36,6	57,6	**54,6**
[dBm]											
Output Power	-72,6	-72,6	-72,6	-48,2	-51,2	-30,2	-30,4	-45,9	-46,1	-25,1	**-28,1**

Figure 8-1 Updated Ka-band radiometer block diagram and system calculations. Calculations are based on individual block measurements. Dashed lines in the block diagram indicate mechanical integration. One isolator is added between BPF and third LNA. This is the configuration used in system verification phase. Calibration plane is referred to the directional coupler input.

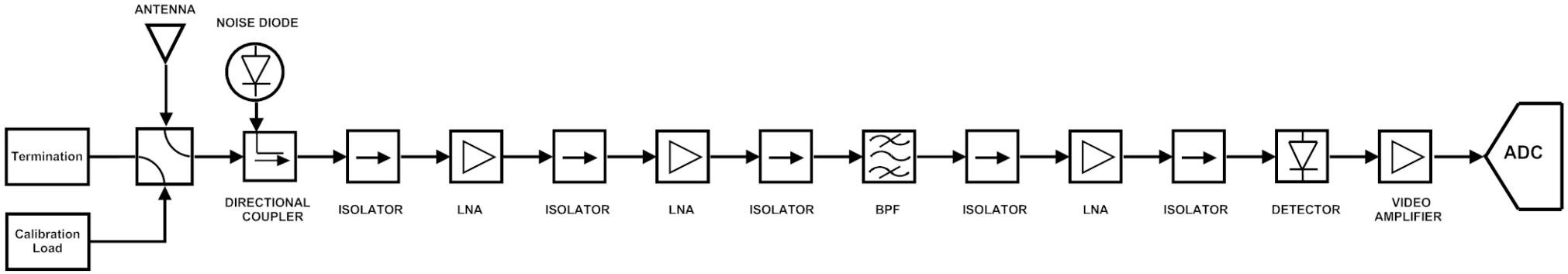

Radiometer W-band											
[dB]	Switch	Coupler	Isolator	LNA1	Isolator	LNA2	Isolator	BPF	Isolator	LNA3	Isolator
NF	0,2	0,7	0,5	4,5	0,5	4,5	0,5	2,0	0,5	4,0	0,5
Gain	-0,2	-0,7	-0,5	16,5	-0,5	16,5	-0,5	-2,0	-0,5	16,5	-0,5
NF Cascade	0,2	0,9	1,4	5,9	5,9	6,0	6,0	6,0	6,0	6,0	**6,0**
Gain Cascade	-0,2	-0,9	-1,4	15,1	14,6	31,1	30,6	28,6	28,1	44,6	**44,1**
[dBm]											
Output Power	-71,0	-71,0	-71,0	-50,0	-50,5	-33,9	-34,4	-43,7	-44,2	-27,7	**-28,2**

Figure 8-2 Updated W-band radiometer block diagram and system calculations. Calculations are based on individual block measurements. Mechanical construction of this configuration is significantly different from the original design. This is the configuration to be used in system verification phase after which the level of integration is determined. Calibration plane is referred to the directional coupler input.

8.1 Ka-band radiometer

This section shows the measurement results for the Ka-band radiometer components. From the individual component measurements the total radiometer response is calculated as well as the power spectral density at the diode detector. Measured results are compared with the nominal design values with a discussion on the optimal LNA bias conditions.

8.1.1 Low noise preamplifier

The low noise amplifier block with two LNA chips and a 3dB microstrip attenuator in between was measured with Anritsu VectorStar – Vector Network Analyzer (VNA). Both LNAs both have nominal gain of $21dB$ leading to a nominal $39dB$ gain of the LNA block (including the attenuator). The mean gain at the LNA gain bandwidth is $36{,}8dB$. If we also account for the measured losses at the transitions the gain is within $1dB$ from what was expected. For stabilizing purposes a magnetically loaded absorber was glued inside the housing on top of the LNA, which is a common way to suppress cavity resonances.[21].

The used bias circuitry to drive the LNAs is a constant voltage type where precision voltage reference is used. The effect of drain current on gain was investigated and the result is shown in the left hand side of Figure 8-3. The drain voltage is kept constant and with different gate voltages the corresponding gains and drain currents are recorded. The gain vs drain voltage was measured by keeping the gate voltage constant and changing the drain voltage. It is clear that gate voltage fluctuations have prominent effect on gain which was not observed with drain voltage. Gain sensitivity is defined as the slope between gain and drain current and has units $[dB/mA]$. For higher drain currents the gain sensitivity is smaller. This indicates that the fluctuations of the bias circuitry cause smaller gain fluctuations, if the LNAs are biased with higher drain currents. Gain sensitivity to current fluctuations at $36{,}5GHz$ point frequency is shown in the right hand side of Figure 8-3.

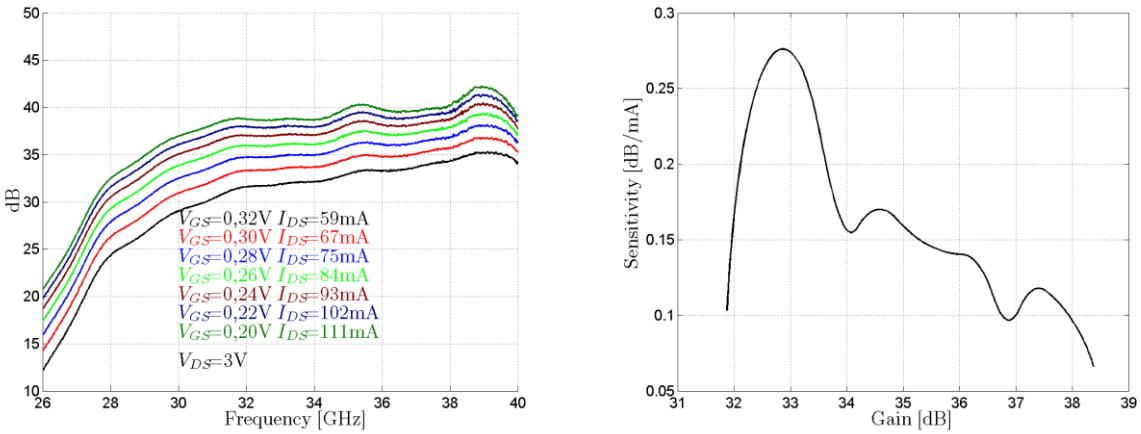

Figure 8-3 Left: The effect of drain current to gain in 2XLNA block with the expected gain around 38dB. Note that the absolute value of the gate voltages are shown. All gate voltages are negative respective to ground. Right: Measured gain sensitivity at 36,5GHz by changing gate voltage and recording bias current and gain. Sensitivity is the slope between gain and bias current [dB/mA].

LNA gain fluctuations are believed to arise from multiple sources e.g. inherent amplifier gain fluctuations, bias circuitry fluctuations and fluctuations generated by ambient noise coupled through radiometer box. In addition these fluctuations are affected by temperature fluctuations. It was also found, as discussed, previously that drain current and gain fluctuations correlate and the low frequency fluctuations can be reduced from the measurements by computing. With this assumption the sensitivity of measuring the fluctuations from drain currents is maximized with high current conditions. Another finding was that the radiometer resolution is limited by the $1/f$ noise of the amplifiers. The LNA $1/f$ noise is reduced with low drain voltage. This was discussed in chapter 4.2. Therefore the final LNA bias condition that optimizes the radiometer resolution is obtained with low V_{DS} but high I_{DS}.

Noise figure is measured with Rohde&Schwarz ZVA40. It has the ability to directly measure the noise figure without external power sources and is described in [36]. Figure 8-4 shows the noise figure over the waveguide band. It can be seen that noise performance deteriorates rapidly below $32GHz$. This can also be seen from the gain measurement where gain starts to drop below $32GHz$ due to LNA chip performance. Whether or not the noise performance of the block deteriorates so rapidly is unclear. The used noise figure measurement introduces error when sufficient gain is not available and full confidence of the noise figure below $32GHz$ is not achieved. The nominal noise figure

for one LNA chip is $2{,}8dB$. If the whole block is considered including the losses from the transitions, the measured value is in close agreement with the expected value.

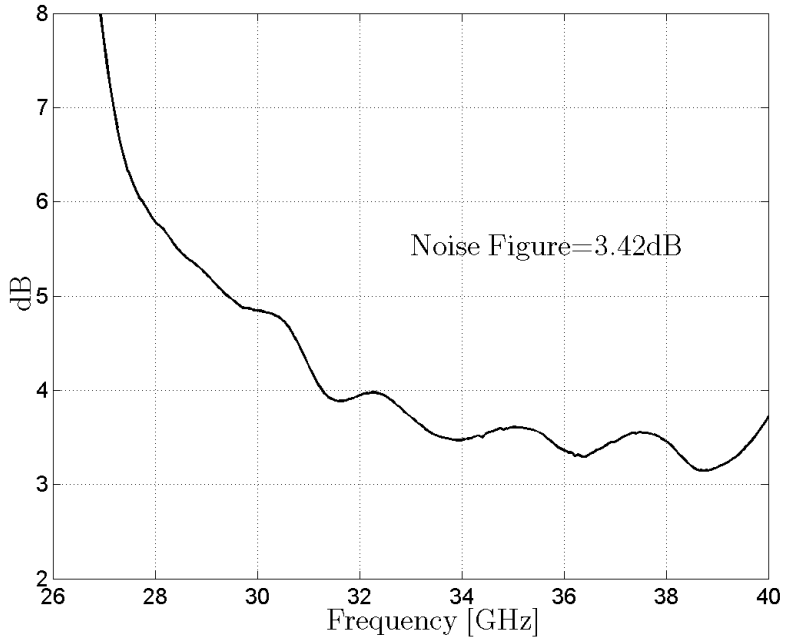

Figure 8-4 Noise figure of the 2xLNA block. Noise figure is averaged between 35,5GHz…37,5GHz and is 3,42dB.

8.1.2 Noise diode

The excess noise ratio (ENR) of the noise diode is measured with R&S ZVA40, which can be used as a power meter. Although receiver power calibration could not be done, the diode ENR can be measured by placing the noise diode block to the input of the radiometer and switching it on and off with bias current. If enough amplification is provided the noise contribution of the receiver can be neglected and the ENR can be calculated from the measured difference. The measured power for both cases is $k(T_{ON/OFF} + T_{REC})BG = P_{ON/OFF}$. Assuming $T_{OFF} = 290K$ and knowing the noise figure by measurement T_{ON} can be calculated by taking the ratio of these measurements. Calculated T_{ON} is plugged into eq.(5-1). Amplification unit is the actual radiometer with one extra LNA to provide sufficient gain. Since the BPF is used in the amplification unit to prevent LNA saturation the ENR calculation is only valid where the amplified noise power is well above the power meter noise floor. The average ENR between $36{,}1 \ldots 36{,}5GHz$ is $9{,}8dB$ with $20mA$ bias current. This is lower than was expected from the manufacturer data. The designed cross coupler has measured coupling

of $16{,}8dB$. This leads to $64K$ as the injected noise temperature to the radiometer channel. The simulated value for good calibration performance was found to be $200K \ldots 400K$. It was, however, found that the noise diode has $15 \ldots 20dB$ ENR at lower frequencies of the waveguide band. This implies that tuning the noise diode to higher frequencies would provide sufficient ENR. With the given ENR the radiometer can be calibrated, but the radiometer resolution is increased compared to higher noise diode ENR.

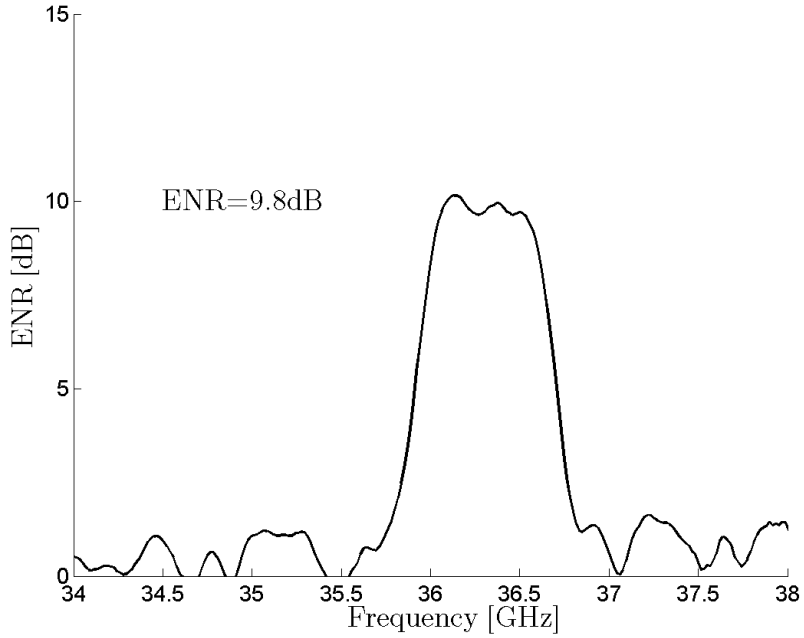

Figure 8-5 The calculated ENR from the spectral density difference. The average is taken from 36,1…36,5GHz.

8.1.3 Diode detector

Left hand side of Figure 8-6 shows the measured response of the detector. The detector input power is an estimate since the mechanical block also includes an attenuator and an LNA. Nominal gain and attenuation are used when the detector input power is calculated. A directional coupler is used in the measurement and the input power of the 1xLNA + Detector block in monitored with calibrated power meter. It can be seen that higher load resistance yields higher output voltage as expected. This also limits the dynamic range compared to the lower resistance value. In the middle of the figure the sensitivity of the detector calculated from the measurement results is shown. The sensitivity is in-

line with the data of the diode manufacturer. $10k\Omega$ was chosen for the output resistance of the diode detector. The frequency response of the detector block is shown on the right of the Figure 8-6. The detector is most sensitive around the designed frequency implying good matching between the components inside the detector block.

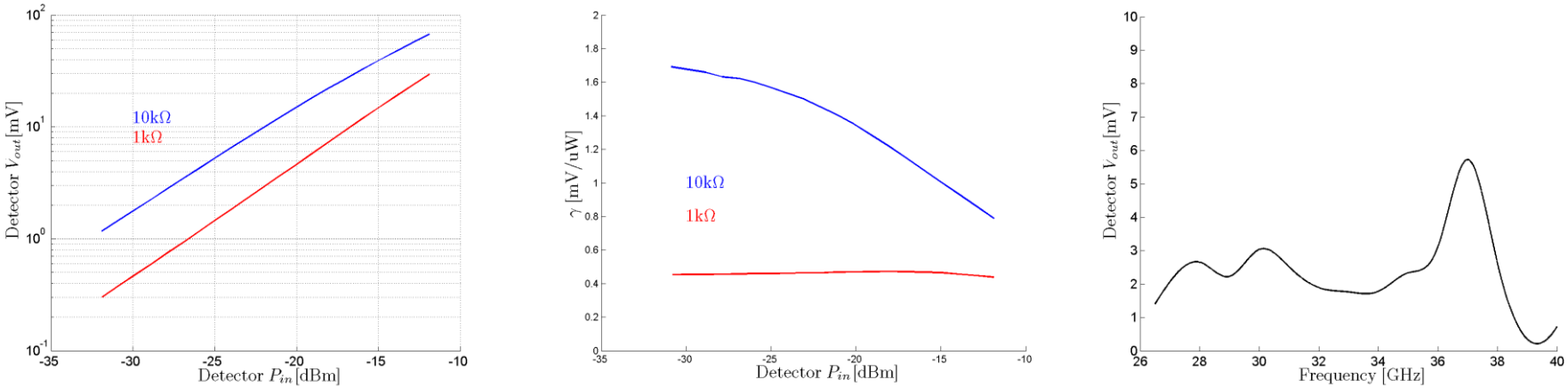

Figure 8-6 Left: Response of the Ka-band radiometer detector with 1kΩ and 10kΩ load resistances at 36,5GHz. Middle: Detector sensitivity with 1kΩ and 10kΩ load resistances at 36,5GHz. Sensitivity is defined as the slope between input power and output voltage. Right: Detector frequency response with 10kΩ load resistance.

8.1.4 Spectral density

The receiver S-parameters were calculated from individual S-parameter measurements of the radiometer blocks. This enabled the possibility to investigate different cascade configurations. S-parameter matrices of the components cannot be directly cascaded. They can be transformed to T-parameters (Transfer scattering parameters) which allows direct matrix multiplication to cascade components. The cascaded T-parameter matrix can then be transformed back to S-parameter matrix. Conversion equations are given in [37] and they are reproduced below. The S/T-parameter data used in calculations must be in complex value.

$$T11 = \frac{1}{S21} \tag{8-1}$$

$$T12 = -\frac{S22}{S21} \tag{8-2}$$

$$T21 = \frac{S11}{S21} \tag{8-3}$$

$$T22 = \frac{-\det(\boldsymbol{S})}{S21} \tag{8-4}$$

Cascading of T-parameters is done by multiplication of individual T-matrices.

$$\boldsymbol{T^T = T^1 T^2 \ldots T^n} \tag{8-5}$$

From the combined T-matrix the resulting S-parameters are obtained by

$$S11 = \frac{T21}{T11} \tag{8-6}$$

$$S12 = \frac{\det(\boldsymbol{T})}{T11} \tag{8-7}$$

$$S21 = \frac{1}{T11} \tag{8-8}$$

$$S22 = -\frac{T12}{T11} \tag{8-9}$$

From the individual block measurements the resulting receiver S-parameters are calculated. The third LNA that cannot be directly measured and it is assumed to have the same spectral shape as the 2xLNA block with gain adjusted accordingly. The maximum gain of the radiometer was around $56dB$ which can be further adjusted with LNA bias. The equivalent noise bandwidth of the radiometer is roughly $490MHz$ and the center frequency is within $0{,}33\%$ from the nominal frequency. The return loss at the input is better than $23dB$ inband. This is mainly determined by the first isolator.

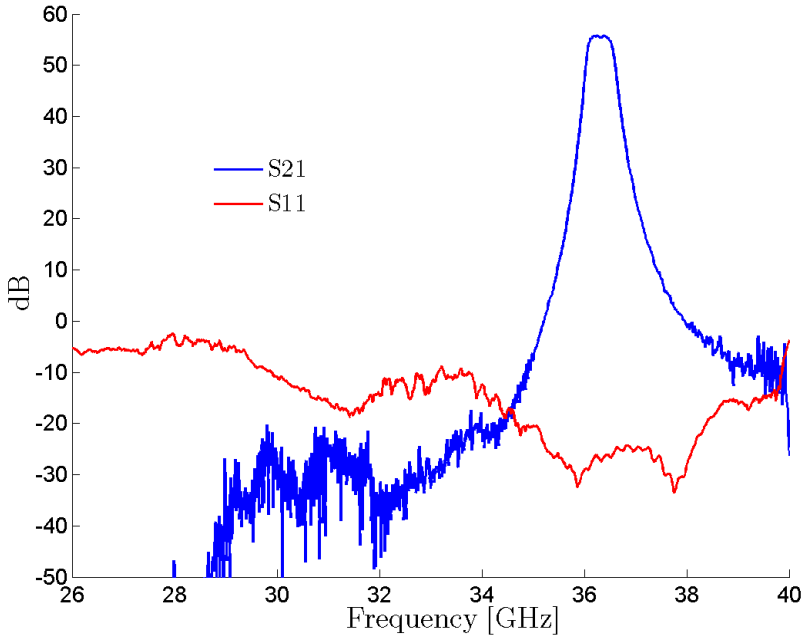

Figure 8-7 Ka-band radiometer gain and reflection of the radiometer. Each block in the radiometer is measured individually and cascaded with the help of T-parameters.

To determine the power spectral density at the input of the diode detector wideband simulations were made to determine that it is the designed frequency band that determines the output voltage of the diode. A particular concern was the spurious band of Ka-band BPF. Measured filter spurious band is shown in Figure 7-14. In this simulation reflections were omitted and only the insertion gain was used from each individual block measurement. These measurements were combined to obtain the wideband re-

ceiver response from which the output power spectral density is plotted at various receiver stages shown in Figure 8-8. The effect of the third (last) LNA is seen at the detector input. The choice was made that the BPF filter would be located before it. The noise floor at diode is raised above the thermal noise floor due to wideband gain of the last LNA. It is also evident that extra filtering before the third LNA would not help since after the BPF the power spectrum is at the noise floor excluding the insignificant extra power between $45GHz \dots 50GHz$ arising from the BPF spurious band. The waveguide to microstrip transitions act as low pass filter at frequencies somewhat above $40GHz$ where other modes in the waveguide are exited. The energy is converted from the fundamental mode to other modes. These other modes are greatly attenuated in the transition. The gain of the LNAs is decreased above frequencies of $40GHz$. These effects combined result to insignificant power at BPF spurious band. The given model uses measurement results so it can be concluded that all the power whether or not it is in the fundamental mode, is included. The inband power is defined as $-10dB$ bandwidth from the maximum value and $P_{INBAND} = -28{,}23dBm$. The total power at $26GHz \dots 70GHz$ frequency range $P_{TOTAL} = -28{,}12dBm$. The power restricted by the BPF clearly dominates the measurement.

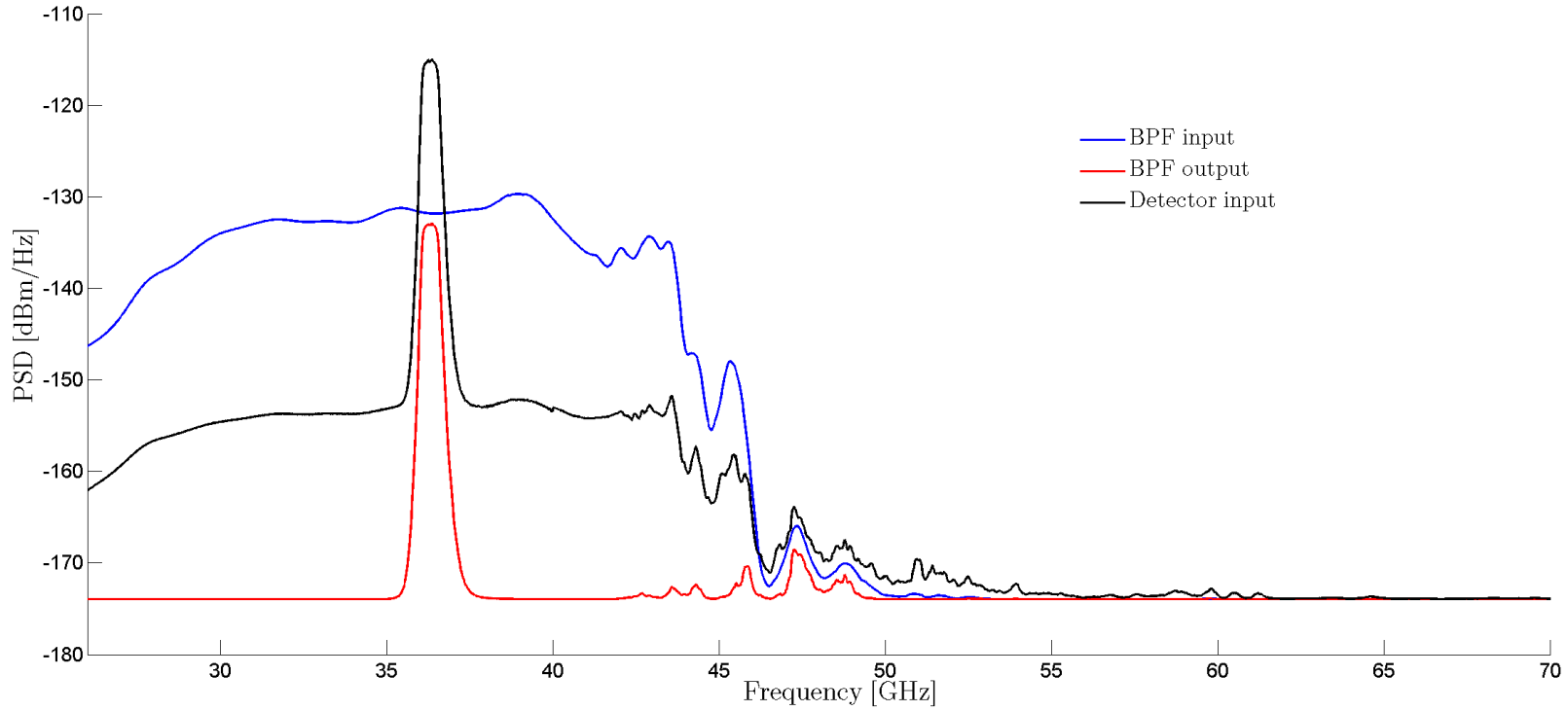

Figure 8-8 Power spectral densities at various stages of the Ka-band radiometer. Calculations are made from S-parameter measurements of the radiometer blocks. Two sets of individual component measurements from 26…40GHz and 40…70GHz were combined. 290K load is assumed at the input of the radiometer.

8.2 W-band radiometer

This section shows the measurement results for the W-band radiometer components. From the individual component measurements the total radiometer response is calculated as well as the power spectral density at the diode detector. Measured results are compared with the nominal design values.

8.2.1 Low noise preamplifier

The W-band radiometer has three individual LNA blocks due to design modification discussed earlier. These were measured with R&S ZVA110E and the gain is shown in Figure 8-9. The gain in the nominal band is roughly $16 \ldots 18dB$ depending on the LNA. With proper bias conditions this can be increased some decibels. Discussion concerning low frequency fluctuations addressed in Ka-band measurements applies here also. These amplifiers, however, exhibit stronger dependency on V_{DS} than was observed for the Ka-band amplifiers. It was also observed that after some point, increasing V_{GS} will reduce the gain while I_{DS} is still increasing. This means that the LNA bias that optimizes the resolution might not be obtained with low V_{DS} and high I_{DS} conditions which was the case for Ka-band LNAs. Measurements with different bias conditions and resulting power spectral densities needs to be measured and compared to obtain full knowledge of the $1/f$ noise behavior of the amplifiers. Noise figure of these amplifiers were not measured. Chips from the same manufacturing path in similar mechanical construction showed that these blocks exhibit LNA noise figure $4..5dB$ with little variation.

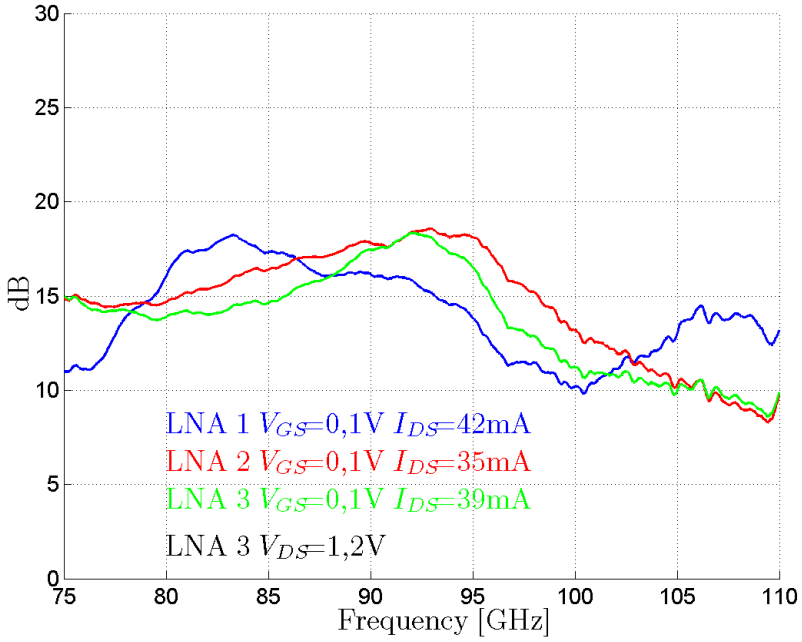

Figure 8-9 W-band LNA gains with nominal bias conditions.

8.2.2 Noise diode

The excess noise ratio (ENR) of the noise diode is measured with R&S ZVA110E. It has the possibility to be used as a power meter. Although receiver power calibration could not be done the diode ENR can be measured by placing the noise diode to the input of the radiometer and switching it on and off in the same manner as was done for the Ka-band noise diode. Noise figure of the amplification unit is $5dB$. Amplification unit is the actual radiometer with one extra LNA to provide sufficient gain. Noise figure is based on previous measurements made in DA-Design Ltd. with chips from the same manufacturing patch. Since the BPF is used in the amplification unit to prevent LNA saturation the ENR calculation is only valid where the amplified noise is well above power meter noise floor. The average ENR in the nominal band is $17{,}4dB$ which is well suited to be used in the radiometer with the designed coupler with $17{,}2dB$ coupling. This leads to 310K of injected noise to the radiometer channel which matches well with the designed value of 200K…400K.

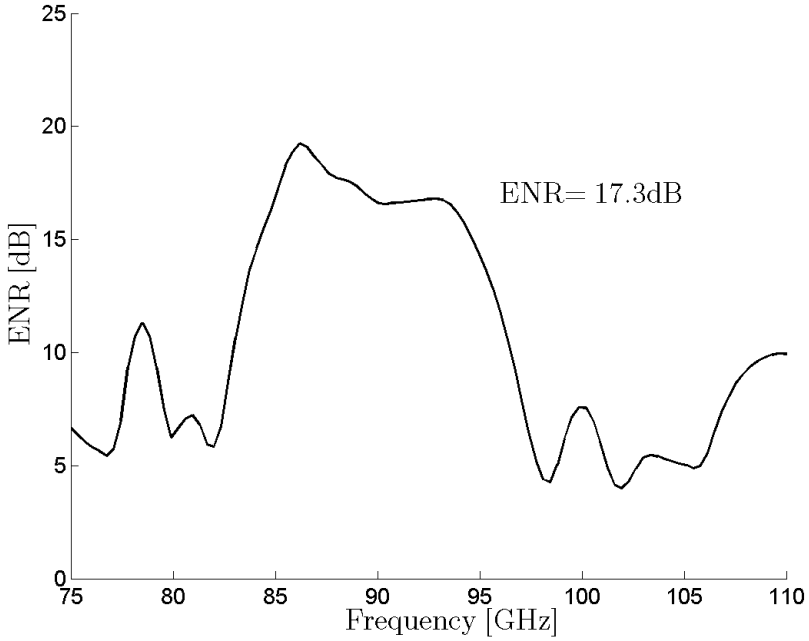

Figure 8-10 The calculated ENR from the spectral density difference. The average is taken from the nominal bandwidth.

8.2.3 Diode detector

Left hand side of the Figure 8-11 shows the measured response of the detector. The detector input power is an estimate since the used input power source was not calibrated. It can be seen that higher load resistance yields higher output voltage as expected. The sensitivity of the detector calculated from the measurement results is shown in the middle of the figure. The sensitivity is lower than what was expected from the diode manufacturer data. The frequency response of the detector was checked. $10k\Omega$ was chosen to be the output resistance of the detector block as was chosen for the Ka-band detector. Right hand side of figure shows the detector frequency response. The output voltage is strongest at the lower end of the waveguide band. This implies poor return loss at the detector. This can be improved by tuning the physical placement of the detector chip or with tuning circuits. This is however not required since the output voltage at the detector can be increased simply by adjusting LNA gain and a good return loss is ensured by using isolator in front of the detector.

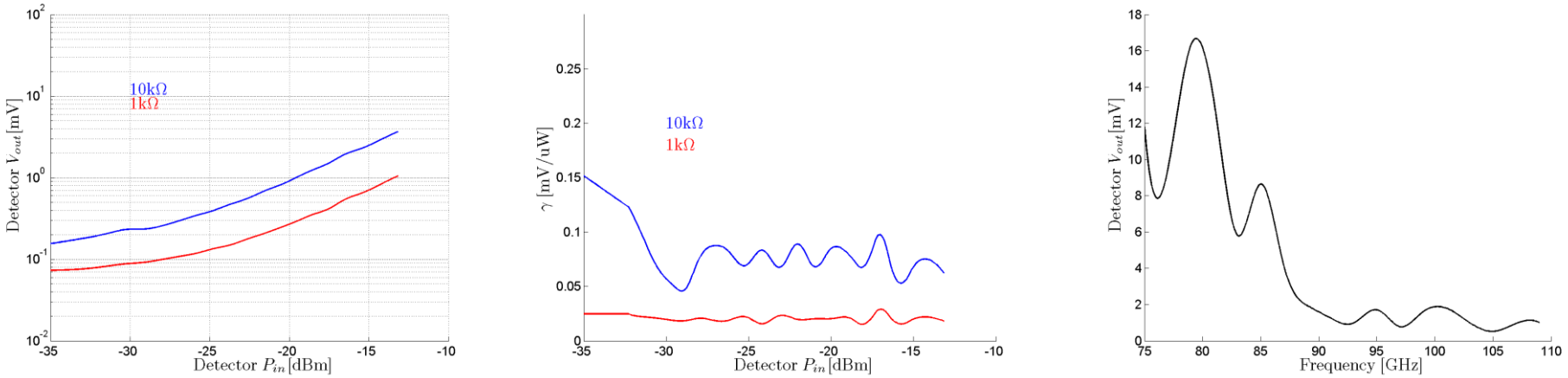

Figure 8-11 Left: Response of the W-band radiometer detector with 1kΩ and 10kΩ load resistances at 89GHz. Middle: Detector sensitivity with 1kΩ and 10kΩ load resistances at 89GHz. Sensitivity is defined as the slope between input power and output voltage. Right: Detector frequency response with 10kΩ load resistance.

8.2.4 Spectral density

The receiver S-parameters were calculated from individual S-parameter measurements of the radiometer blocks in a similar manner as was done for the Ka-band radiometer. This is shown in Figure 8-12. The W-band radiometer gain is $42{,}8dB$ when averaged over the nominal bandwidth. The equivalent noise bandwidth with the average gain is $4{,}4GHz$. From the average gain the $3dB$ bandwidth is $87{,}7 \ldots 91{,}2GHz$. The return loss averaged over the nominal band is $-22{,}5dB$. The isolators around the BPF have deteriorated return loss and isolation at the filter roll-off. This is seen as small bumps in the roll-off and the roll-off is not as steep when the filter is measured with well matched loads. This has negligible effect on the equivalent noise bandwidth and to the total power at the diode.

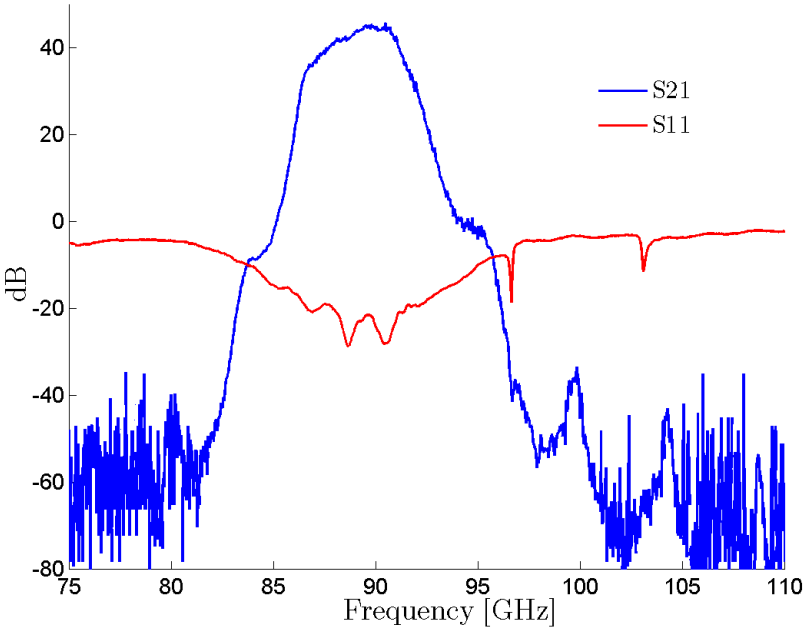

Figure 8-12 W-band radiometer gain and reflection from the radiometer input to detector input. S-parameters of the radiometer blocks were measured individually and then cascaded with the help of T-parameters.

The power spectral density was calculated in a similar manner as was done for the Ka-band radiometer shown in Figure 8-13. However, it was not possible to measure the frequency response up to the spurious band of the filter and thus the noise contribution at these frequencies remained unexamined. From the plotted spectral density and from the LNA measurements it is evident that no gain is present at 140GHz where the simulated BPF spurious band is located. The in-band power is defined as $-10db$ points from the mean gain in the nominal bandwidth and $P_{INBAND} = -28{,}12dBm$. Total power at $75 \dots 110GHz$ frequency range $P_{TOTAL} = -28{,}04dBm$. The power restricted by the BPF clearly dominates the measurement.

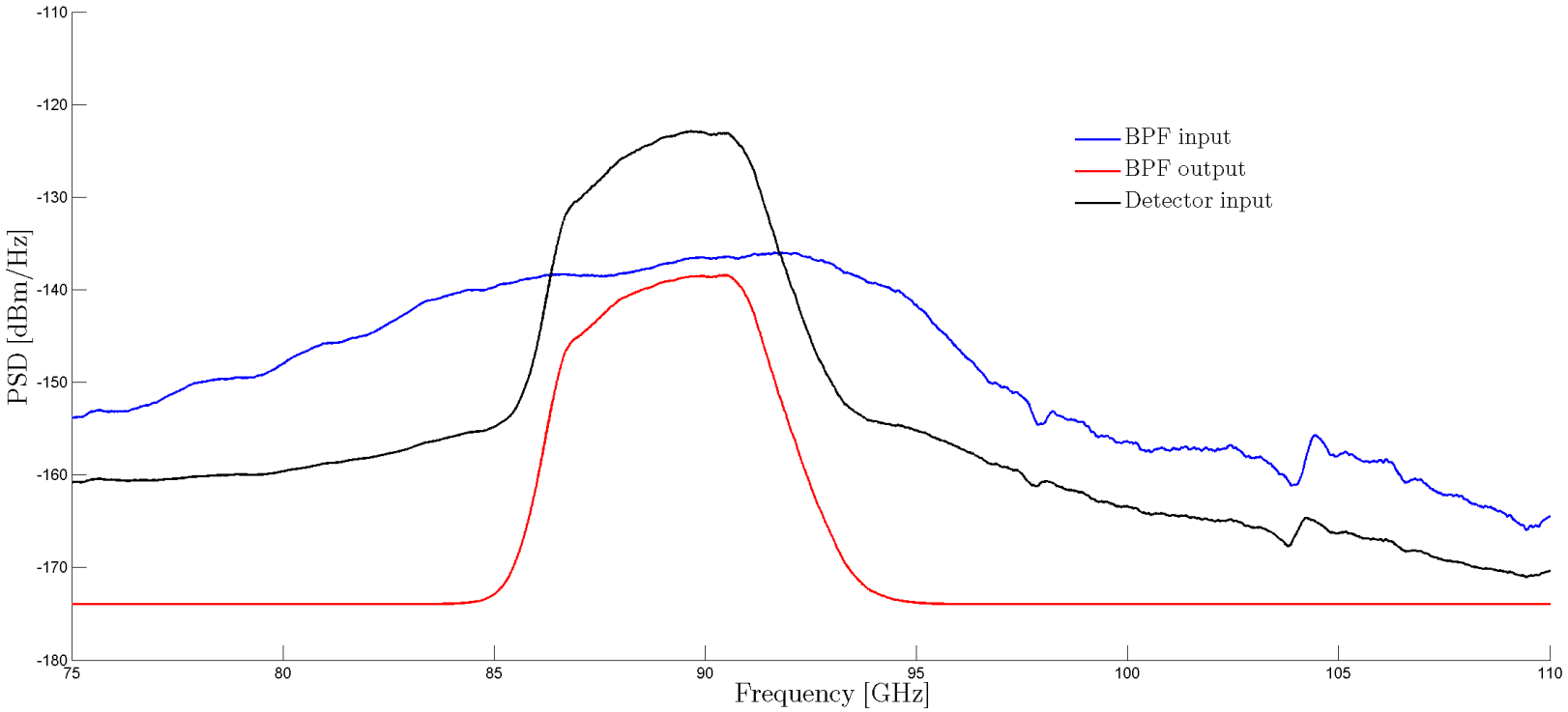

Figure 8-13 Power spectral densities at various stages of the W-band radiometer. Calculations are made from S-parameter measurements of the radiometer blocks. 290K load is assumed at the input of the radiometer.

9 CONCLUSIONS

Design of two radiometer at $36{,}5GHz$ and $89GHz$ were presented. Both radiometers are total power radiometers. The overall system description was presented. System design including noise temperature, gain, linearity and wideband noise was analyzed for both radiometers. Two radiometer calibration procedures were discussed with system simulations describing the errors involved with calibrations. Factory calibration is used to determine the exact noise diode temperature that is used in on-site calibration. In factory calibration two known standards are used: an ambient temperature matched load and a cryogenic load. Cryogenic load is an absorbing material soaked in liquid nitrogen which is viewed by an antenna. Cryogenic load design and brightness temperature analysis was presented. Radiometer box and component mechanics were presented in a general level including a brief discussion about thermal stabilization. Radiometer RF components were designed, measured and discussed. The RF component measurements were combined to analyze spurious band contribution to the output voltage.

Radiometers have been incorporated to the ADC measurement board with active temperature stabilization circuitry. Radiometers are functioning and preliminary results show good agreement with designed values and simulated estimates.

10 REFERENCES

[1] F T Ulaby, R K Moore, and A K Fung, *Microwave Remote Sensing Volume 1.*: Artech House, Inc, 1981.

[2] F T Ulaby, R K Moore, and A K Fung, *Microwave Remote Sensing Volume 3.*: Artech House, Inc, 1981.

[3] H-J C Blume, "Variation of the Microwave Brightness Temperature of Sea Surfaces Covered with Mineral and Monomolecular Oil Films," *IEEE Transactions on Geoscience and Remote Sensing*, no. 21-3, 1983.

[4] T Poutanen, Map-Making and Power Spectrum Estimation for Cosmic Microwave Background Temperature Anisotropies, 2005.

[5] W C Daywitt, *Design and Error Analysis for the WR10 Thermal Noise Standard.*: National Bureau of Standards, 1983.

[6] John D Kraus, *Radio Astronomy*, 2nd ed.: Cygnus-Quasar Books, 1986.

[7] D M Pozar, *Microwave Engineering*, 3rd ed.: John Wiley & Sons, Inc, 1989.

[8] R H Dicke, "The Measurement of Thermal Radiation at Microwave Frequencies," *The Review of Scientific Instruments*, vol. 17, no. 7, July 1946.

[9] N Skou and D L Vine, *Microwave Radiometer Systems: design and analysis*, 2nd ed.: Artech House, Inc, 2006.

[10] Aniello Mennella et al., "Offset balancing in pseudo-correlation radiometers for CMB measurements," 2003.

[11] G S Dow et al., "W-band MMIC direct detection receiver for passive imaging system," *Microwave Symposium Digest, IEEE MTT-S International*, 1993.

[12] Qiu Jinghui and Zhang Ruidong, "Design and analysis of 8mm radiometer used for passive millimeter-wave image system," *Imaging Systems and Techniques, IST '09. IEEE International Workshop*, 2009.

[13] N C Jarosik, "Measurements of the Low-Frequency-Gain Fluctuations of a 30-GHz High-Electron-Mobility-Transistor Cryogenic Amplifier," *IEEE Transactions on Microwava Theory ans Techniques*, vol. 44, no. 2, 1996.

[14] S T Brown, S Desai, Lu Wenwen, and A B Tanner, "On the long-term Stability of Microwave Radiometers Using Noise Diodes for Calibration," *Geoscience and Remote Sensing, IEEE Transactions*, no. 45, pp. 1908-1920, 2007.

[15] N Skou, "Measurements on Active Cold Loads for Radiometer Calibration,"

in *Microwave Radiometry and Remote Sensing of the Environment*, 2008.

[16] Edward Racette Paul, "Radiometer Design Analysis Based Upon Measurement Uncertainty," George Washington University, PhD thesis 2005.

[17] M Seiffert et al., "1/f noise and other systematic effects in the Planck-LFI radiometers," *A&A*, 2002.

[18] W J Riley, *Handbook of Frequency Stability Analysis*.: Hamilton Technical Services, 2007.

[19] C Sanabria, Noise of AlGaN/GaN HEMTs and Oscillators, 2006, Disseration.

[20] Application Note 57-2, Noise Figure Measurement Accuracy - The Y- Factor Method , 2010.

[21] P Dixon, *Dampening cavity resonance using absorber material*.: Microwave Technology.

[22] C L Trembath, D F Wait, G F Engen, and W J Foote, "A Low- Temperature Microwave Noise Standard," *Microwave Theory and Techniques, IEEE Transactions*, vol. 16, no. 9, pp. 709-714, 1968.

[23] W N Hardy, "Precision Temperature Reference for Microwave Radiometry," *Microwave Theory and Techniques, IEEE Transactions*, no. 21, pp. 149-150, 1973.

[24] L Ying, G Wei, and Z Zuyin, "Radiation from the cryogenic calibration load for microwave radiometers," *Journal of Electronics (China)*, vol. 15, no. 2, pp. 182-186, 1998.

[25] T Hewison and A McGrath, "Performance Assesment of Liquid Nitrogen Calibration Target supplied by Fred Solheim (Radiometrics) at 89, 157 and 183GHz," 2001.

[26] Anritsu, "Calculating VNA Measurement Accuracy," Application Note.

[27] J A R Ball and T M Sulda, "Crossed Waveguide Directional Couplers for High Power Applications," *Journal of Microwave Power and Electromagnetic Energy*, no. 35-4, pp. 232-241, 2000.

[28] M Kotiranta, A cooled 90 GHz VLBI-receiver front end, 2008, Master's Thesis.

[29] R E Collin, *Field Theory of Guided Waves*, Inc. McGraw-Hill Book Company, Ed., 1960.

[30] A Lehto and A Räisänen, *RF- ja Mikroaaltotekniikka*, 8th ed.: Otatieto, 1994.

[31] Y C Leong and S Weinreb, "Full Band Waveguide to Microstrip Probe Transitions," *IEEE MTT-S Digest*, 1999.

[32] G Matthaei, L Young, and E M T Jones, *Microwave Filters, Impedance Matching Networks and Coupling Structures*.: Artech House, Inc, 1980.

[33] S Bhat and K Koul, *Analysis and design and applications of fin lines*.: Artech House, Inc, 1987.

[34] P A Rizzi, *Microwave Engineering: Passive Circuits*, 1st ed.: Prentice Hall , 1987.

[35] F Sammoura et al., "A micromachined W-band iris filter," in *Digest of Technical Papers of the 13th International Conference on Solid State Sensor, Actuators and Microsystems*, 2005, pp. 1067-1070.

[36] Application Note, Noise Figure Measurement without a Noise Source on a Vector Network Analyzer.

[37] R Mavaddat, *Network Scattering Parameters*, World Scientific Publishing Co Pte Ltd, Ed., 1995.

[38] A Das and S K Das, *Microwave Engineering*.: Tata McGraw Hill Education Private Limited, 2009.

[39] R E Collin, *Foundations for Microwave Engineering*, 2nd ed.: IEEE Press, 2001.

[40] M.H.L Pryce, "Wave guides," *Journal of the Institution of Electrical Engineers - Part IIIA: Journal of the Institution of Radiolocation*, vol. 93, no. 70, pp. 33-39, 1946.

[41] V R Reddy, *13.9 GHZ Radiometer Design*, Defence Technical Information Center, Ed., 1984.

[42] S A Pelyushenko, "Microwave Radiometer System for the Detection of Oil Slicks".

[43] G P Ferrante, F Principato, A Caddemi, N Donato, and G Tuccari, "DC and 1/f noise characterization of cryogenically cooled pseudomorphic HEMT's," in *Proceedings of the 5th Workshop on Low Temperature Electronics*, 2002.

[44] D A Frickey, "Conversions between S,Z,Y,H,ABCD, and T parameters which are valid for complex source and load impedances," *IEEE Transactions on Microwave Theory and Techniques*, vol. 42, no. 2, 1994.

[45] (2012, Jan.) RF Cafe. [Online].

http://www.rfcafe.com/references/electrical/s-h-y-z.htm

[46] A Makdissi, F Vernotte, and E Clercq, "Stability variances: a filter approach," *IEEE Transactions on Ultrasonics, Ferroelectrics and Frequency Control*, vol. 57, no. 5, 2010.